PREDICTIONS VERSUS MEASUREMENTS OF TURBOCHARGER NONLINEAR DYNAMIC RESPONSE

A Thesis

by

JUAN CARLOS RIVADENEIRA

Submitted to the Office of Graduate Studies of
Texas A&M University
in partial fulfillment of the requirements for the degree of

MASTER OF SCIENCE

May 2006

Major Subject: Mechanical Engineering

PREDICTIONS VERSUS MEASUREMENTS OF TURBOCHARGER NONLINEAR DYNAMIC RESPONSE

A Thesis

by

JUAN CARLOS RIVADENEIRA

Submitted to the Office of Graduate Studies of
Texas A&M University
in partial fulfillment of the requirements for the degree of

MASTER OF SCIENCE

Approved by:

Chair of Committee,	Luis San Andrés
Committee Members,	Dara Childs
	Paul Roschke
Head of Department,	Dennis O’Neal

May 2006

Major Subject: Mechanical Engineering

ABSTRACT

Predictions versus Measurements of Turbocharger Nonlinear Dynamic Response.
(May 2006)
Juan Carlos Rivadeneira, B.S., Michigan State University
Chair of Advisory Committee: Dr. Luis San Andrés

The present work advances progress on the validation against measurements of linear and nonlinear rotordynamic models for predicting the dynamic shaft response of automotive turbochargers (TCs) supported on floating ring bearings. Waterfall spectra of measured shaft motions at the compressor and turbine ends of a test TC rotor evidences a complex response, showing synchronous (*1X*) and multiple subsynchronous frequencies along the entire operating speed range (maximum shaft speed ~ 65 krpm). Post-processing of the raw test data by mathematical software allows filtering the synchronous and subsynchronous vibration components for later comparisons to predicted shaft motions. The static performance of the floating ring bearings is analyzed with in-house software (XLSFRBThermal®), which considers thermal expansion of the shaft and bearing components as well as static loading on the bearing due to lubricant feed pressure. In addition, the program calculates rotordynamic force coefficients for the inner and outer films of the floating ring bearing. The turbocharger Finite Element (FE) structural model for the linear and nonlinear analyses includes lumped masses for the compressor and turbine wheels and the thrust collar. The mass imbalance distribution on the TC rotor is estimated from the test data using a procedure derived from the two-plane balancing method with influence coefficients. The linear model yields predictions of rotor synchronous (*1X*) response to imbalance and damped eigenvalues. The analysis evidences that the rotor cylindrical-bending mode is unstable at all shaft speeds while the rotor conical model becomes more unstable as lubricant feed pressure decreases. The predicted synchronous (*1X*) motions agree well with the test data, showing a critical speed at approximately 20 krpm. The linear stability results indicate the existence of three critical speeds occurring at 4, 20 and 50 krpm. The second critical speed corresponds to the rotor cylindrical-bending mode, showing larger amplitudes of motion at the compressor nose than at the turbine end. The third critical speed associated to the rotor first bending modes is well damped. In the nonlinear transient analysis, the nonlinear equations of motion of the system (rotor-FRB) are integrated, and the bearing reaction forces are calculated at each time step in a numerical integration procedure. The model then yields predictions of total motion which is decomposed into synchronous (*1X*) and subsynchronous motions, amplitudes and frequencies. The nonlinear analysis predicts synchronous (*1X*) amplitudes that correlate well with the test data at high shaft speeds (> 30 krpm) but underpredicts the imbalance response at low shaft speeds (<30 krpm). The time transient simulations predict multiple frequency subsynchronous motions for shaft speeds ranging from 10 krpm to 55 krpm, with amplitudes and frequencies that are in good agreement with the measurements. Finally, the shaft motion measurements and predictions demonstrate that the turbocharger dynamic response does not depend greatly on the lubricant feed pressure and inlet temperature for the conditions tested.

DEDICATION

First and foremost I dedicate this work to my wife, Kristin, for her understanding, patience and priceless love. To my family, their love and support have been unconditional throughout my life. I especially thank my brother, Ramiro Rivadeneira, for continuously inspiring me to achieve higher goals in life. To my close friends, Jose Antonio Ruíz, Dario Rubio, Adolfo Delgado and Juan Gabriel Castillo, for your encouragement to complete this work. In particular I thank Dario Rubio and Adolfo Delgado for sharing with me their valuable knowledge and experience. Finally and very importantly, I dedicate this thesis and hard work to my home country, ECUADOR.

ACKNOWLEDGEMENTS

The support of Honeywell Turbo Technologies is gratefully acknowledged, in particular its economical and technical assistance. I acknowledge Dr. Murali Chinta, Dr. Kostandin Gjika, Dr. Chris Groves and Mr. Gerry Larue for their continuous input and support to this research. Special thanks to my advisor, Dr. Luis San Andrés, for granting me the opportunity to perform this research under his guidance and for letting me be part of his team. I sincerely appreciate Dr. Luis San Andrés' willingness to share his knowledge and experience; and in particular for his patience and understanding. Finally, I acknowledge the support and friendship of all the students and staff from the Turbomachinery Laboratory at Texas A&M University.

NOMENCLATURE

A, B	Imbalance planes
C	Bearing radial clearance [m]
D	Bearing diameter [m]
L	Bearing axial length [m]
N	Rotational speed [rad/s]
R	Bearing radius [m]
S	Sommerfeld number [-]
s	Shaft speed [rpm]
$\bar{u}_1$	Imbalance vector (magnitude and phase) at compressor C.G.
$\bar{u}_2$	Imbalance vector (magnitude and phase) at turbine C.G.
W	Static load on bearing [N]
Z_1	Compressor nose axial location [m]
Z_2	Turbine end axial location [m]
$\bar{z}_1$	Synchronous (*1X*) response vector (magnitude and phase) at compressor nose
$\bar{z}_2$	Synchronous (*1X*) response vector (magnitude and phase) at turbine nose
α	Ring speed ratio (ring rotational speed/shaft speed) [-]
μ	Lubricant viscosity [Pa-s]

Subscripts

CG	Center of gravity
FRB	Floating ring bearing
i	Inner
J	Journal
M	Measured

o	Outer
P	Predicted
R	Floating ring

TABLE OF CONTENTS

Page

LIST OF FIGURES

Page

Page

Page

Page

LIST OF TABLES

CHAPTER I
INTRODUCTION

Automotive turbochargers (TCs) increase the power output of internal combustion engines by increasing the air to fuel ratio entering into the piston cylinders. TCs are common in diesel engines for automobiles, trucks and marine applications. Diesel engines have lower power-to-weight ratio compared to gasoline engines; thus, turbocharging becomes the most suitable way to improve performance [1]**.** In a TC, hot exhaust gases spin a turbine wheel connected through a shaft to a compressor wheel, thus providing additional air for the combustion process.

Figure **1** shows an assembly cut of a typical TC unit. Due to low production costs and ease of machining, TC assemblies are commonly supported on floating ring bearings (FRBs) or semi-floating ring bearings (SFRBs) which are prone to show one or two subsynchronous instabilities over a wide range of operating speeds [1-14].

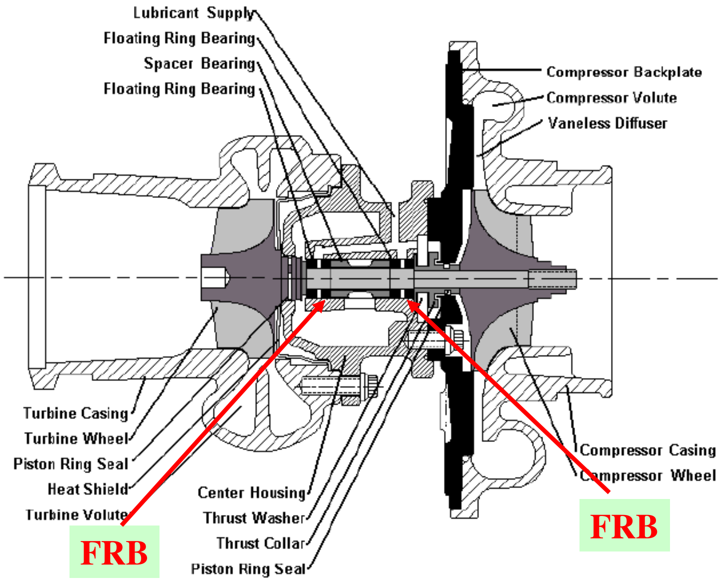

Figure 1 Overview of an automotive turbocharger unit [13]

This thesis follows the style of the Journal of Tribology

Figure 2 shows a typical FRB and SFRB configurations for TC units, comprising of a cylindrical sleeve between the journal and the bearing housing, thus creating two lubricant films. The subsynchronous whirl motions caused by the shearing of the two fluid films in series within each bearing, generally reach a limit cycle which enables the continuous operation of the TC [11]. In a SFRB configuration the floating ring is locked by a pin that allows it to precess but not to rotate, i.e. the outer lubricant film acts as a squeeze film damper.

The proper analysis of the dynamics of the rotor/bearing system is critical to improve current and new TCs designs. Thus, it is necessary to conduct nonlinear rotordynamics analyses since linear models are restricted to predict the synchronous response of motion, and not the amplitudes and multiple (subsynchronous) frequency components of shaft motion.

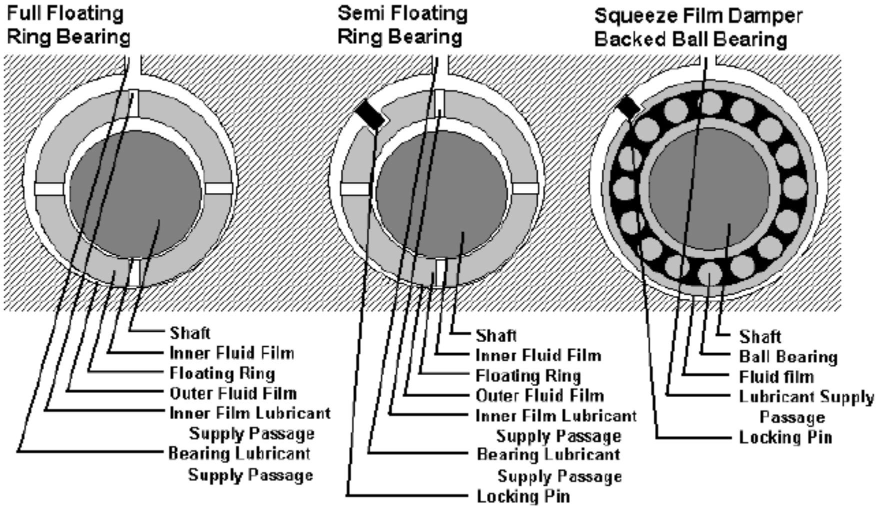

Figure 2 Floating and semi-floating ring bearings [13]

The physical analysis of FRBs is a critical element on the study of the dynamics of TCs. A complete fluid film bearing model accurately predicting FRB performance characteristics, i.e. floating ring speed, lubricant film temperature and viscosity changes, clearance thermal growth, power dissipation and operating eccentricities (floating ring and journal), is necessary to complement the linear and nonlinear rotordynamic tools. A comprehensive description of the static performance analysis for FRBs, including experimental and predicted results, is included in [11-14, 17].

Manufacturers produce a large number of TC units per year. Each unit type is tested to meet rigorous vibration standards before they can be distributed and used. This process is costly and time consuming. Thus, the present work seeks as its main goals to develop a computational model predicting the dynamic forced response of TCs and to facilitate a cost efficient product development. Identifying the source of mechanical problems prior to the manufacturing processes would allow the manufacturer to minimize unnecessary development costs.

CHAPTER II
LITERATURE REVIEW

Significant analytical and experimental research on the dynamic response and stability of high speed rotor-bearing systems supported on FRBs has been conducted for many years. The FRB comprises of a ring loosely inserted between the journal and casing surfaces, creating two lubricant films, inner and outer. The floating ring dynamic force performance is mainly dictated by the inner and outer film clearances, C_i and C_o, respectively. Viscous shear in the inner oil film causes the rotation of the floating ring while shear in the outer oil film retards its motion. Thus, the floating ring is subjected to the action of two drag torques in opposite directions; and, the floating ring rotates at a fraction of the journal velocity [1].

Born [2], presents an experimental and analytical study of the self-excited rotor vibrations originating from the fluid film bearings (FRBs) on a well balanced TC rotor. For an original FRB with outer to inner clearance ratio (C_o/C_i) of 1.55, the experimental results show a dynamically unstable rotor at shaft speeds above 8.2 krpm with increasing amplitudes of motion at the system natural frequency (136 Hz). Because this self-exited instability has a frequency of approximately half of the floating ring rotational speed, the probable cause may be a self-excited instability at the outer fluid film. The self-excited vibrations caused by the inner lubricant film are small in amplitude and disappear at shaft speeds above the system natural frequency. The stability analysis shows that the threshold speed instability is sensitive to small changes of the outer ring clearance, increasing the speed range of stable operation when the outer film clearance is reduced. Although, the inner ring related whirl frequencies could increase in amplitude due to the reduction in damping. Experimental data obtained for the same TC rotor supported on FRBs with a clearance ratio (C_o/C_i) of 1.33 agree with the analytical results from the stability analysis; i.e., the threshold speed of instability of the rotor-bearing system did not appear within the speed range.

In hydrodynamic journal bearings, the Sommerfeld number describes the equilibrium position of a rotor-bearing system at a rotational speed (*N*) in terms of the lubricant viscosity (μ), static load (*W*) and the geometrical characteristics of the bearing such as length (*L*), diameter (*D*) and clearance (*C*) [3], i.e.,

$$S = \frac{\mu NLD}{W}\left(\frac{L}{C}\right)^2 \tag{1}$$

In a floating ring bearing, the Sommerfeld numbers for the two fluid films are defined as:

$$S_i = \frac{\mu(N_J + N_R)LD_i}{W}\left(\frac{R_i}{C_i}\right)^2 \tag{2}$$

$$S_o = \frac{\mu N_R LD_o}{W}\left(\frac{R_o}{C_o}\right)^2 \tag{3}$$

$$S_o = \frac{\alpha}{1+\alpha}\left(\frac{R_o}{R_i}\right)^3\left(\frac{C_i}{C_o}\right)^2 S_i\,,\ \alpha = N_R / N_J \tag{4}$$

where S_i (equation 2) is the Sommerfeld number for the inner lubricant film dependant of the rotational speeds of the journal (N_J) and the floating ring (N_R). The Sommerfeld number for the outer lubricant film, S_o (equation 3), depends on the rotational speed of the floating ring (N_R). Note that total static load (*W*) is the same for the two lubricant films. Equation 4 gives a relationship between S_o and S_i [4].

Tanaka [5] presents a stability analysis for a floating bush bearing in which the full Sommerfeld condition is applied to the inner oil film due to the high rotational speed of the journal and the half Sommerfeld condition to the outer oil film. The full Sommerfeld solution predicts negative pressures in the divergent portion of the oil film mirroring the positive pressures in the convergent wedge. Half Sommerfeld truncates negative pressures but does not actually account for cavitation. The linear stability of the TC rotor is obtained for various floating bush bearing clearance ratios ($0.8 \leq C_o/C_i \leq 4.0$). The results indicate that for low clearance ratios ($C_o/C_i \leq 1.6$), the rotor-bearing system is unstable as soon as the shaft starts rotating, it then becomes stable at a higher speed, and as shaft speed increases, it becomes unstable again. The stable speed operation region can be extended with a larger clearance ratio ($C_o/C_i \geq 2.4$); and if properly designed, the floating ring journal bearing could have a region of stable rotor operation even to very high shaft speeds. The predictions show good agreement with the experimental results presented by Tatara [6]. On previous research, Tanaka and Hori [7] performed a theoretical analysis of a short length floating bush bearing with the half Sommerfeld condition for the two oil films. These assumptions lead to different stability characteristics which could not explain the stable operation of floating bush bearings at high rotational speeds.

The work presented in [1] also addresses predictions of the FRB static force performance The authors perform a theoretical analysis of the operating characteristics of a unidirectionally loaded FRB and present design charts with ring to journal speed ratios (N_R/N_J) for any value of Sommerfeld number (S_o) and various clearance ratios (C_o/C_i). The analysis shows that, except for low values of the Sommerfeld number, the ring speed does not depend on the clearance ratio (C_o/C_i). The experimental results presented agree well only with analytical predictions for the case of lightly loaded FRBs.

The adoption of isothermal flow models to predict the rotational speed of a floating ring has proven to yield poor results with respect to test data. Trippett and Li [8] conducted an experimental program to evaluate the effect of various bearing parameters on the floating ring speed and compare the test results to analytical predictions from an isothermal flow model. The test data recorded at low shaft speeds show agreement with analytical results, although as shaft speed increases the discrepancy between both enlarges as well. The authors compare the experimental results to predictions from a thermal flow analysis which includes variable lubricant viscosity as a function of the mean temperature across the film thickness, and present analytical data that is more in agreement with the experimental results. Further investigation on the performance characteristics of FRBs presented by Li [9] include an analytical study based on a numerical integration solution of the rotor-bearing equations of motion of a small rotor (similar to a TC rotor) supported on FRBs. The author compares the results to test data obtained for a similar rotor supported on cylindrical journal bearings. The results show that FRBs have lower power consumption than plain journal bearings and that increasing the fluid film radial clearances decreases the power consumption of the bearing, particularly when the inner film clearance increases. A transient response analysis demonstrates that the journal, ring and rotor all whirl with complex orbits of small amplitude (compared to the bearing clearance), and that increasing the imbalance magnitude increases the orbit size, operating shaft eccentricities and transmitted forces.

On a similar study to [9], Orcutt and Ng [4] calculate and measure the steady state and dynamic load properties of floating ring bearings. The analysis is performed for two outer to inner film clearance ratios (C_o/C_i = 0.7 and 1.3) and laminar flow conditions. The experimental results agree with the analytical data, which shows the existence of subsynchronous instabilities due to the floating ring bearings. The test data evidence orbital motions of the shaft in the ring with a whirling frequency of approximately 60% and 70% of the rotational frequency of the shaft. Sometimes the outer film becomes unstable so the ring orbits in the bearing clearance at approximately 50% of its rotational speed, resulting in more complicated orbits. The stability characteristics of the bearings improve when using a more viscous lubricant and also by avoiding large lubricant supply pressures. It is important to mention that the test bearing with the lowest clearance ratio (C_o/C_i = 0.7) shows more stable characteristics, agreeing with the results presented in [2].

Subsequent experimental results by Holt *et al.* [10] present measurements of casing acceleration on an automotive TC supported on FRBs running to a top speed of 115 krpm and driven by pressurized air at ambient temperature. The authors study the effects of increasing lubricant inlet pressure and temperature on the turbocharger rotordynamic response. An extensive analysis of the test data shows two rotordynamic instabilities (subsynchronous whirl motions). The onset speed of instability for the most severe subsynchronous motion is delayed with increasing feed pressure. On the other hand the lubricant supply temperature does not show any significant effect on the onset and end shaft speeds of rotordynamic instabilities. In a follow-up paper, Holt *et al.* [11] introduce two rotordynamic models, linear and nonlinear, to predict TC dynamic responses and correlate them with the experimental results previously obtained. The linear model predicts well the rotor free-free modes and onset speed of instability using linearized (inner and outer) film bearing force coefficients. The nonlinear model relies on the numerical integration of the equations of motion and calculates the transient response of the rotor. The results show limit cycle amplitudes with two subsynchronous whirl frequencies, further verifying that rotors supported on FRBs typically show two subsynchronous instabilities induced by the hydrodynamic action of the inner and outer fluid films.

Recently, San Andrés and Kerth [12] present a comprehensive model for prediction of FRB forced response, including a lumped-parameter thermal energy balance to determine the actual lubricant viscosity and thermal growth of the rotor, bearing and floating ring. The predictions for ring speed show a reasonable correlation to test data obtained for a TC with lubricant feed pressures of 69 kPa - 276 kPa and inlet temperatures of 27 – 49 °C. It is important to note that the predictions could be improved with a better estimation of the actual static load acting on the FRBs. On the other hand, the model predicts with high accuracy the lubricant exit temperature and power convected by the oil flow. Finally, the authors combine results from the thermal model with the nonlinear rotordynamic tools advanced in [11] to predict the TC dynamic response. The model predicts well the frequency content of the measured response presented in [11], although it over predicts their corresponding amplitudes of rotor response. The nonlinear model and test data demonstrate the persistence of two subsynchronous whirl frequencies at approximately 50% of the ring speed and 50% of the ring and shaft speed. A more detailed investigation of the bearing loading conditions based on the static equilibrium position and geometrical characteristics of the FRB is needed to better predict the dynamic forced response of TCs.

Kerth [13] presents a comprehensive investigation of the shaft motions encountered on a TC supported on FRBs, showing detailed comparisons between test data and predictions based on the rotordynamic and thermal models given in [11] and [12], respectively. The measurements of TC shaft motion and floating ring rotational speed are obtained from a TC test rig operating with cold shop air. The horizontal and vertical motion of the rotor is recorded by pairs of orthogonally positioned Eddy current sensors facing the TC shaft at the compressor and turbine rotor ends. Fiber-optic sensors measure the frequency of rotation of the lubricant feed holes on the ring outer race. The operating speed of the TC is controlled by a manually operated valve that supplies air to the turbine; an infrared tachometer mounted on the turbine outlet casing captures the shaft speed. Bourdon-type pressure gauges and thermocouples record the pressure and temperature at the inlet and discharge ports of the compressor and turbine. In addition, a pump delivers lubricant for the bearings from a temperature controlled reservoir while thermocouples sense the lubricant inlet and outlet temperatures. The author presents in detail the development and validation of the rotor structural model by comparing experimental against analytical results of rotor free-free modes and natural frequencies. The linear eigenvalue analysis shows four unstable roots (negative damping ratios); the first mode becomes unstable at a shaft speed of 15 krpm and the second at 25 krpm. These modes are characterized by forward whirling with an almost constant whirl frequency ratio (*WFR*) of 0.15, corresponding to approximately half the frequency of ring rotation; thus, indicating that the instability originates in the outer fluid film. The third and fourth modes are unstable at low shaft speeds (below 40 krpm), and becoming stable as shaft speed increases. Their corresponding frequencies are between the ring speed and the rotor speed, thus probably associated with the whirling in the inner lubricant film. The eigenvalue analysis also reveals two stable roots (critical speeds) at 23 krpm and 31 krpm, corresponding to the first and second bending modes of the rotor. It is important to mention that the predicted synchronous (1X) response to imbalance does not show the critical speed at 31 krpm, probably due to its high damping ratio (ξ = 0.74).

In [13], the results from the nonlinear analysis show that the TC system is unstable, although with amplitudes of motion that reach a stable limit cycle. The same results presented in the frequency domain (Fast Fourier Transforms) show the last 512 time steps of the transient, thus capturing the quasi-steady state response of the system. The time response at 60 krpm shows the fundamental frequency of the shaft motion at 147 Hz (whirl at approximately 50% of ring speed), correlating with the linear predictions for the first mode. On the other hand, the nonlinear analysis predicts the third and fourth eigenvalues to be unstable at rotor speeds above 45 krpm, differing from the results obtained by the linear analysis. The predictions of ring speeds are, in an average sense, in good agreement with the experimental results obtained for various lubricant supply pressures and inlet temperatures. The predicted amplitudes of shaft motion for increasing lubricant feed pressure do not reflect the test data showing amplitudes of vibration reducing as the oil feed pressure increases. The probable cause for this discrepancy is the improper modeling of the lubricant supply groove or inaccurate knowledge of the actual imbalance mass distribution.

San Andrés *et al.* [14] continue improving the predictions from the FRB thermal flow analysis and rotordynamic models advanced in [11-12]. For this purpose, the authors include accurate estimation of the hydrostatic loads (varying with shaft speed) acting on the FRBs due to lubricant feed pressure. The authors present shaft motion test data measured at the compressor nose of a TC supported on semi-floating ring bearings (SFRBs), i.e. the rotation of the ring is restricted by a locking pin. The latest linear and nonlinear predictions for lubricant feed pressures ranging from 100 kPa to 400 kPa at a nominal inlet temperature of 150 ^{o}C show a good correlation to available test data (amplitudes and frequencies). The experimental and computed results show that the synchronous (1X) motions are but a small fraction of the total shaft motion (at the compressor end) and large subsynchronous motions are persistent through the entire operating speed range. The predictions of synchronous (1X) amplitudes (linear and nonlinear models) are slightly smaller relative to the test data amplitudes; although the discrepancy can be attributed to the uncertainty in the imbalance masses and locations used in the analysis. The nonlinear predictions for subsynchronous whirl frequencies agree well with measurements, although predicting a third higher subsynchronous frequency not evident on the test data. More importantly, the results reveal that the unstable shaft motions correspond to excitations of the rotor conical mode and its harmonics.

This thesis presents progress on the development of linear and nonlinear rotordynamic and fluid film bearing models introduced and used in [11-14] to accurately predict the dynamic shaft response of a TC rotor (GT37 TC) supported on FRBs. The results show significant improvements in predicting the TC shaft motions, in particular with the proper estimation of the operating (inner and outer) film clearances and the side loads due to lubricant feed pressure.

CHAPTER III

TURBOCHARGER STRUCTURAL MODEL USING FINITE ELEMENT ROTORDYNAMIC SOFTWARE

This chapter describes the FE structural model of a GT37 TC unit using an in-house rotordynamic software, XLTRC^2 [15]. The physical properties of the rotor assembly are used to create a lumped FE model to predict the dynamic forced response of the rotor/bearing system. Measurements of the rotor free-free modes and natural frequencies are performed in order to validate the rotordynamic model

The second section describes the modeling of the floating ring bearings (FRBs) using a computational fluid-film bearing model, XLSFRBThermal® [16], for predicting FRB performance parameters with linearized and inner and outer film force coefficients (stiffness and damping) for a specified static load.

The analysis of the FRBs is critical on the study of the dynamics of the rotor/bearing system; for this reason great attention is taken to model correctly the inner and outer lubricant films. The FRB modeling includes calculations of hydrostatic side loads using XLHYPAD© [18]. The varying hydrostatic loads acting on the FRBs are calculated for shaft eccentricities ranging from -85% to 85% of the outer film clearance, thus estimating the loads from the lowest to highest shaft speeds.

The third section presents the results from the fluid-film bearing model, including predicted ring speeds, lubricant temperature and viscosity changes, power dissipation at the lubricant films and eccentricities for the ring and journal. Predictions and measurements of ring speeds are presented for three lubricant feed pressures, 158, 206, 272 kPa and inlet temperatures ranging from 32 °C to 46 °C. The effect of the lubricant feed pressure and inlet temperature on the bearing performance is investigated. Finally, an analytical procedure for estimating the actual imbalance on the turbocharger rotor is given. The procedure is based on the influence coefficient method for balancing a rotor as described in [20].

Finite element rotor-bearing system model

Figure 3 shows the GT37 TC rotor assembly. Fully-floating ring bearings (FRBs) support the rotor at two locations near the turbine and compressor wheels. The total weigh of the TC is 6.03 N and its center of gravity (CG) is located 113.34 mm from the compressor end. The compressor and turbine FRBs are located at 29.67 mm and 8.20 mm from the rotor C.G, respectively (distances measured from the FRBs mid planes). Hence, the fractions of rotor weight acting on the compressor and turbine FRBs equal 1.38 N and 4.30 N, respectively. Table 1 shows relevant dimensions of the TC rotor.

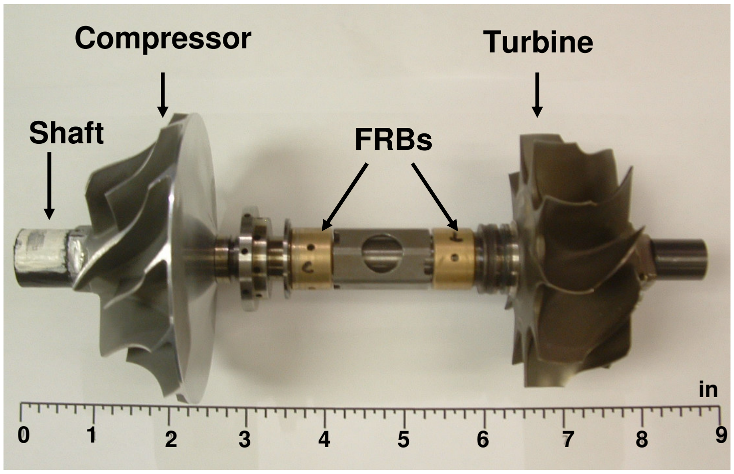

Figure 3 GT37 Turbocharger rotor

Table 1 Dimensions of TC components

Part	Length (mm)	Mass (grams)	C.G. Location from compressor end (mm)
Compressor wheel	48.6	131.5	29
Turbine wheel	56.0	382.0	151
Thrust collar	20.7	37.0	61
Compressor - FRB	11.2	15.0	83
Turbine – FRB	11.2	15.0	122
Total rotor	193	580.5	113.4

Figure 4 displays the TC rotordynamic structural model. The model includes lumped masses for the compressor and turbine wheels and the thrust collar. 42 finite elements (43 stations) model the rotor, and 2 elements for each floating ring bearing. The spring-connections represent a fluid film bearing. Note that only the outer fluid films are visible in the graph. The inner film connections can not be distinguished due to their small clearance.

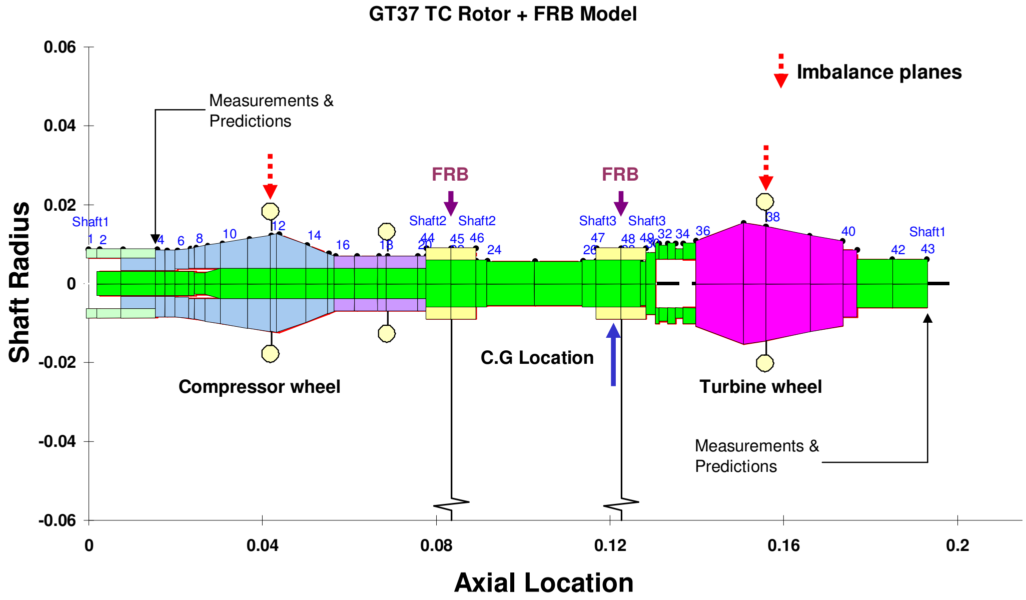

Figure 4 Rotordynamic model for GT37 TC rotor. Location of imbalance planes noted

The rotordynamic model includes imbalance masses located on the compressor and turbine wheels C.G. locations, stations 11 and 38, respectively. Table 2 shows the mass imbalance distribution for the TC. The method by which the imbalance masses and phase angles are determined is described later in this chapter.

Table 2 Imbalance distribution for TC rotor

Station #	Amount (gram-mm)	Phase (deg)	Description
11	2.1	-171°	CW C.G
38	6.04	-12°	TW C.G
Obtained from test data at a lubricant feed condition equal to 206 kPa and 38 °C. Multiple speed analysis at 60, 62.5 and 65 krpm			
14	2.74	111°	CW Backface
36	0.635	312°	TW Backface
Imbalance specified by project sponsor company (October 2003)			

The free-free mode shapes and natural frequencies of a rotor distinguish the response of the rotor in the absence of any support and no rotation. A good correlation between experimental and predicted values is essential to validate the rotordynamic model. Figure 5 depicts the measured and predicted first free-free mode shape for the TC rotor without the thrust collar. The first natural frequency is measured at 640 Hz; the predictions give 688 Hz, agreeing well with the experimental results. The compressor nose shows larger deflections than the turbine end, i.e. the shaft is more flexible at the compressor end. The normalized amplitudes indicate that the turbine end deflections are approximately 50% smaller in amplitude compared to those at the compressor nose.

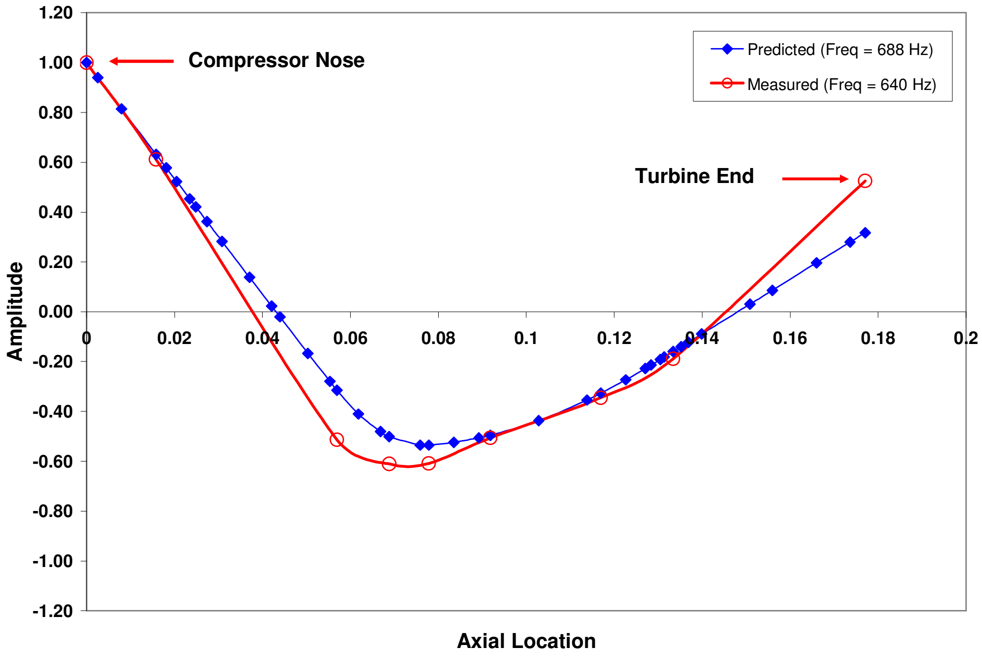

Figure 5 Measured and predicted first free-free mode shape and natural frequency for TC rotor

Figure 6 shows the measured and predicted second free-free mode shape and natural frequency for the TC rotor without the thrust collar. The largest deflections occur at the turbine end, being approximately 35% higher than the deflections at the compressor nose. Note that the second largest deflection is measured at an axial location of 117 mm, which coincides with the location of the turbine floating ring bearing. The predicted and measured second natural frequencies are 2,016 Hz and 2,190 Hz, respectively. The predicted second free-free mode shape shows slightly smaller deflections than the measurements at the turbine end, although similar amplitudes are predicted along the remaining axial length of the TC rotor.

Hence, the good correlation between predicted and measured results confirms that the rotordynamic model is adequate to conduct the linear and nonlinear response analyses. It is important to mention that the measurements were performed at room temperature. Hence, the rotor material properties replicate this condition.

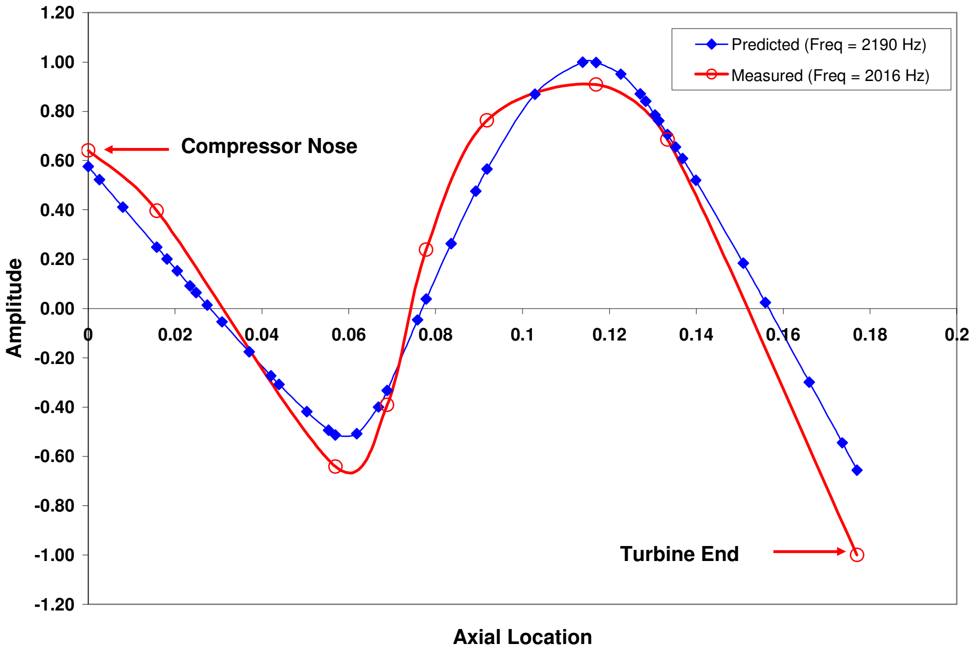

Figure 6 Measured and predicted second free-free mode shape and natural frequency for TC rotor

Modeling of floating ring bearings

The floating ring bearings (FRBs) are modeled with an updated version of the bearing thermal flow model (XLSFRBThermal® Version 5) advanced in [12]. The program calculates the FRB static performance parameters based on the static equilibrium state of the bearing for a specified shaft speed range. Detailed descriptions of the physical model are given in [12] and [16]. The original model includes a lumped-parameter thermal energy balance to determine the actual lubricant viscosity and thermal growth of the rotor, bearing and floating ring. The FRB rotordynamic force coefficients for the inner and outer films, necessary for the linear stability analysis (eigenvalues) and calculation of the synchronous (*1X*) response to imbalance, are also an output of the thermal flow model.

In addition to the characteristics of the original bearing model in [12], the updated version of the program considers the effect of hydrostatic side loads (due to lubricant feed pressure) acting on the floating rings. The TC bearing housing has two half-moon grooves for lubricant supply to the bearings. Figure 7 shows the schematic view of the outer film bearing modeled in XLHYPAD©[1]. This software aids in the calculation of the side loads due to hydrostatic pressurization using as inputs the bearing geometry, supply pressure and lubricant properties.

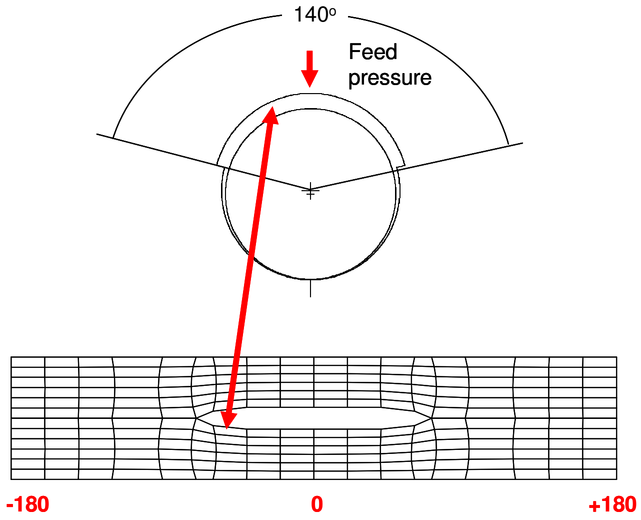

Figure 7 Outer film bearing configuration for estimation of side loads (XLHYPAD©)

Figure 8 shows the predicted hydrostatic loads for eccentricities ranging from -85% to 85% of the outer film nominal radial clearance (0.048 mm). The side load factor

---

[1] Part of XLTRC^2 Software Suite

at the centered ring condition equals to 10.7 N/bar for the compressor and turbine FRBs. In this study, the centered condition is representative of TC operation at a high shaft speed (70 krpm). Note that the TC is designed to operate to a maximum speed of 150 krpm. At a highly eccentric conditions (e/c = 0.85) representing low shaft speeds (10 krpm), the side load factor is calculated as 9.3 N/bar for the compressor and turbine FRBs.

Table 3 shows the relevant physical properties of the FRB and housing half moon groove used as inputs for calculating the hydrostatic side load.

Table 3 Compressor floating ring bearing dimensions

	Parameter	mm
A.	Journal Diameter	11.508
B.	Floating Ring Inner Diameter	11.543
C.	Floating Ring Outer Diameter	17.722
D.	Bearing Diameter	17.817
E.	Outer Film (Overall) Length	11.30
F.	Inner Film (Overall) Length	8.80
G.	Lubricant Feed Hole Diameter	2.00
	Number of Lubricant Feed Holes	4

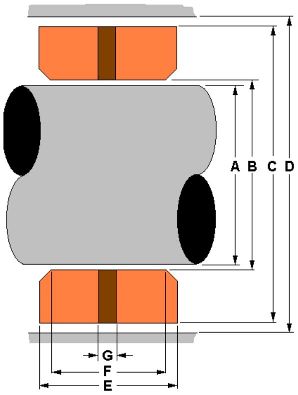

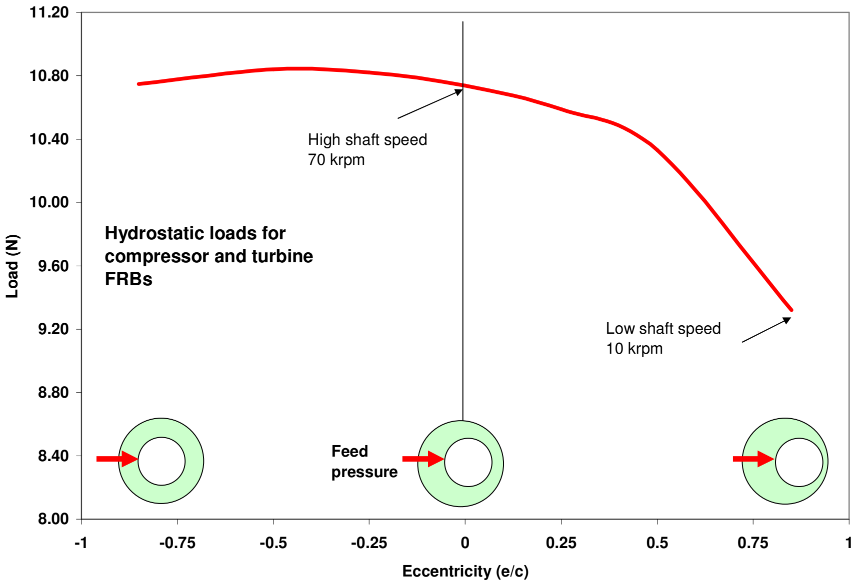

Figure 8 Predicted side loads for varying outer film ring eccentricities. Feed pressure equals 1 bar

Table 4 presents the inputs for the compressor FRB as used in the fluid film bearing program. Material properties for the ring, casing and rotor are also included. The “thermal model” is set as to represent an adiabatic shaft and the “bearing model” as to account for FRB lubricant supply at the bearing midplane. Note that the *X* and *Y* “pin” stiffnesses are zero for a fully-floating ring bearing configuration (no locking pin or mechanism). The fluid-film bearing model also accounts for the lubricant pressure loss at the inner film due to centrifugal flow effects through the feed orifices.

Table 4 Dimensions of compressor FRB, outer and inner films, and operating conditions (Set of inputs to XLSFRBThermal®)

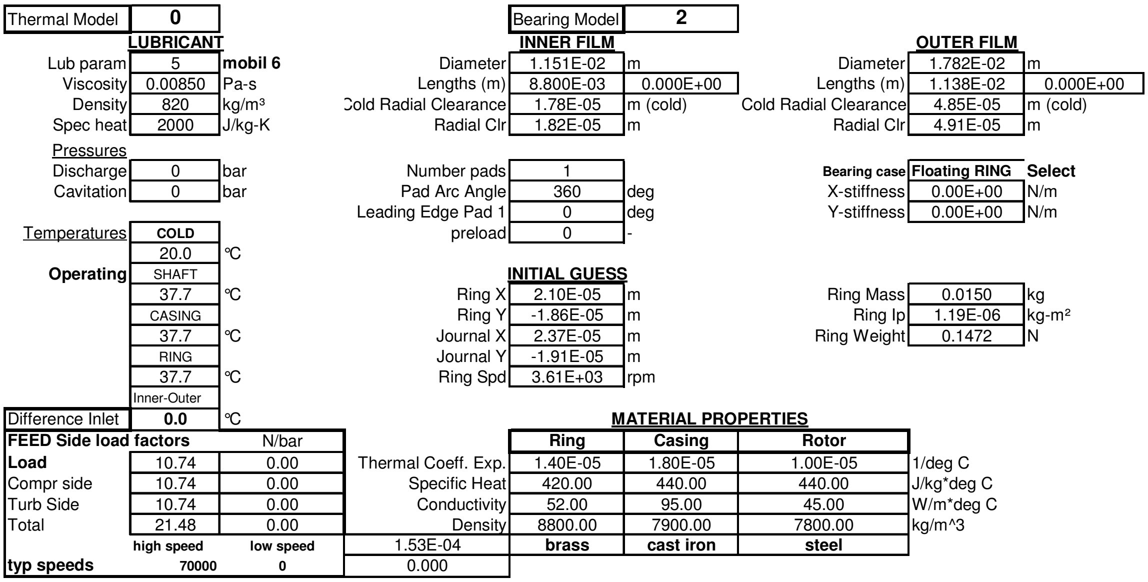

Thermal Model	0	
	LUBRICANT	
Lub param	5	**mobil 6**
Viscosity	0.00850	Pa-s
Density	820	kg/m³
Spec heat	2000	J/kg-K
Pressures		
Discharge	0	bar
Cavitation	0	bar
Temperatures	**COLD**	
	20.0	°C
Operating	SHAFT	
	37.7	°C
	CASING	
	37.7	°C
	RING	
	37.7	°C
	Inner-Outer	
Difference Inlet	**0.0**	°C

Bearing Model	**2**	
	INNER FILM	
Diameter	1.151E-02	m
Lengths (m)	8.800E-03	0.000E+00
Cold Radial Clearance	1.78E-05	m (cold)
Radial Clr	1.82E-05	m
Number pads	1	
Pad Arc Angle	360	deg
Leading Edge Pad 1	0	deg
preload	0	-
	INITIAL GUESS	
Ring X	2.10E-05	m
Ring Y	-1.86E-05	m
Journal X	2.37E-05	m
Journal Y	-1.91E-05	m
Ring Spd	3.61E+03	rpm

	OUTER FILM	
Diameter	1.782E-02	m
Lengths (m)	1.138E-02	0.000E+00
Cold Radial Clearance	4.85E-05	m (cold)
Radial Clr	4.91E-05	m
Bearing case	**Floating RING**	**Select**
X-stiffness	0.00E+00	N/m
Y-stiffness	0.00E+00	N/m
Ring Mass	0.0150	kg
Ring Ip	1.19E-06	kg-m²
Ring Weight	0.1472	N

FEED Side load factors		N/bar
Load	10.74	0.00
Compr side	10.74	0.00
Turb Side	10.74	0.00
Total	21.48	0.00
	high speed	**low speed**
typ speeds	**70000**	**0**

MATERIAL PROPERTIES

	Ring	**Casing**	**Rotor**	
Thermal Coeff. Exp.	1.40E-05	1.80E-05	1.00E-05	1/deg C
Specific Heat	420.00	440.00	440.00	J/kg*deg C
Conductivity	52.00	95.00	45.00	W/m*deg C
Density	8800.00	7900.00	7800.00	kg/m^3
1.53E-04	**brass**	**cast iron**	**steel**	
0.000				

Figure 10 and Figure 11 depict the measured and predicted compressor and turbine ring speed ratio (ratio of ring to shaft rotational speed), respectively, for lubricant feed pressures ranging from 206 kPa to 272 kPa and nominal inlet temperature of 38 ^{o}C. The measured ring speed ratios and shaft motion test data included in this work are given in [12]. Test data is available for four compressor housing angular orientations, namely 0^{o}, 40^{o}, 80^{o}, 120^{o}. Figure 9 shows a schematic view of the four compressor housing angular orientations for which the shaft motion test data was recorded.

For the purpose of this thesis, only the test data corresponding to a compressor housing orientation of 0^o is used in the remaining sections. Note that all tests were conducted using shop air (cold) to drive the turbine. Thus, the maximum shaft speed is much lower than in actual practice.

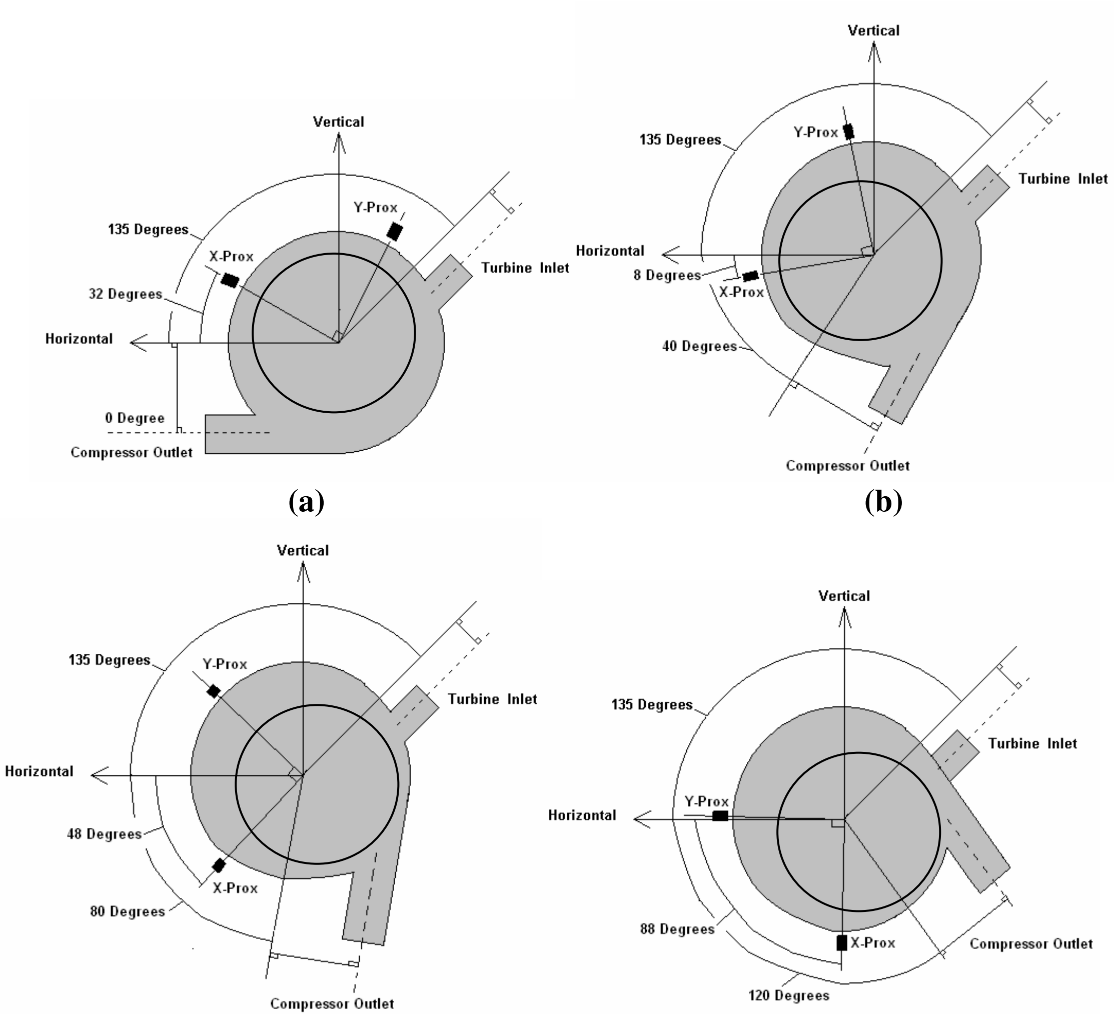

(a) **(b)**

(c) **(d)**

Figure 9 Compressor housing orientations for shaft motion measurements. (a) 0^o, (b) 40^o, (c) 80^o and (d) 120^o [19]

In the analysis, the shaft, casing and rings are assumed to be at the same temperature as the lubricant feed. The highest ring speed ratios, for both compressor and turbine FRBs, are measured and predicted at the lowest shaft speeds, decreasing in magnitude as the shaft speed increases. The test data shows that the compressor side FRB speed ratio suddenly drops from 40% to 30% of shaft speed equal to 30 krpm; the turbine floating ring shows a steadier decline in speed. Note that the experimental results show scattered points at high shaft speeds, indicative of faulty DAQ or more likely an indicative that the floating rings stopped rotating at high shaft speeds. A comprehensive discussion of the measured floating ring speeds can be found in [12, 19].

The floating ring rotational speed is governed by the viscous drag torque in each film. Changes in lubricant viscosity and speed dependant bearing clearances affect the shear torque, thus affecting the ring speed. The predicted ring speed ratios for the compressor and turbine side FRBs show no dependence on the lubricant supply pressure, agreeing well with the test data. However, the predictions for the compressor side FRB shows smaller ring speed ratios for shaft speeds ranging from 10 krpm to 30 krpm. In addition, the fluid film bearing analysis does not predict a zero rotational speed of the ring at the highest shaft speeds as observed in the test data. Measured ring speed ratios for the turbine side FRB show that the floating ring speed decreases steadily from 40% to 20% of the shaft speed, showing scattered data points at shaft speeds higher than 55 krpm.

The predicted ring speed ratios follow the test data trend line, showing good correlation for shaft speeds ranging from 20 krpm to 45 krpm. A better estimation of the hydrostatic loads acting on the FRBs would yield better correlation of predictions to test data. The rotational speed of the floating ring is directly proportional to the inner film lubricant viscosity and clearance. In addition, the drag torque in each film is also a function of its corresponding film clearances. Hence, thermal expansion of the journal, ring and bearing housing are properly accounted for in the calculation of the floating ring rotational speed.

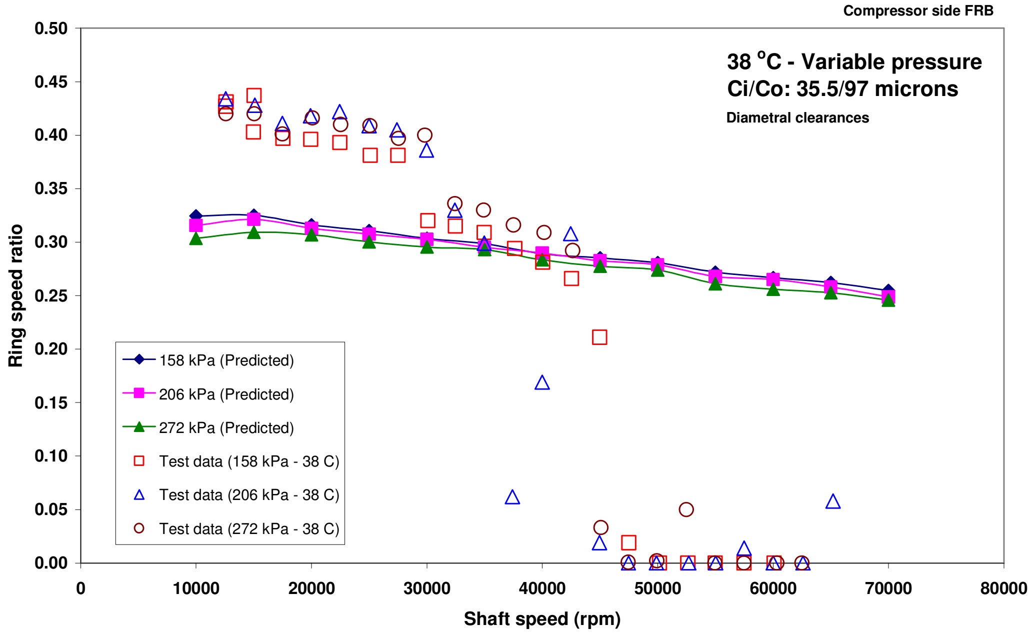

Figure 10 Predicted and measured ring speed ratios for compressor FRB. Variable lubricant feed pressure at a nominal inlet temperature of 38 ^{o}C. Measurements from [19]

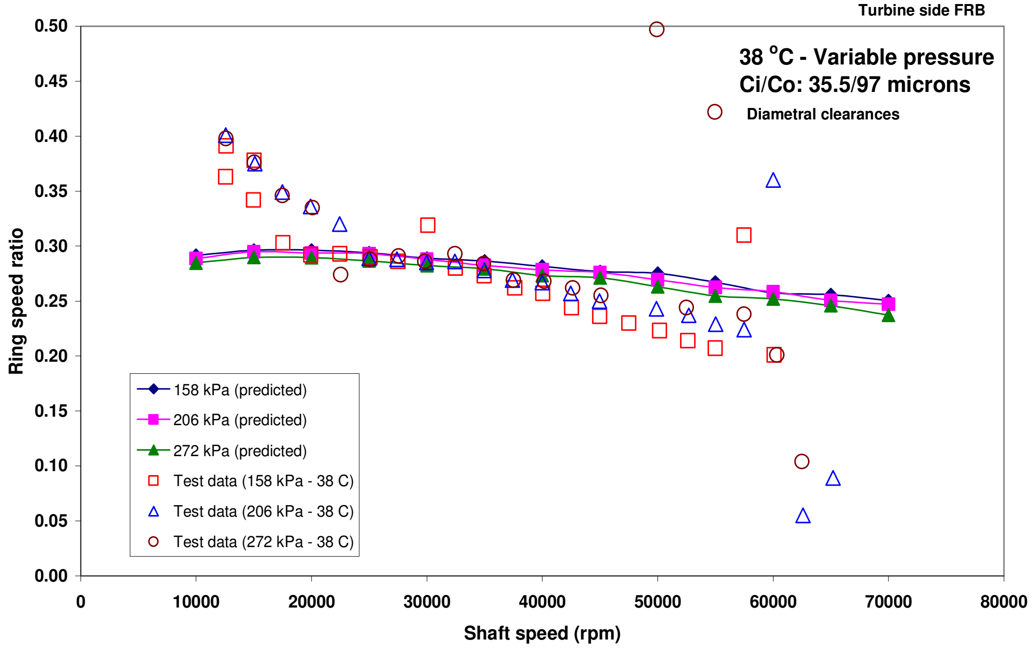

Figure 11 Predicted and measured ring speed ratios for turbine FRB. Variable lubricant feed pressure at a nominal inlet temperature of 38 ^{o}C. Measurements from [19]

Figure 12 and Figure 13 depict ring speed ratios for the compressor and turbine FRBs, respectively, for a constant lubricant feed pressure of 206 kPa and lubricant inlet temperatures ranging from 32 ^{o}C to 46 ^{o}C. The results indicate that the ring speed ratio does not change significantly for the lubricant temperature range considered. A more dramatic effect on the ring speed ratios is expected for higher operating temperatures due to thermal expansion of the bearing components.

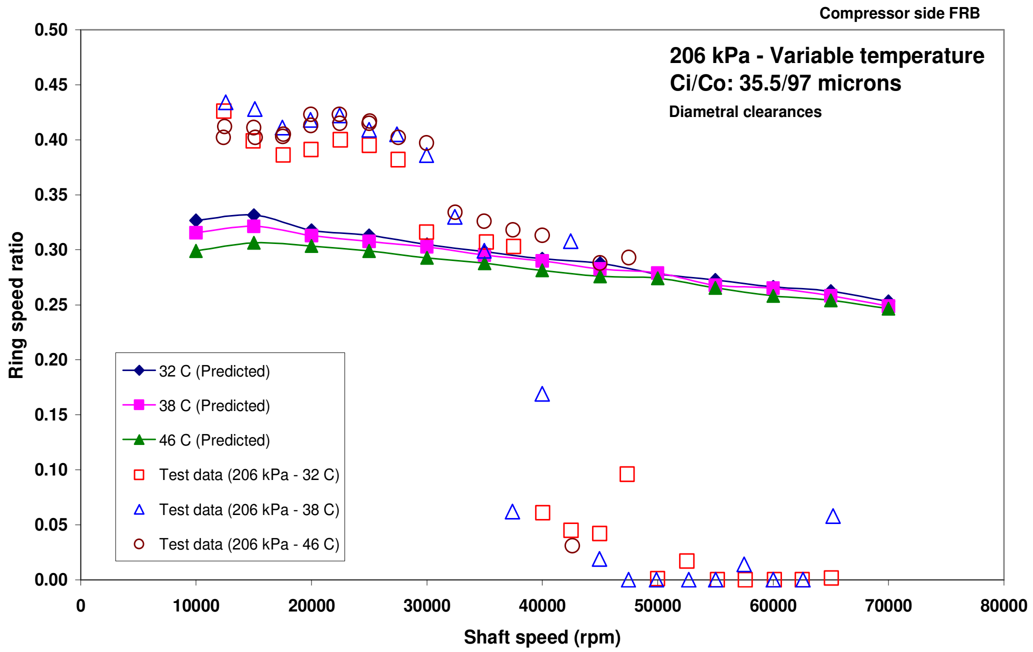

Figure 12 Predicted and measured ring speed ratios for compressor FRB. Variable lubricant inlet temperature at 206 kPa feed pressure. Measurements from [19]

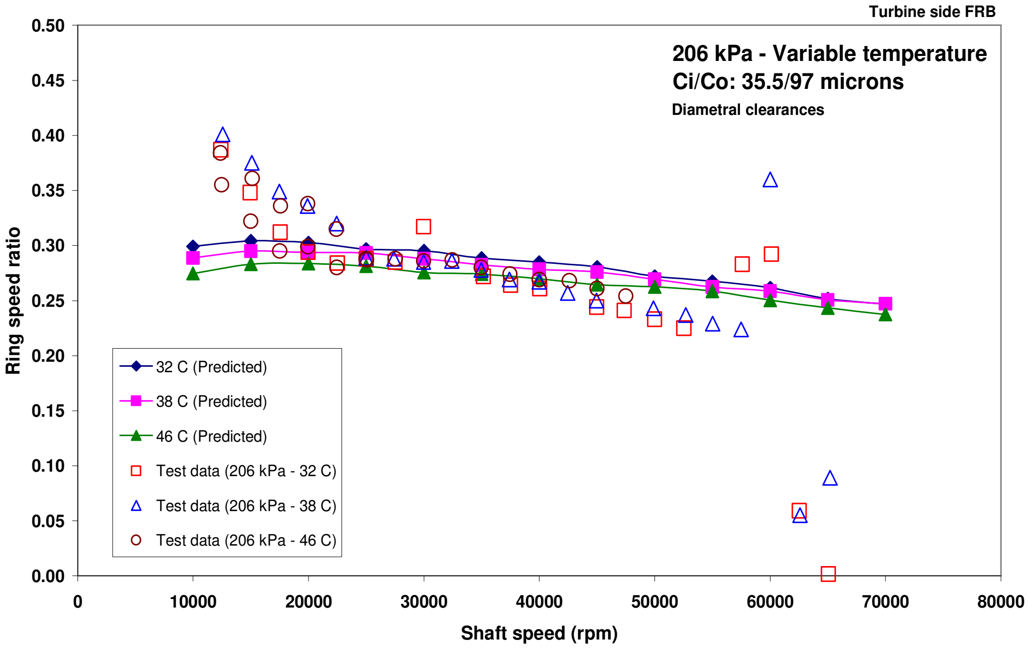

Figure 13 Predicted and measured ring speed ratios for turbine FRB. Variable lubricant inlet temperature at 206 kPa feed pressure. Measurements from [19]

Figure 14 shows a schematic view of the floating ring bearing thermal model. On the right side, lubricant flows into the inner and outer bearing clearances where mechanical power is consumed due to fluid shearing because of the rotating ring and journal. Consequently, energy is convected to the solids and conducted through the shaft, ring and bearing. On the left side, lubricant exits the bearing with higher energy and temperature; hence with a lower viscosity.

Figure 15 depicts predicted lubricant temperature raises at the inner and outer films of the compressor and turbine side FRBs for a lubricant feed pressure of 206 kPa and nominal inlet temperature of 38 ^{o}C. The lubricant temperature of the inner film increases at a much faster rate than at the outer film due to the smaller clearance and in particular due to the rotation of both ring and journal. At high rotor speeds, the mean temperature of the lubricant and bearing components is the highest since more mechanical energy is being consumed by the bearings. The hot stream of lubricant from the inner film mixes with the relatively cold stream of lubricant from the outer film at the exit of the bearing. Figure 16 shows predicted and measured lubricant exit temperatures for a lubricant feed pressure of 206 kPa and nominal lubricant inlet temperature of 38 ^{o}C. The predictions show good agreement with the test data, showing a rapid increase in temperature with shaft speed. At the highest shaft speed, 70 krpm, the lubricant temperature increases approximately 5 ^{o}C, demonstrating the FRB operates with relatively cool temperatures.

Effective lubricant viscosities for each film, inner and outer, of FRBs are illustrated in Figure 17 for increasing shaft speeds. Lubricant viscosity decreases due to the shear forces along the fluid film thickness which consequently increase the fluid mean temperature, in particular in the inner film. Note that both compressor and turbine side FRBs show similar lubricant effective viscosities along the shaft speed range considered.

Figure 18 shows the predicted power consumption of the inner and outer lubricant films for the compressor and turbine side FRB. The results are for a lubricant feed pressure of 206 kPa and nominal inlet temperature of 38 ^{o}C. The inner film consumes more energy than the outer fluid film due to its smaller clearance and higher speed. On the other hand, the lubricant contained within the outer clearance is only subjected to the shear caused by the rotation of the ring (casing is stationary), thus its power consumption is much lower than for the inner film. The viscous shear energy is converted into heat flow, which is carried away by the lubricant flowing through the inner and outer films, and most importantly conducted through the ring and bearing surfaces [17].

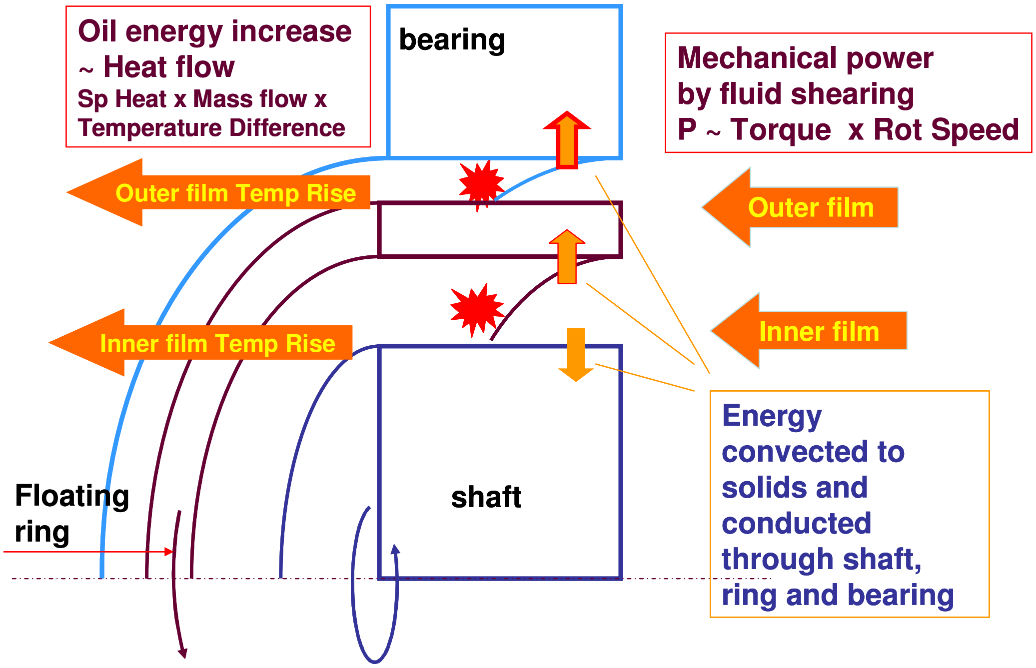

Figure 14 Schematic view of a floating ring bearing thermal model [17]

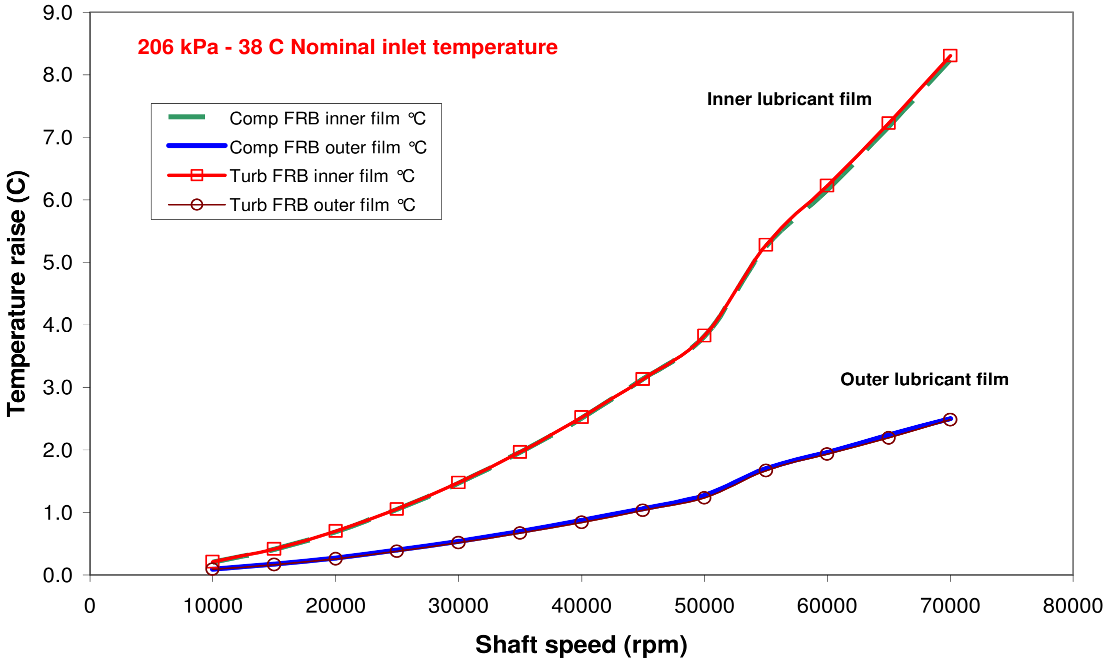

Figure 15 Predicted temperature raise at the inner and outer lubricant films (compressor and turbine FRBs). 206 kPa lubricant feed pressure, 38 ^{o}C nominal inlet temperature

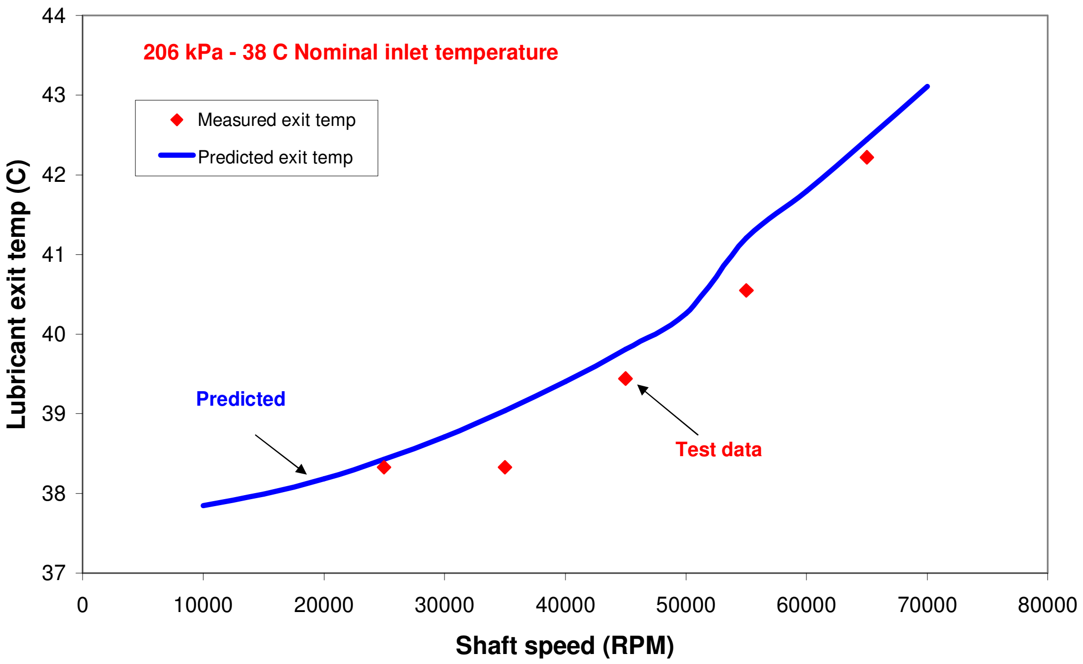

Figure 16 Predicted and measured lubricant exit temperature. 206 kPa lubricant feed pressure, 38 ^{o}C nominal inlet temperature

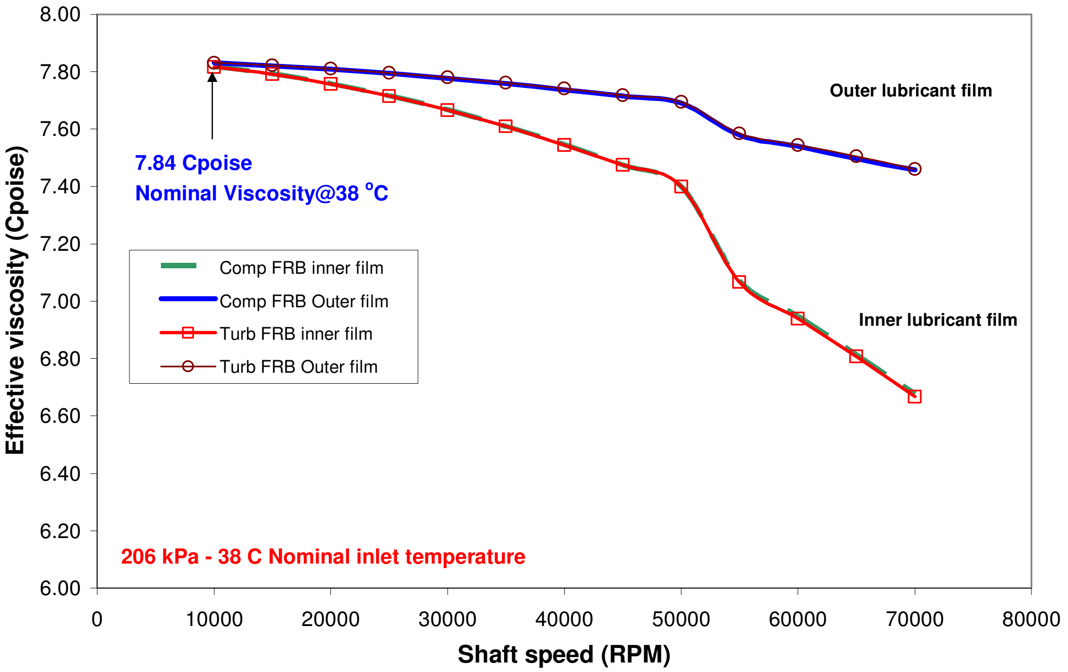

Figure 17 Predicted bearing effective viscosity (compressor and turbine FRBs). 206 kPa lubricant feed pressure, 38 ^{o}C nominal inlet temperature

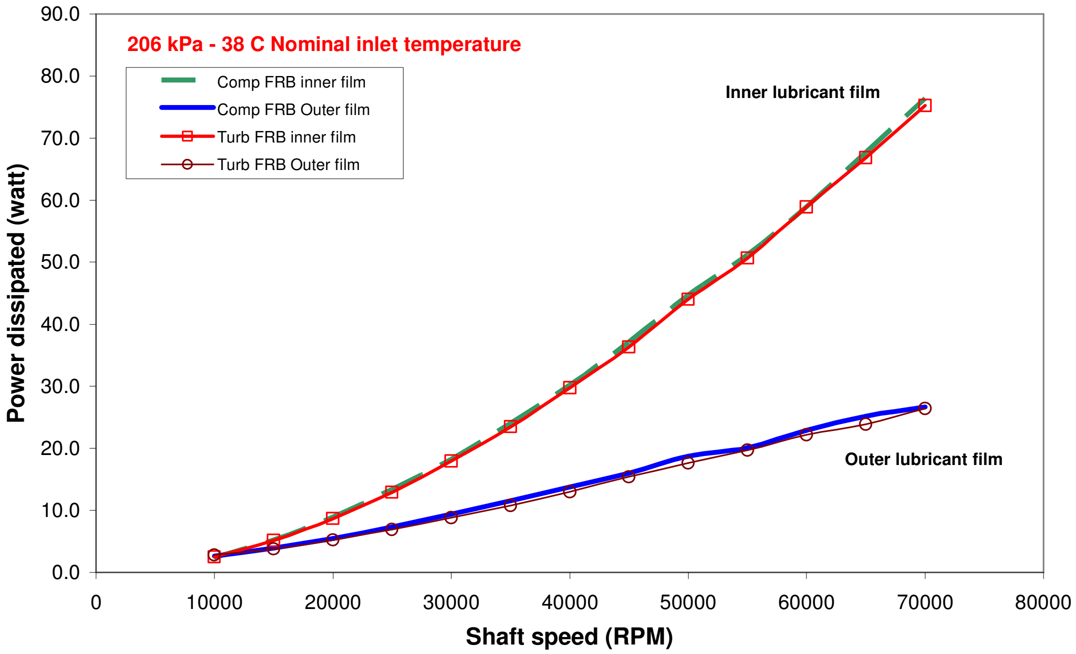

Figure 18 Predicted bearing power consumption (compressor and turbine FRBs). 206 kPa lubricant feed pressure, 38 °C nominal inlet temperature

Thermal expansion of the ring and bearing surfaces occurs as the lubricant temperature increases, consequently the operating clearances of the FRB change. Figure 19 shows the FRBs clearance changes relative to the nominal clearances (at test temperature) as functions of rotor speed. The inner film clearance increases while the outer film clearance decreases as shaft speed increases, indicating that the ring expands. Large inner film clearances result in smaller ring speed ratios since the lubricant shear decreases. A detailed analysis of the FRB heat transfer model is given by San Andrés [21].

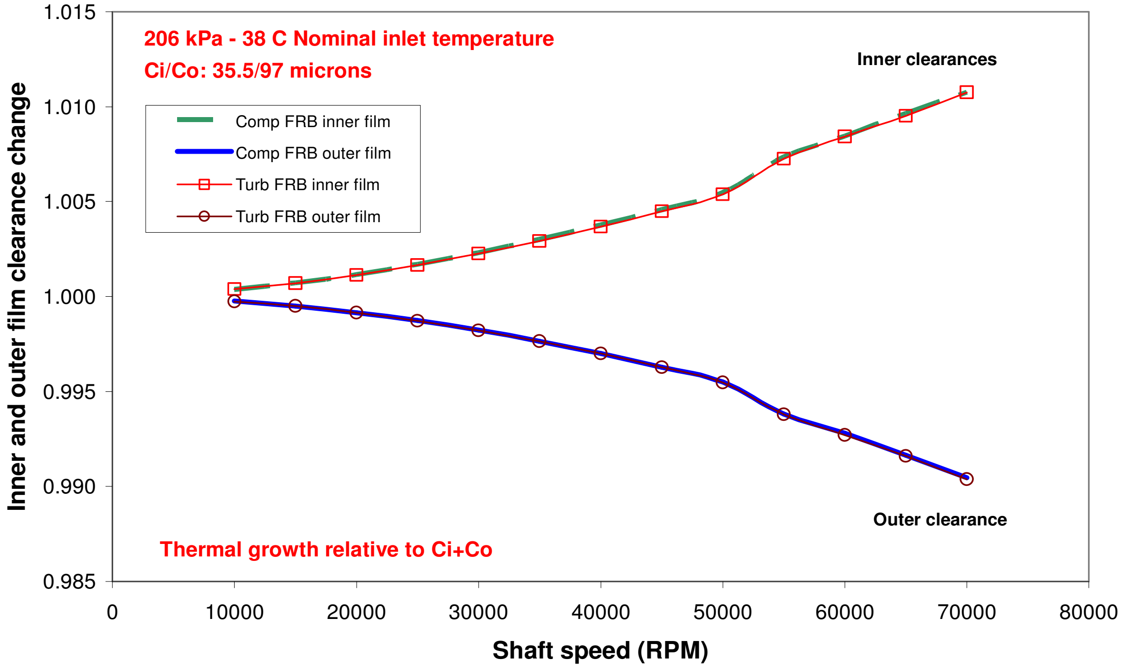

Figure 19 Predicted clearance changes with respect to nominal values. 206 kPa lubricant feed pressure, 38 °C nominal inlet temperature

Figure 20 depicts the lubricant inlet pressure loss due to centrifugal flow effects at the inner film of the compressor and turbine side FRBs. The results are for lubricant feed pressure and temperature of 206 kPa and 38 ^{o}C, respectively. At the lowest shaft speed, 10 krpm, lubricant enters the bearing lands at 206 kPa and as shaft speed increases the inlet pressure into the inner film decreases rapidly due to centrifugal flow loses. The predicted results show that lubricant inlet pressure to the inner film decreases to approximately 70% from the nominal supply pressure at the highest shaft speed (70 krpm). The lubricant inlet pressure into the outer film (not shown in graph) remains constant as shaft speed increases. As expected, the lubricant inlet pressure to the inner and outer films of the compressor and turbine FRBs are identical.

In plain cylindrical journal bearing, the eccentricity (*e*) indicates the relative position of the journal center with respect to the geometrical center of the bearing. Hence, the maximum eccentric position of the journal is the bearing clearance. Eccentricities larger than the bearing clearance indicate rubbing inside the bearing.

Figure 21 displays the predicted ring and journal eccentricities relative to the total radial clearance (nominal at test temperature) inside the bearing ($C_i + C_o$) for a lubricant feed pressure of 206 kPa and inlet temperature of 38 °C. At a shaft speed of 0 krpm, the journal and ring sit on the bottom of the bearing due to the weight of the rotor (static load) acting on each of the bearings in the direction of the gravitational force. When the shaft rotates, hydrodynamic pressure at the inner and outer films increases with the ring and journal rotational speeds, displacing both ring and journal towards the geometrical center of the bearing. Fluid film bearings operating at low eccentricities are more likely to become unstable than those operating at high eccentric positions. However, note that the hydrostatic load due to feed pressure, which increases with shaft speed, pushes the ring and journal to a high eccentric position particularly at low shaft speeds.

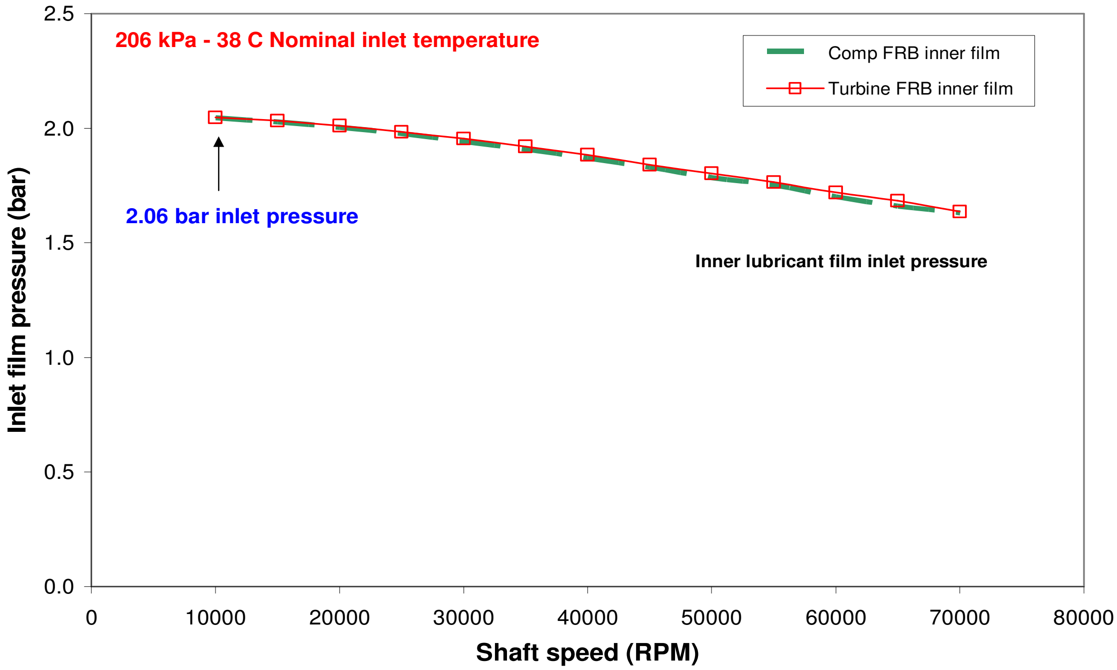

Figure 20 Predicted inlet pressure loss at inner film. 206 kPa lubricant feed pressure, 38 °C nominal inlet temperature

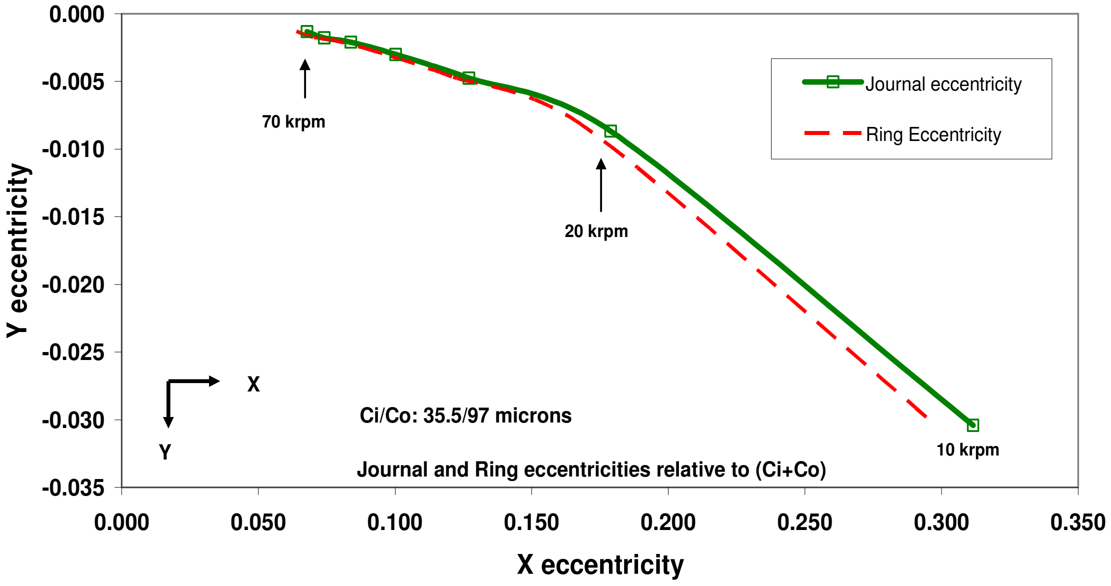

Figure 21 Predicted ring and journal eccentricities relative to total clearance (C_i + C_o) . 206 kPa lubricant feed pressure, 38 °C nominal inlet temperature

Influence coefficient method for estimating imbalance on the TC rotor

Due to the uncertainty on the actual TC rotor imbalance condition, it becomes necessary to devise a method which allows its reliable estimation. The following analytical procedure describes the approach used for estimating the imbalance on the test TC rotor. The procedure is based on the two plane balancing method with influence coefficients detailed by Vance [20].

Figure 22 shows a schematic view of the test turbocharger rotor. The locations of imbalance planes ***A*** and ***B*** are noted with arrows at the compressor and turbine wheel back faces. Measured synchronous (*1X*) response vectors are available for the compressor and turbine ends of the rotor. Hence, there are two locations of imbalances planes and two locations of shaft displacement measurements. The same imbalance and measurement plane distribution is used in the FE structural model.

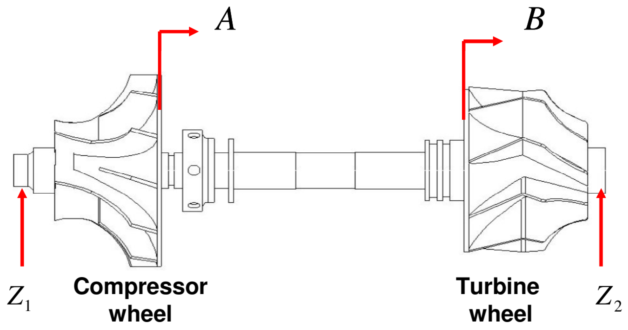

Figure 22 Location of imbalance and measurement planes on the rotor

A and *B* in Figure 22 are the two planes where imbalances $\overline{u}_1$ and $\overline{u}_2$ (magnitudes and phases) are located. For each imbalance $\overline{u}$, there is a synchronous (*1X*) response vector $\overline{z}$ (magnitude and phase) at the compressor (Z_1) and turbine (Z_2) ends of the TC rotor. Hence,

$$\overline{u} = |u|e^{\theta i} \Rightarrow \overline{z} = |z|e^{\alpha i} \tag{5}$$

Then, from [20] the two plane influence coefficient method for balancing a rotor is given by:

$$\begin{bmatrix} C_{11} & C_{12} \\ C_{21} & C_{22} \end{bmatrix} \begin{bmatrix} \overline{u}_1 \\ \overline{u}_2 \end{bmatrix} = \begin{bmatrix} \overline{z}_1 \\ \overline{z}_2 \end{bmatrix} \tag{6}$$

Where the left side of equation (6) is formed by a matrix of influence coefficients which represent the effect that an imbalance mass ($\overline{u}$) has on the synchronous response ($\overline{z}$) of the rotor. $\overline{z_1}$ and $\overline{z_2}$ represent the synchronous (*1X*) vibration vectors at the compressor and turbine ends of the TC rotor, respectively.

Assuming that the structural model of the TC yields accurate synchronous (*1X*) response predictions, it is then possible to obtain *predicted* synchronous vibration vectors $\overline{z}_{1_P}$ and $\overline{z}_{2_P}$ for unit imbalance masses located at imbalances planes *A* and *B*.

Note that the subscript *P* defines a predicted vibration vector. Using $\overline{u}1_A = 1\angle 0^0$ and $\overline{u}2_A = 0\angle 0^0$, the rotor model yields two predicted synchronous (*1X*) vibration vectors, one at the compressor end ($\overline{z}1_{PA}$)and one at the turbine end ($\overline{z}2_{PA}$) . Similarly, with $\overline{u}1_B = 0\angle 0^0$ and $\overline{u}2_B = 1\angle 0^0$ also yields two predicted synchronous (*1X*) vectors ($\overline{z}1_{PB}, \overline{z}2_{PB}$). Then, equation (7) can be expressed in terms of the predicted vibration vectors $\overline{z}1_P$ and $\overline{z}2_P$, i.e.,

$$\begin{bmatrix} C_{11} & C_{12} \\ C_{21} & C_{22} \end{bmatrix} \begin{bmatrix} \overline{u}1 \\ \overline{u}2 \end{bmatrix} = \begin{bmatrix} \overline{z}1_P \\ \overline{z}2_P \end{bmatrix} \tag{7}$$

Consequently, the influence coefficients follow as

$$C_{11} = \frac{\overline{z_{1_{PA}}}}{\overline{u_{1_A}}},\ C_{21} = \frac{\overline{z_{2_{PA}}}}{\overline{u_{1_A}}},\ C_{22} = \frac{\overline{z_{2_{PB}}}}{\overline{u_{2_B}}} \text{ and } C_{12} = \frac{\overline{z_{1_{PB}}}}{\overline{u_{2_B}}} \tag{8}$$

Equation (8) yields the influence coefficients from the specified unit imbalances and the predicted synchronous vibration vectors. From the test data, synchronous (*1X*) vibration vectors $\overline{z}1_M$ and $\overline{z}2_M$ are available and, since the influence coefficient matrix is known, it is possible to rewrite equation (7) such that it yields estimates of the imbalances $\overline{u}1$ and $\overline{u}2$ at the time of the measurements.

$$\begin{bmatrix} \overline{u}1 \\ \overline{u}2 \end{bmatrix} = \begin{bmatrix} C_{11} & C_{12} \\ C_{21} & C_{22} \end{bmatrix}^{-1} \begin{bmatrix} \overline{z}1_M \\ \overline{z}2_M \end{bmatrix} \tag{9}$$

Note that this analytical procedure calculates the imbalance masses that the structural model requires to reproduce the measured synchronous vibration vector at a *single* shaft speed (s). At high shaft speeds, the TC synchronous (*1X*) response most likely shows the imbalance on the TC rotor. Hence, this method can be extended to calculate the imbalances $\overline{u}1$ and $\overline{u}2$ from *multiple* speeds ($s_1, s_2, ..., s_N$), preferably high shaft speeds for the above mentioned reason. In this case, the three highest shaft speeds from the measurements are used to improve the accuracy of the calculations.

From equation (9), for each selected speed there is a 4x4 matrix of influence coefficients (C), a 2x1 matrix of calculated imbalances (u) and a 2x1 matrix of measured synchronous (*1X*) vibration vectors, i.e.,

$$\begin{aligned} C_1 u &= Z_{1M} \\ C_2 u &= Z_{2M} \\ C_3 u &= Z_{3M} \end{aligned} \tag{10}$$

The system in equation (10) is over determined, having more equations than unknown parameters. Thus, a Least Square (*LS*) method is applicable to resolve for the imbalance matrix u and to obtain $\bar{u}_1$ and $\bar{u}_2$.

$$u = A_{LS} Z_M \text{ where } A_{LS} = (C^T C)^{-1} C^T \quad \text{, with } C = \bigcup_{i=1}^{3} C_i \tag{11}$$

where A_{LS} in equation (11) results from the *LS* method and Z_M is a matrix that contains all the measured synchronous (*1X*) vibration vectors from equation (10). The imbalances calculated with this analytical method are given in Table 2, see page 14.

CHAPTER IV

ANALYSIS OF MEASURED TURBOCHARGER FORCED RESPONSE. SYNCHRONOUS AND SUB SYNCHRONOUS SHAFT MOTIONS

Measurements of TC shaft motion and floating ring rotational speed are reported in [19] using the cold air TC test rig at Texas A&M University described in [13]. The measurements were performed for lubricant feed pressures of 158, 206 and 272 kPa and inlet temperatures ranging from 32 ^{o}C to 46 ^{o}C. Eddy current sensors record the shaft displacement at the compressor and turbine ends, in the horizontal and vertical directions. The floating ring speeds are measured with fiber-optic sensors that detect the frequency of rotation of the lubricant feed holes on the outer race of the ring. Correct manipulation of the raw test data by computational means yields the components of synchronous (*1X*) and subsynchronous shaft motions.

This chapter presents a comprehensive discussion of the main characteristics observed in the measured TC shaft motions. The effect of varying operating conditions on the synchronous (*1X*) and subsynchronous vibrations is investigated. A comprehensive assessment of the synchronous response to imbalance yields the critical speed. On the other hand, the spectrum of subsynchronous vibrations contains the information regarding encountered instabilities. Available test data waterfall spectra are also presented to demonstrate the abundance of multiple frequencies of subsynchronous motion under which the TC operates in a limit cycle.

As for the ring speeds presented in the previous chapter of this thesis, test data is available for four compressor housing orientations, namely 0^{o}, 40^{o}, 80^{o}, 120^{o} with respect to the horizontal axis (refer to Figure 9). A complete discussion of the effects that the compressor housing orientation has on the TC shaft motions is given in [19]. The purpose of this chapter is to discuss the particular characteristics encountered in the recorded TC shaft motions. For this reason, only test data corresponding to a compressor housing orientation of 0^{o} is presented (refer to Figure 9). Adequate post processing of the test data is necessary to transfer the measured vibration amplitudes from the fixed sensors coordinate system to actual horizontal and vertical planes. In addition, all the test data amplitudes are shown in dimensionless form relative to the limit of maximum conical motion at the turbine end, namely 0.254 mm 0-pk. Hence, shaft motions with amplitudes equal to 1 indicate that the vibration level reaches 100% of the maximum physical limit and rubbing between components will occur.

Figure 23 and Figure 24 depict waterfall graphs of TC compressor and turbine shaft amplitudes of motion versus frequency for the horizontal and vertical directions, respectively. The test data corresponds to a lubricant feed pressure of 206 kPa and inlet temperature of 38 ^{o}C. The top graphs show the frequency content of the compressor end of the rotor while the bottom graphs correspond to the turbine end. The waterfalls show the multiple frequencies and amplitudes of motion for shaft speeds ranging from 12.5 krpm to 65 krpm. The waterfalls also show the multiple subsynchronous vibration components along the entire operating speed range for both compressor and turbine ends of the rotor.

The horizontal (X) and vertical (Y) shaft motions show similar amplitudes at both compressor and turbine ends with dominance of synchronous speed components. Although, as it will be discussed later, the synchronous ($1X$) vibration amplitudes at turbine end are larger than the synchronous ($1X$) motions at the compressor end. Note that the four waterfalls show subsynchronous frequencies that track the synchronous motions at a fraction of the shaft speed, indicative of oil whirl encountered in fluid film bearings. However, note that at the highest shaft speed (65 krpm) the compressor end shows the onset of a large subsynchronous amplitude with a frequency of approximately 50% of the shaft speed. This large amplitude of vibration is an indicative of oil whip which occurs when a subsynchronous frequency locks at a natural frequency of the system. It is important to note that the multiple frequency subsynchronous motions reach stable limit cycles enabling the continuous operation of the unit without failure.

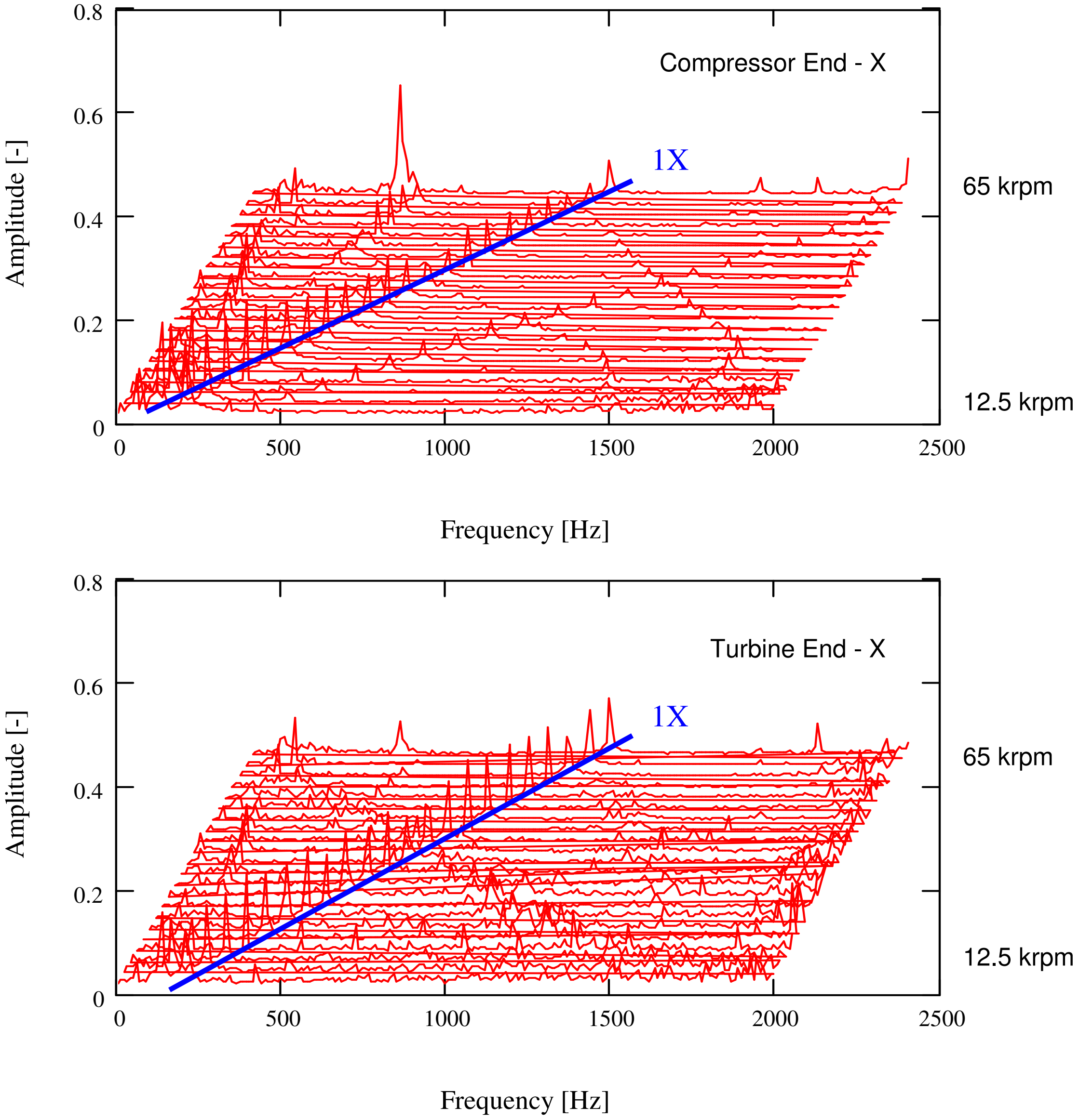

Figure 23 Waterfall of compressor (top) and turbine (bottom) horizontal shaft end motion. Oil inlet temperature 38 ^{o}C and feed pressure of 206 kPa [19]

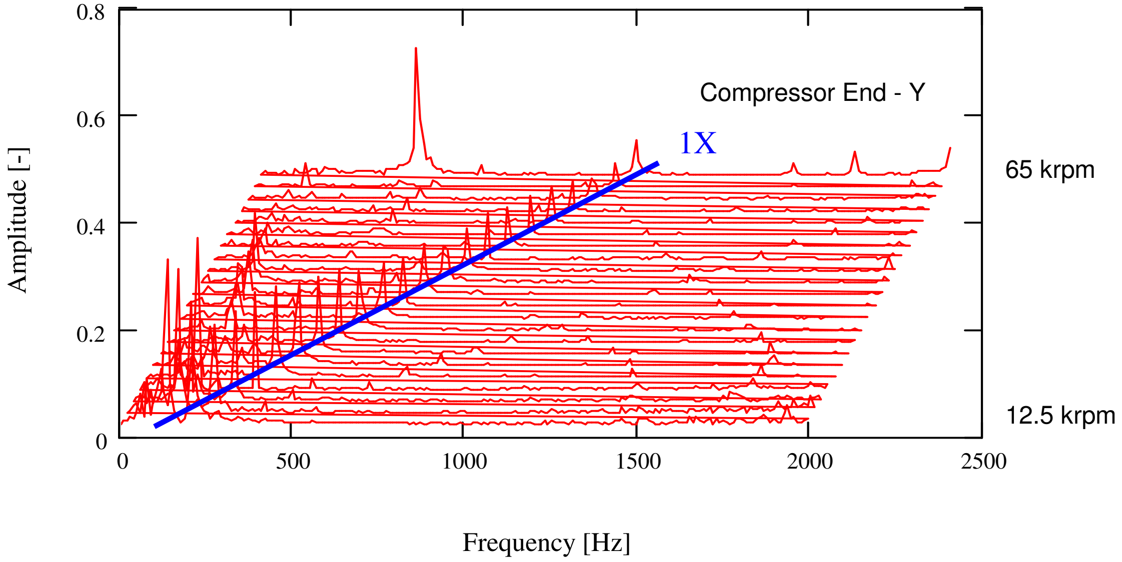

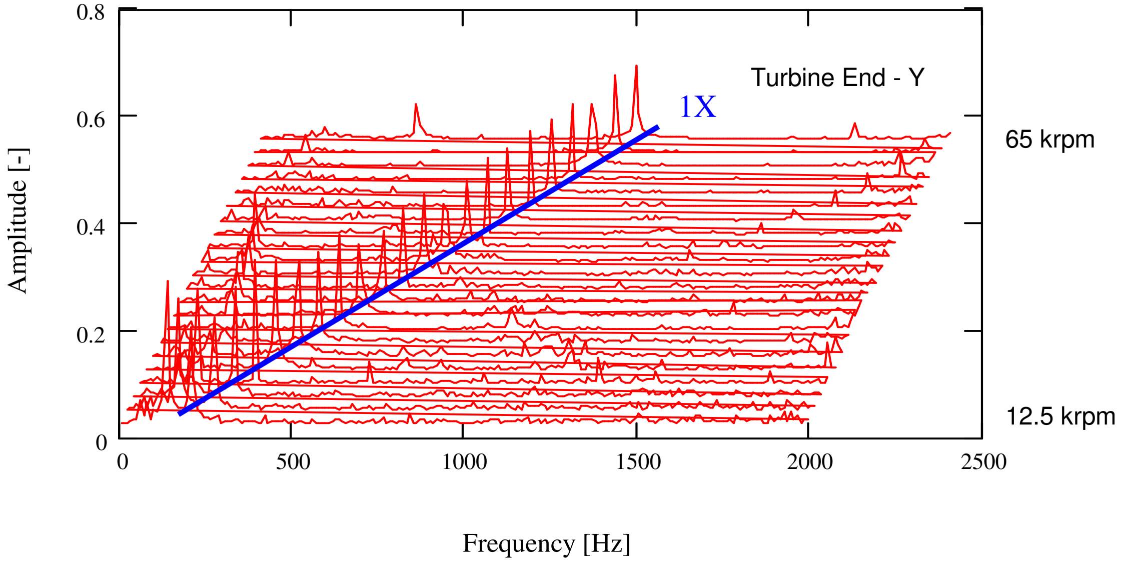

Figure 24 Waterfall of compressor (top) and turbine (bottom) vertical shaft end motion. Oil inlet temperature 38 ^{o}C and feed pressure of 206 kPa [19]

Figure 25 depicts the static motion (DC) for shaft speeds increasing from 12.5 krpm to 65 krpm. The results are for lubricant feed pressure of 206 kPa and inlet temperature of 38 °C. In the graph, the circular path with a radius of 1 corresponds to the approximate limit of maximum conical motion of the rotor at the turbine end. The static motion of both compressor and turbine shaft ends is presented relative to the position at the lowest rotational speed (12.5 krpm). At the lowest rotor speed, the shaft is located at origin (0,0) and as shaft speed increases the compressor shaft end moves initially downwards and then straight upward. Similarly, the turbine end of the rotor displaces upward and positions at a location close to the origin vertical axis (*Y*). Hence, both compressor and turbine shaft ends operate at similar vertical locations relative to the origin at the highest shaft speed (65 krpm).

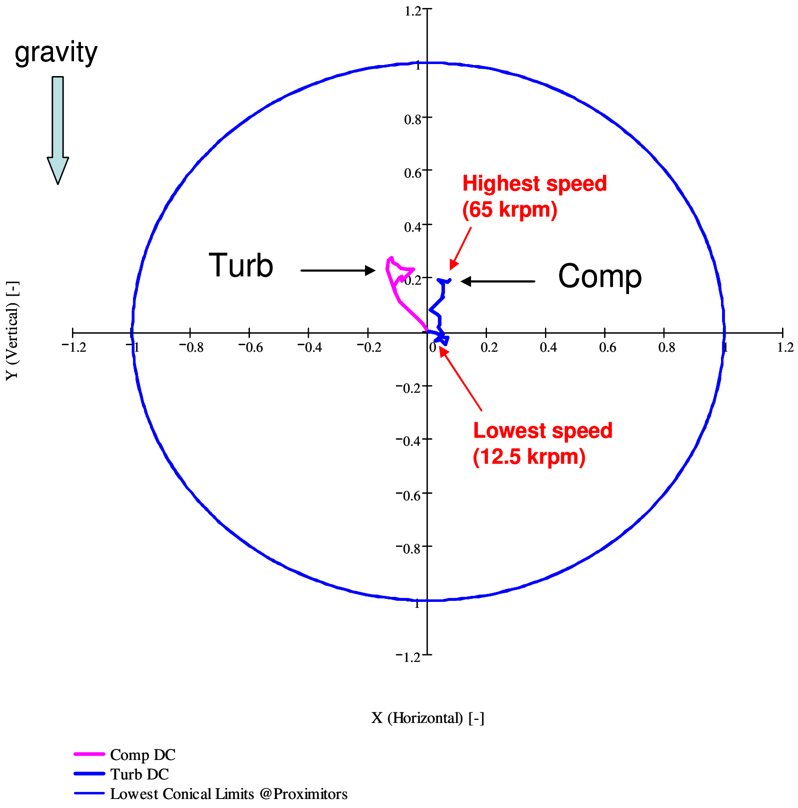

Figure 25 Static displacement of rotor (DC) from low (12.5 krpm) to top speed (65 krpm). Oil inlet temperature 38 °C and feed pressure of 206 kPa. Compressor and turbine shaft ends [19]

Figure 26 shows the dynamic portion of the shaft motion (orbits) at the highest shaft speed (65 krpm). As for the previous graph, the circular path with a radius of 1 corresponds to the approximate limit of maximum conical motion of the rotor at the turbine end. The dynamic amplitudes of motion (vibrations) are far more severe at the turbine shaft end than at the compressor end. Note, however, that the turbine horizontal and vertical amplitudes are of similar magnitude while the compressor end of the rotor shows larger vibrations along the vertical direction (*Y*) direction. The orbit recorded at the turbine end of the shaft is composed of the large amplitude synchronous (*1X*) vibration components and subsynchronous frequencies. On the other hand, the orbital motions at the compressor nose of the TC show more complex patterns clearly indicating the presence of subsynchronous frequencies.

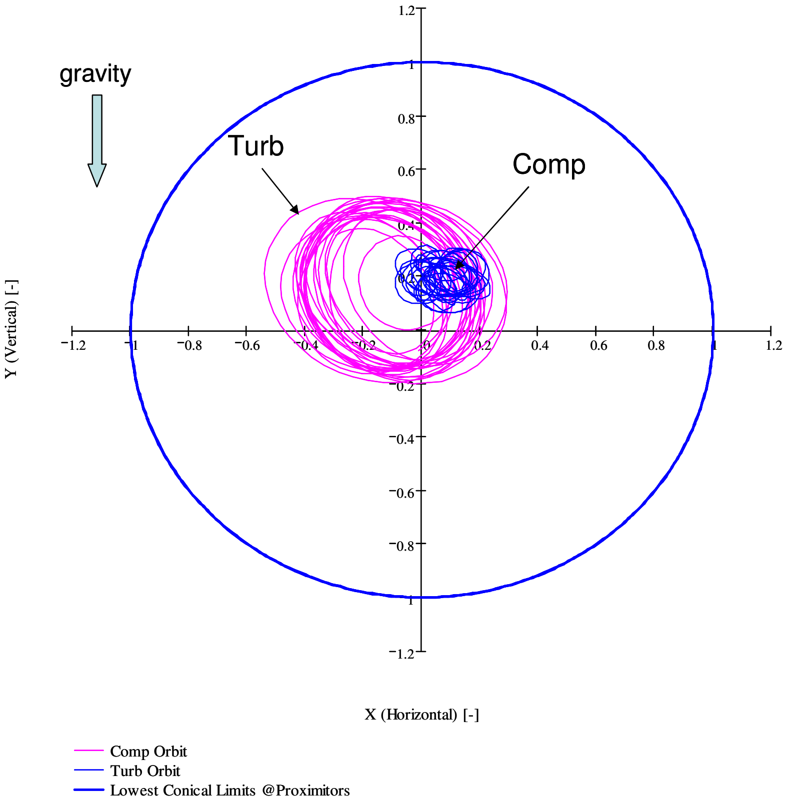

Figure 26 Orbital motion at top shaft speed = 65 krpm. Oil inlet temperature 38 ^{o}C and feed pressure of 206 kPa [19]

Figure 27 and Figure 28 show the *X* and *Y* peak values (dimensionless), respectively, of the measured motions at the compressor and turbine ends of the TC rotor for 206 kPa and 38 ^{o}C lubricant feed pressure and inlet temperature, respectively. In the figures, the rotor motions are decomposed into synchronous and subsynchronous vibrations components. The test data shows the synchronous (*1X*) and subsynchronous shaft motions along with their corresponding amplitudes of vibration. The larger amplitudes of vibration correspond to the synchronous (*1X*) response to imbalance. These motions decrease in amplitude as shaft speed increases. However, the *1X* amplitudes measured at the compressor nose of the rotor decrease at a faster rate than the synchronous vibrations measured at the turbine end of the rotor. Consequently, synchronous vibrations at the turbine end show larger amplitudes for the highest shaft speeds when compared to the response at the compressor end. Note that the amplitudes of subsynchronous motions are larger in the vertical (*Y*) direction for both compressor and turbine shaft ends, in particular at low shaft speeds (< 20 krpm), where the subsynchronous amplitudes are larger than the synchronous components. It is important to note that at low shaft speeds, just above two times the conical mode natural frequency, the subsynchronous amplitudes are significantly large.

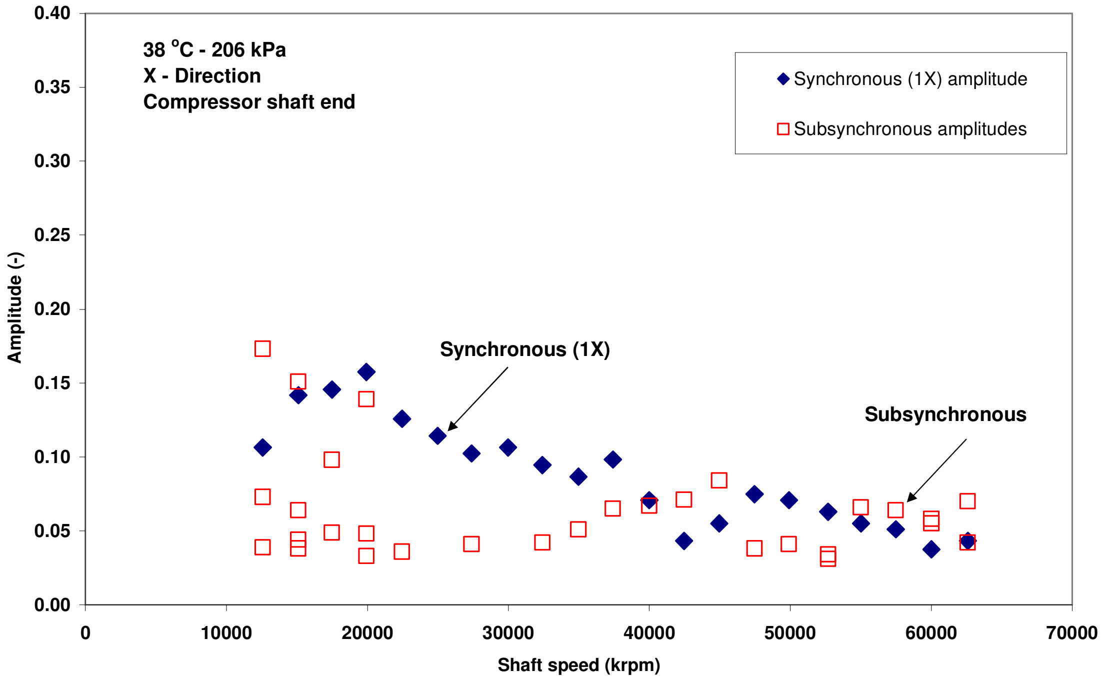

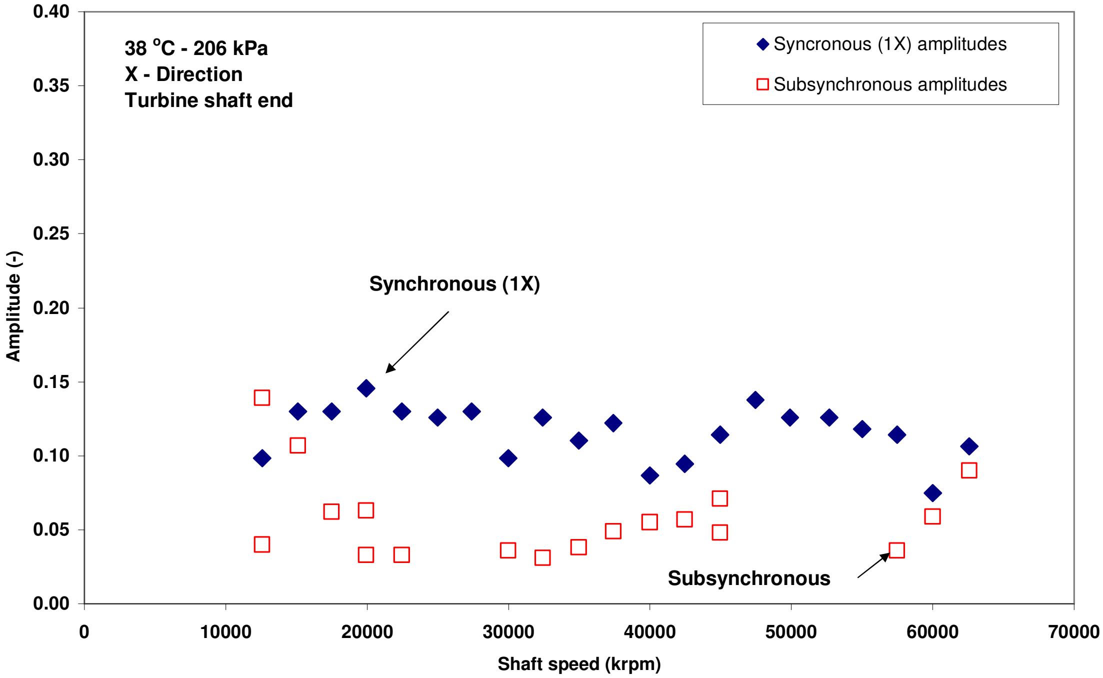

Figure 27 Synchronous and subsynchronous motions at compressor (top) and turbine (bottom) shaft ends (X-direction). Lubricant inlet temperature 38 °C and feed pressure of 206 kPa [19]

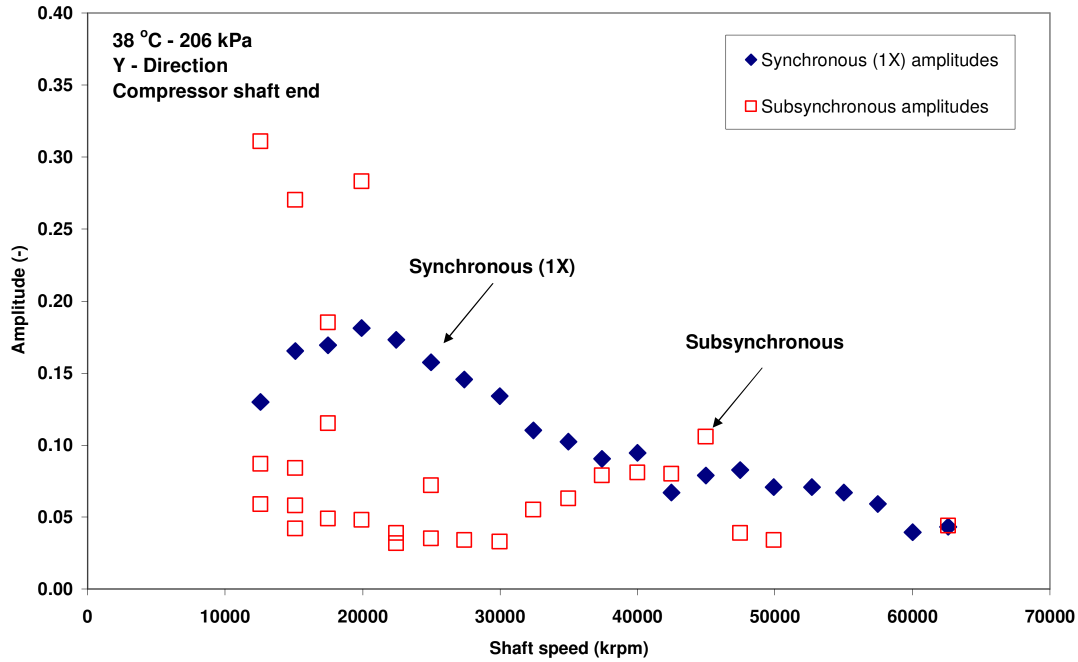

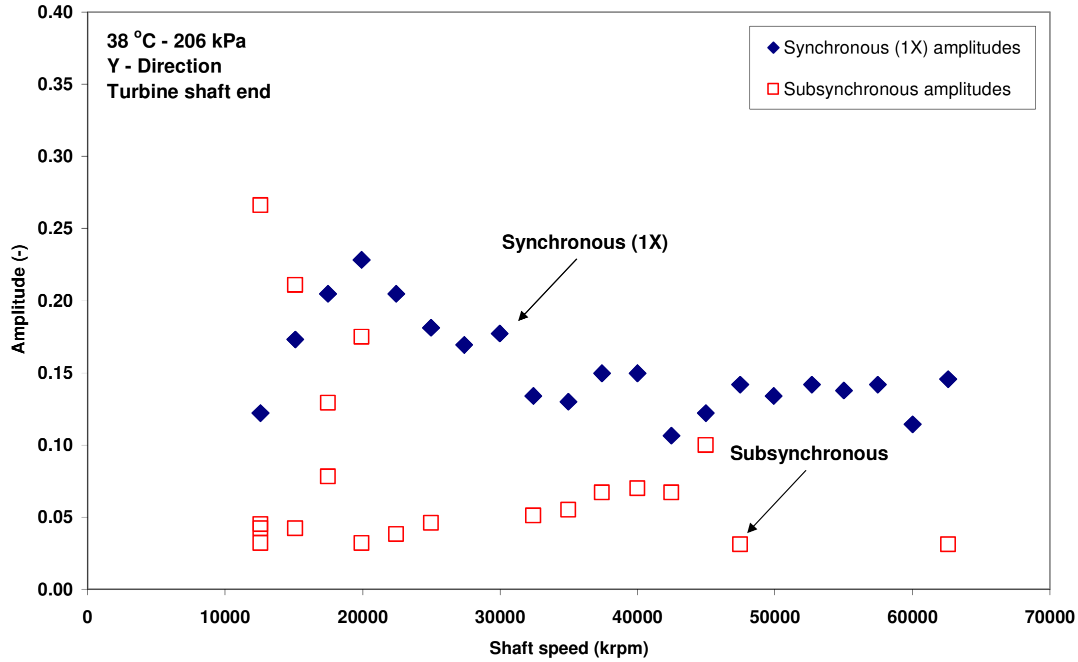

Figure 28 Synchronous and subsynchronous motions at compressor (top) and turbine (bottom) shaft ends (Y-direction). Lubricant inlet temperature 38 °C and feed pressure of 206 kPa [19]

Figure 29 depicts the measured dimensionless horizontal (*X*) synchronous and subsynchronous amplitudes of shaft motions versus whirl frequency ratios (*WFRs*) at the compressor (top) and turbine (bottom) ends of the TC rotor. Figure 30 shows the vibration amplitudes and *WFRs* for the vertical direction (*Y*). In the analysis, the whirl frequency ratio (*WFR*) is the ratio of a subsynchronous frequency to the frequency of shaft rotation. In the graphs, a large concentration of data points indicates the importance of a particular frequency. The synchronous (*1X*) motions with *WFRs* equal 1 are dominant in both *X* and *Y* directions. Concentration of data points are observed for *WFRs* ranging from 50% to 60% and 12% to 20% of shaft speed. Accordingly, subsynchronous vibrations are concentrated at frequencies below 300 Hz. Note that the largest subsynchronous amplitudes correspond to the higher *WFRs* (0.5-0.6). These large vibrations reach amplitudes of approximately 30% of the physical limit in the vertical direction (*Y*) at the compressor end. The subsynchronous motions concentrated at the lower whirl frequency ratio reach maximum amplitudes of approximately 10% of the physical limit.

A complete discussion of specific trends encountered in the measured *WFRs* is given at the end of this chapter.

Figure 31 shows the dimensionless amplitude of *X*-direction synchronous (*1X*) response to imbalance (0-pk) measured at the compressor and turbine ends of the TC. The results are for a nominal lubricant inlet temperature of 38 ^{o}C and varying feed pressures ranging from 158 kPa to 272 kPa. The synchronous (*1X*) vibrations show a slight increase in amplitude with increasing lubricant feed pressure, in particular at the compressor end. Peak amplitudes appear at approximately 20 krpm for both the compressor and turbine ends; evidencing the existence of a critical speed. Observe that at high shaft speeds, the largest synchronous (*1X*) amplitudes appear at the turbine end. A second peak appears in the turbine synchronous response at approximately 48 krpm, although this peak is not evident in the measured response at the compressor end of the rotor. This large synchronous vibration could indicate the existence of a second critical speed within the measured speed range.

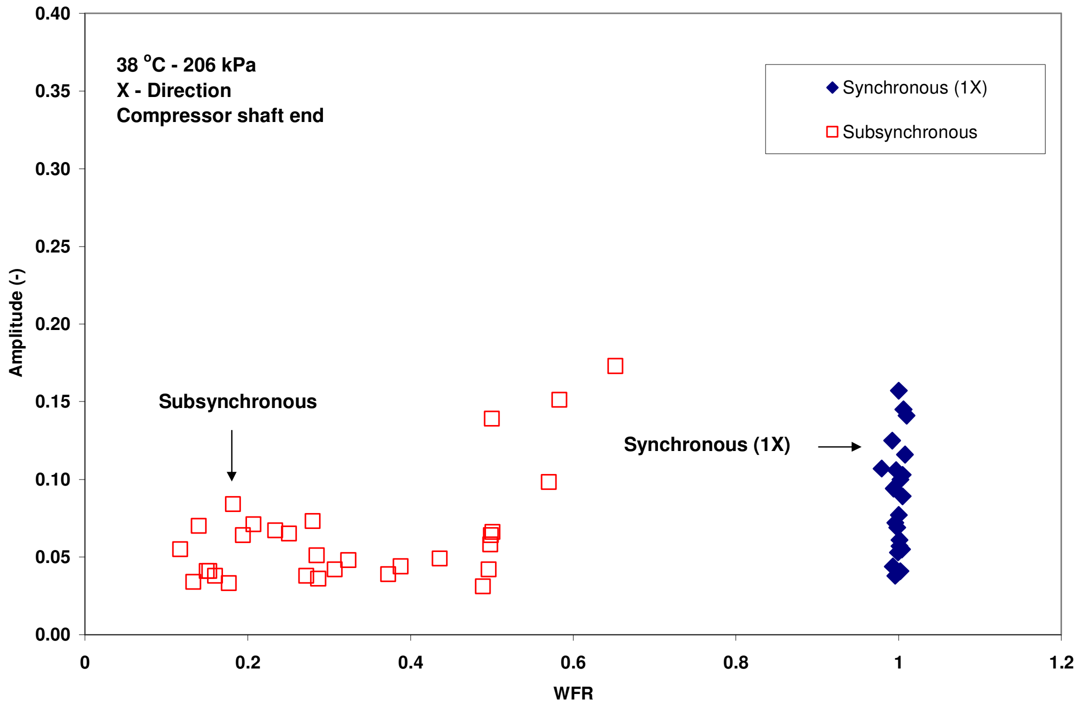

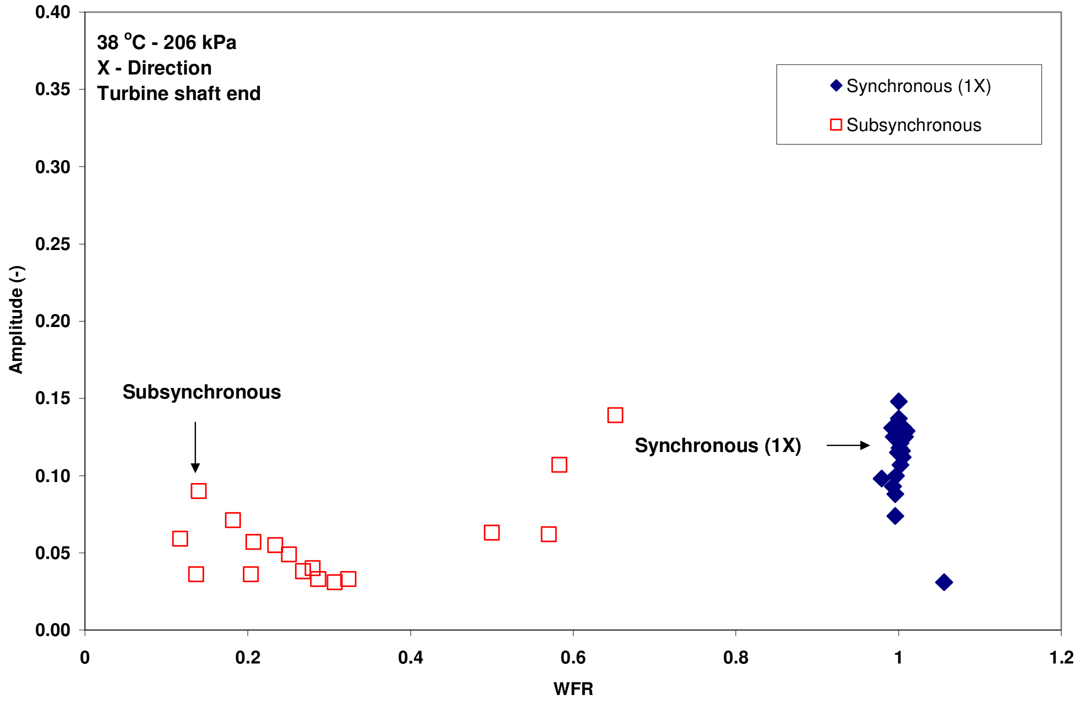

Figure 29 Amplitudes of synchronous and subsynchronous motions versus *WFRs* at compressor (top) and turbine (bottom) shaft ends (X – direction). Lubricant inlet temperature 38 °C and feed pressure of 206 kPa [19]

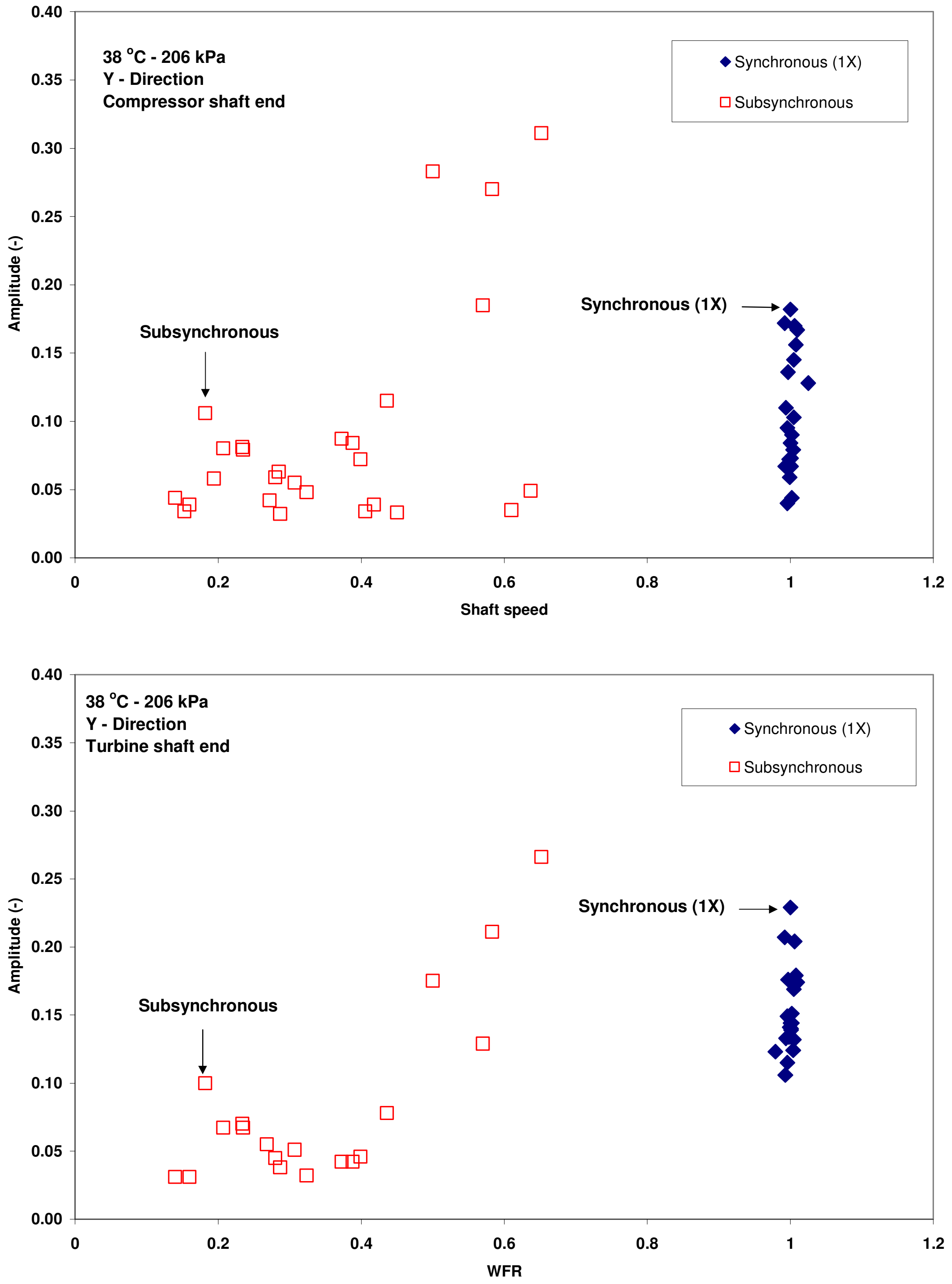

Figure 30 Amplitudes of synchronous and subsynchronous motions versus *WFRs* at compressor (top) and turbine (bottom) shaft ends (Y – direction). Lubricant inlet temperature 38 ^{o}C and feed pressure of 206 kPa [19]

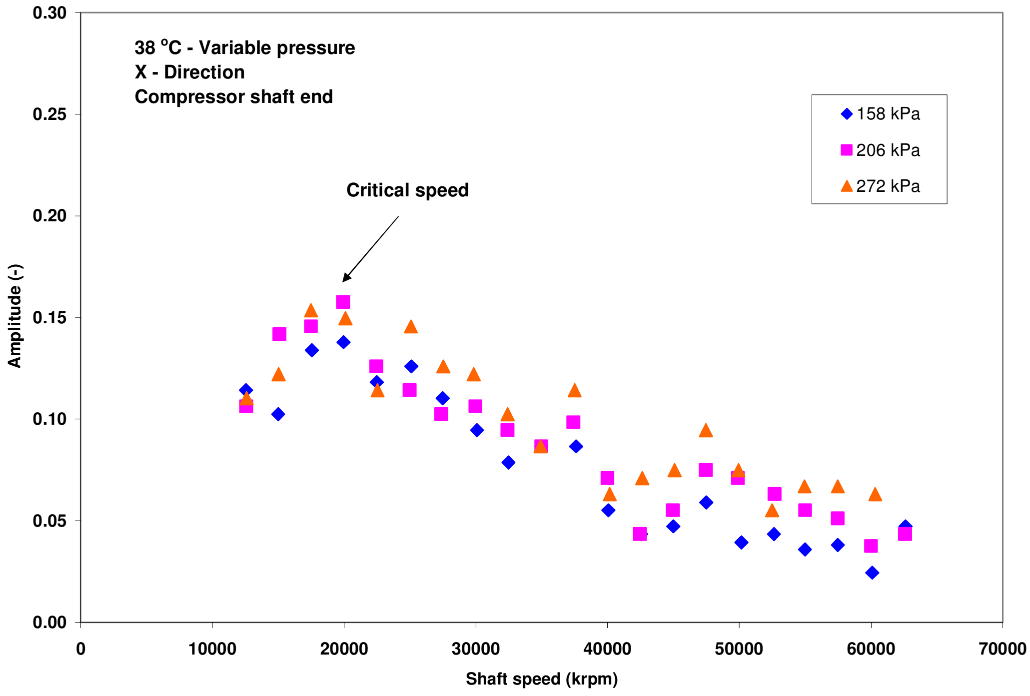

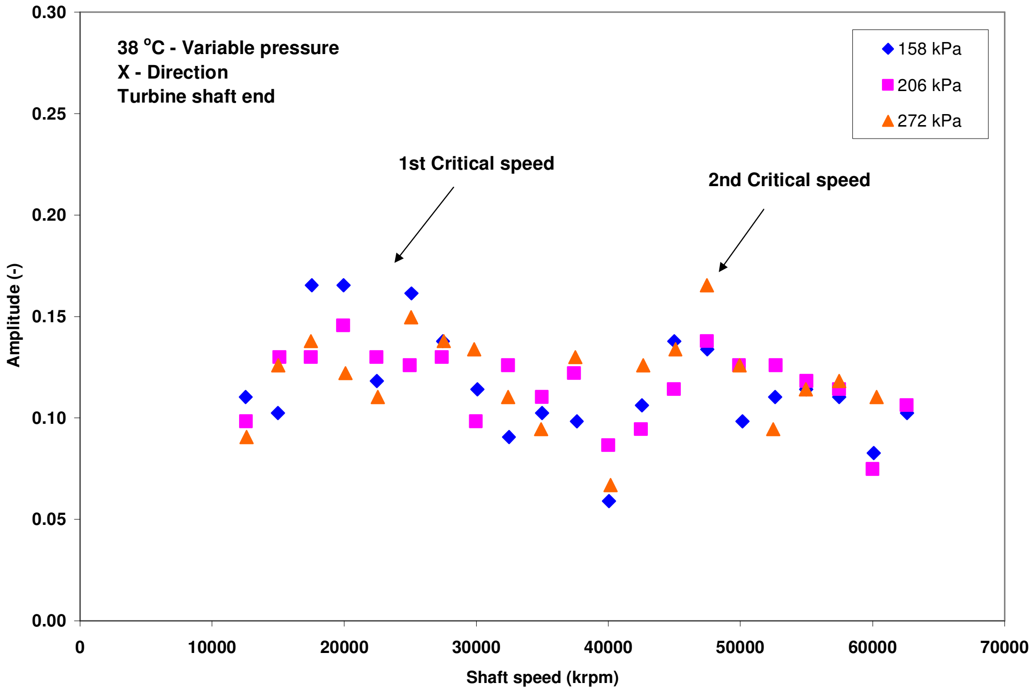

Figure 31 ***X*-direction measured amplitudes of synchronous shaft motion versus shaft speed; (top) compressor end (bottom) turbine end. Variable lubricant feed pressure, 38 °C supply temperature [19]**

Figure 32 depicts the *Y*-direction synchronous (*1X*) response to imbalance (0-pk) at the compressor and turbine shaft ends. The results correspond to the same operating conditions as for the results presented in Figure 31**.** The peak amplitudes at approximately 20 krpm for both TC ends show a critical speed, agreeing with the results depicted in Figure 31**.** The second peak presumed to be related to a second critical speed is clear for the turbine response in the horizontal (*X*) direction at approximately 48 krpm, although it is indistinguishable in the vertical (*Y*) direction response. Note that the largest synchronous amplitudes are measured in the direction of the gravitational load (*Y*-direction*)*, in particular for the turbine shaft end (heavy end). In addition, results in Figure 31 and Figure 32 demonstrate that the rotor *1X* response does not depend significantly on the lubricant feed pressure.

It is also important to determine whether the synchronous response depends or not on the lubricant inlet temperature. Figure 33 and Figure 34 depict the *X* and *Y* motion synchronous (*1X*) amplitudes, respectively, for 206 kPa lubricant feed pressure and variable inlet temperatures ranging from 32 ^{o}C to 46 ^{o}C.

The experimental results show that increasing the lubricant inlet temperature decreases slightly the *1X* motion amplitudes. This behavior is more evident at the compressor end of the TC rotor. As expected from the previous results, the peak amplitudes (*X* and *Y* directions) occur at approximately 20 krpm for both compressor and turbine shaft ends. A second peak is evident at approximately 45 krpm with larger amplitude at the turbine end of the TC rotor, perhaps indicating the existence of a second critical speed.

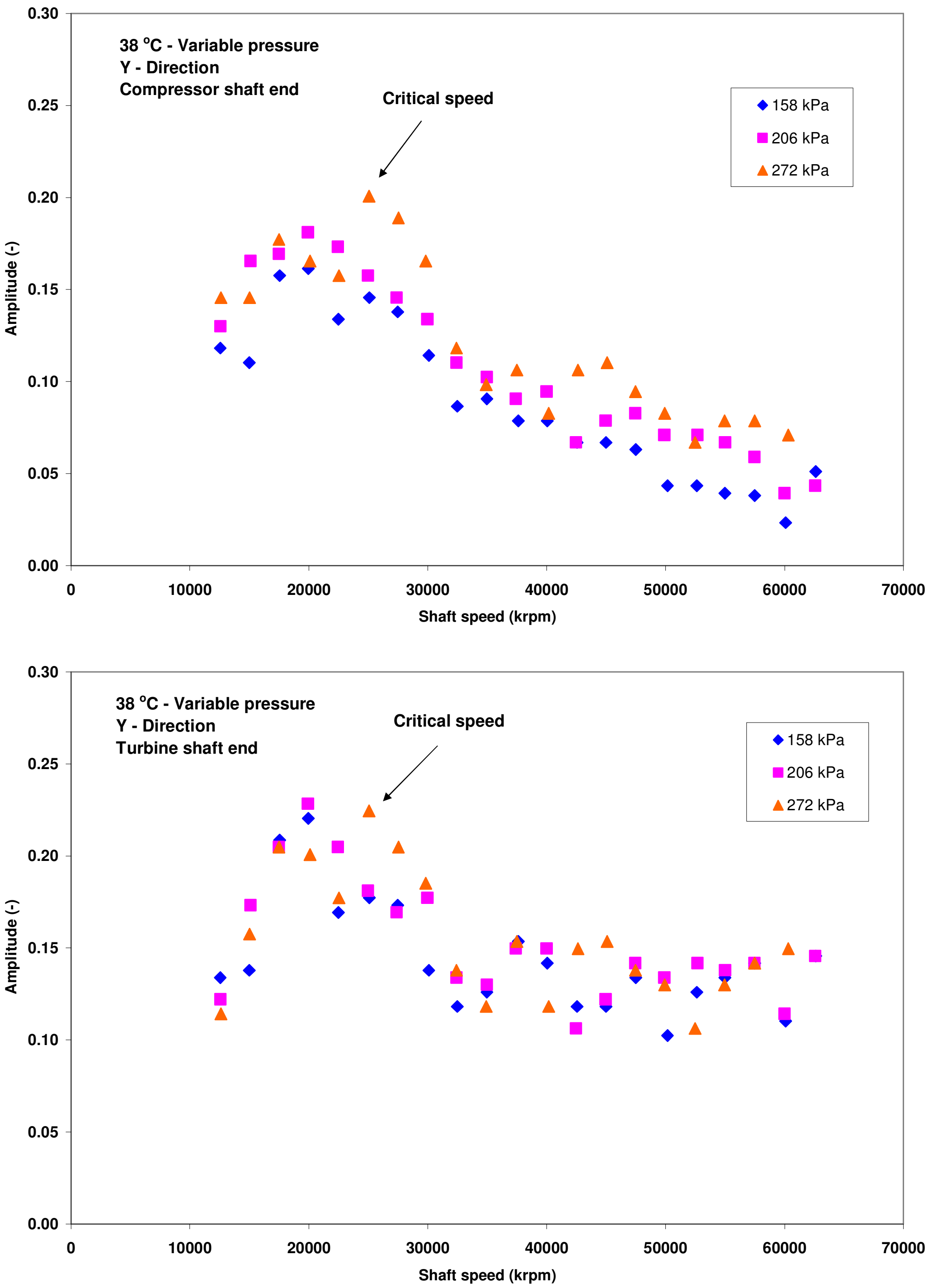

Figure 32 ***Y*****-direction measured amplitudes of synchronous shaft motion versus shaft speed; (top) compressor end (bottom) turbine end. Variable lubricant feed pressure, 38 °C supply temperature [19]**

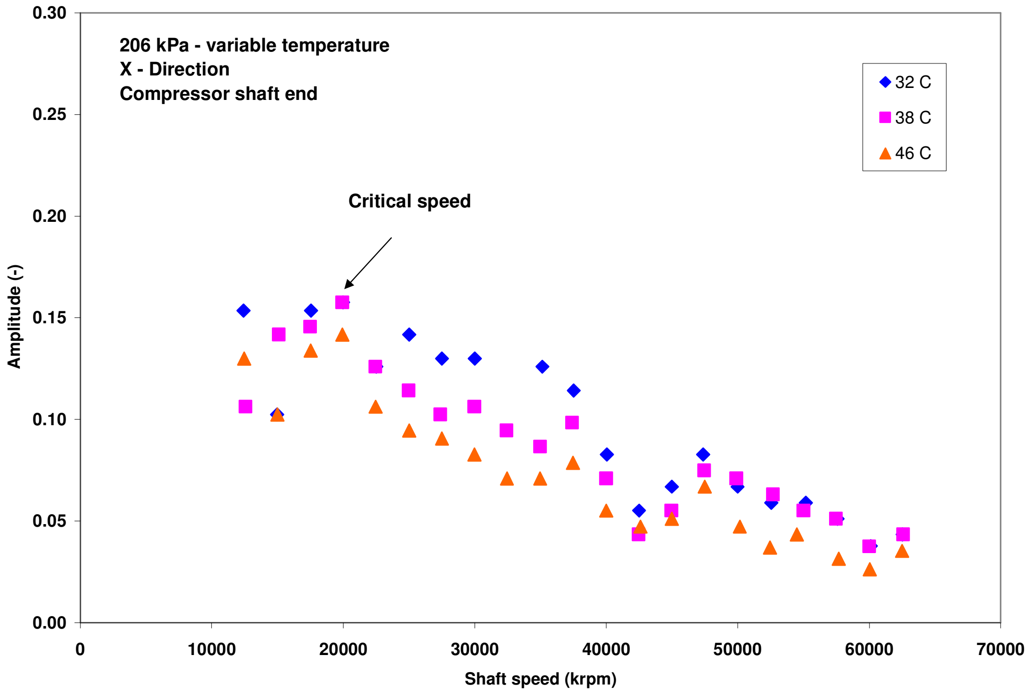

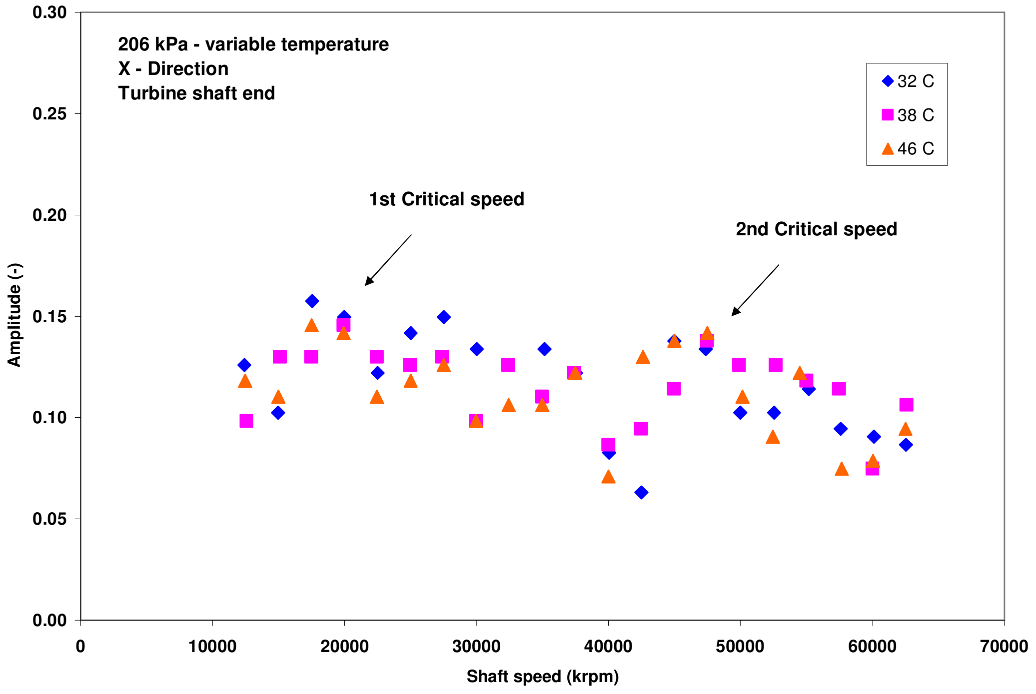

Figure 33 ***X*-direction measured amplitudes of synchronous shaft motion versus shaft speed; (top) compressor end (bottom) turbine end. 206 kPa lubricant feed pressure, variable inlet temperature [19]**

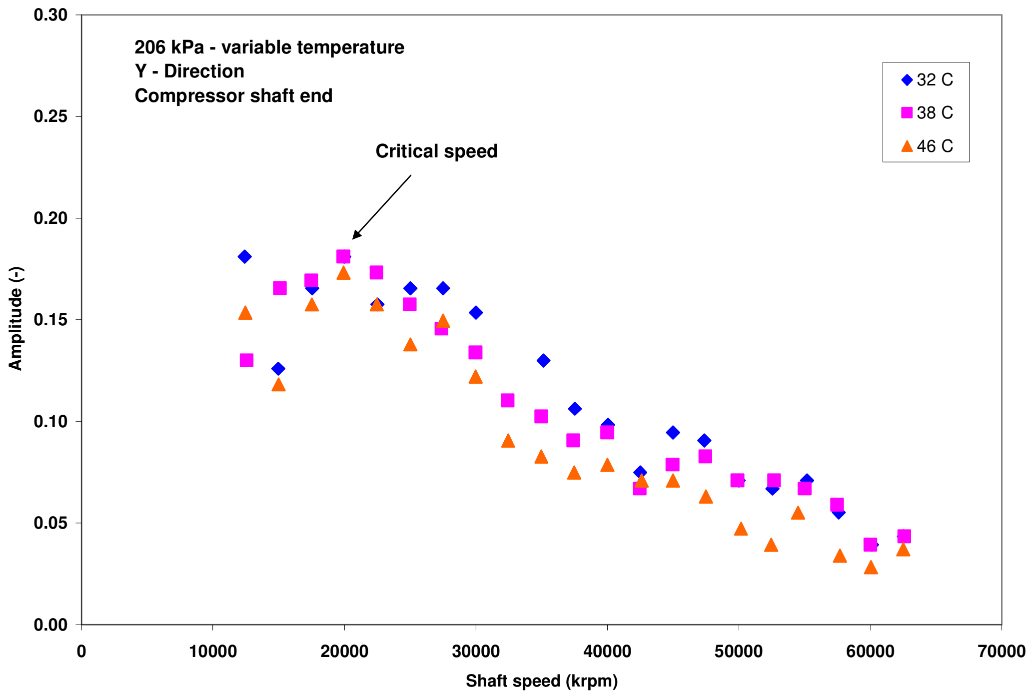

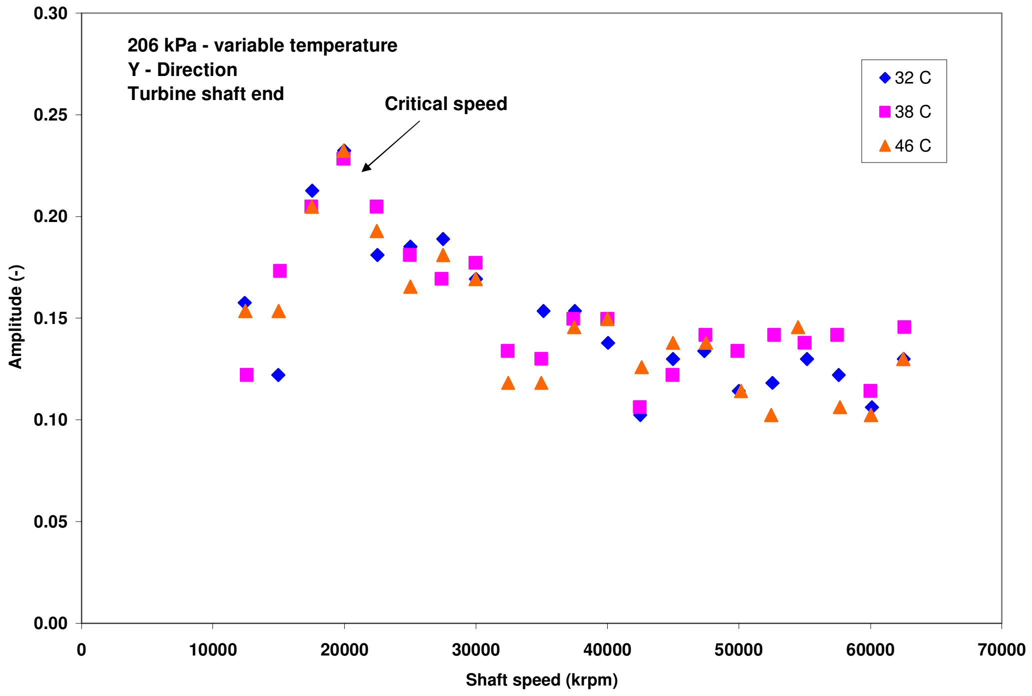

Figure 34 *Y*-direction measured amplitudes of synchronous shaft motion versus shaft speed; (top) compressor end (bottom) turbine end. 206 kPa lubricant feed pressure, variable inlet temperature [19]

Figure 35 and Figure 36 display the measured *X* and *Y* components of subsynchronous motions versus shaft speed, respectively. The results are for a nominal oil inlet temperature of 38 ^{o}C and variable supply pressure. The top and bottom graphs correspond to the compressor and turbine shaft end motions, respectively. The shaft motion in the *X* and *Y* directions are similar for the compressor and turbine shaft ends, although note that at low shaft speeds (< 20 krpm) the largest amplitudes of subsynchronous motions are measured at the compressor end of the rotor. The subsynchronous amplitudes remain nearly invariant for shaft speeds ranging from 20 krpm to 40 krpm. The test data shows large amplitude subsynchronous vibrations at a higher shaft speed, reaching peak amplitudes at approximately 47 krpm. The measured subsynchronous amplitudes are similar along both the *X* and *Y* directions. Thus, any further discussion on the amplitudes of subsynchronous vibrations will be related to the horizontal component (*X*- direction) only.

Figure 37 depict the subsynchronous amplitudes measured at the compressor and turbine ends of the TC rotor versus whirl frequency ratio (*WFR*) for a nominal lubricant inlet temperature of 38 ^{o}C and feed pressures ranging from 158 kPa to 272 kPa. The top and bottom graphs correspond to the compressor and turbine shaft end motions, respectively. The largest subsynchronous amplitudes concentrate in *WFRs* ranging from 0.5 to 0.6, corresponding to shaft speeds between 12 krpm and 20 krpm. A second peak with large subsynchronous amplitudes is evident for *WFRs* of approximately 0.2, corresponding to a shaft speed of 47 krpm.

The analysis of the subsynchronous motions indicate that the subsynchronous amplitudes are not affected by changes in the lubricant feed pressure or temperature. Two main subsynchronous vibrations are evident at approximately 12%-20% and 50%-60% of the rotor speed with the largest amplitudes corresponding to the higher frequency vibration.

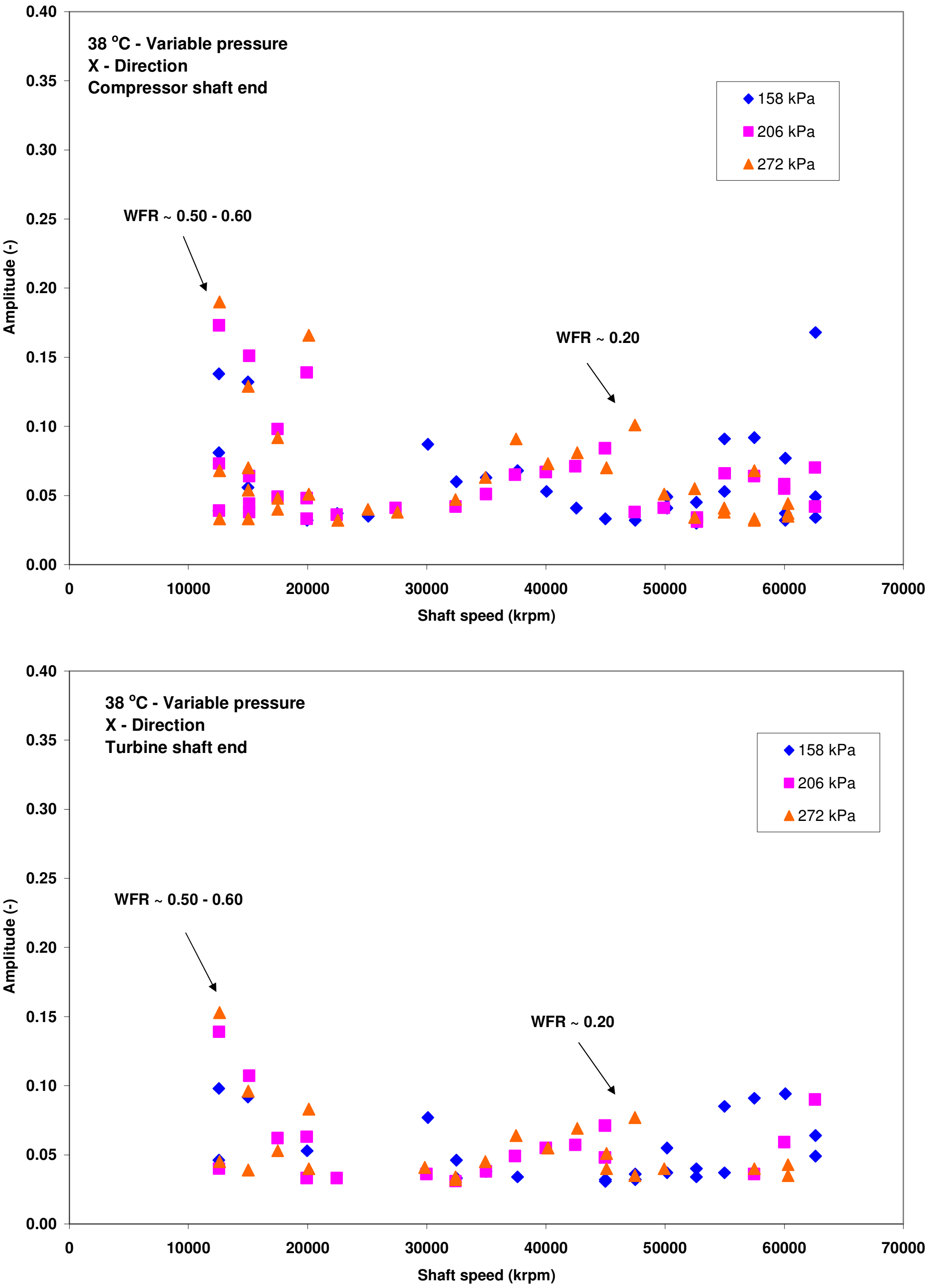

Figure 35 *X*-direction measured amplitudes of subsynchronous shaft motion versus shaft speed; (top) compressor end (bottom) turbine end. Variable lubricant feed pressure, 38 ^{o}C inlet temperature [19]

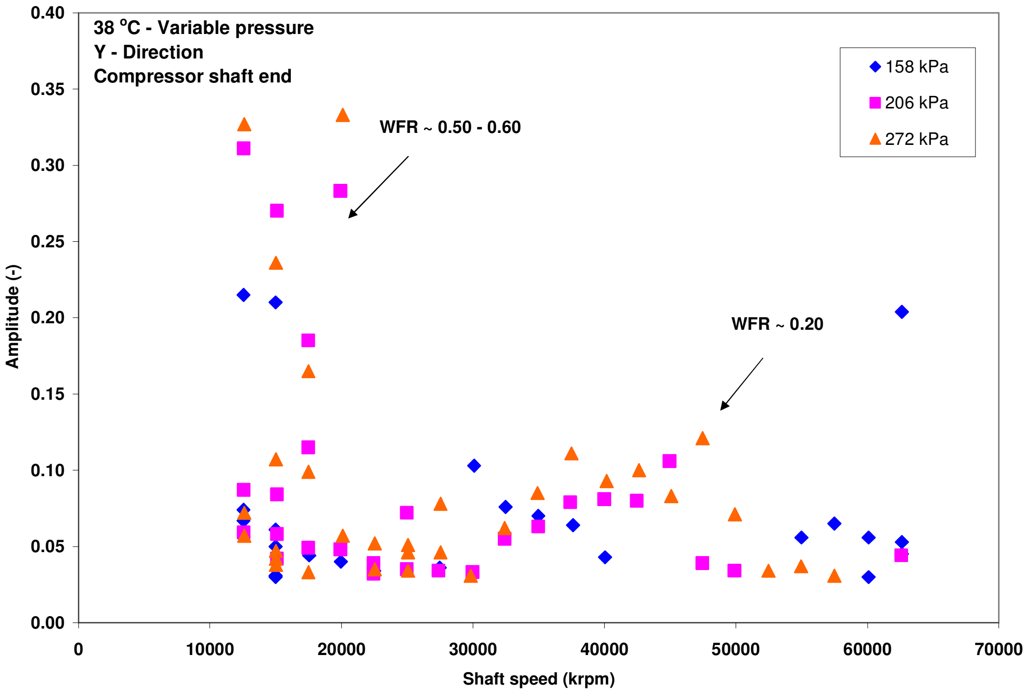

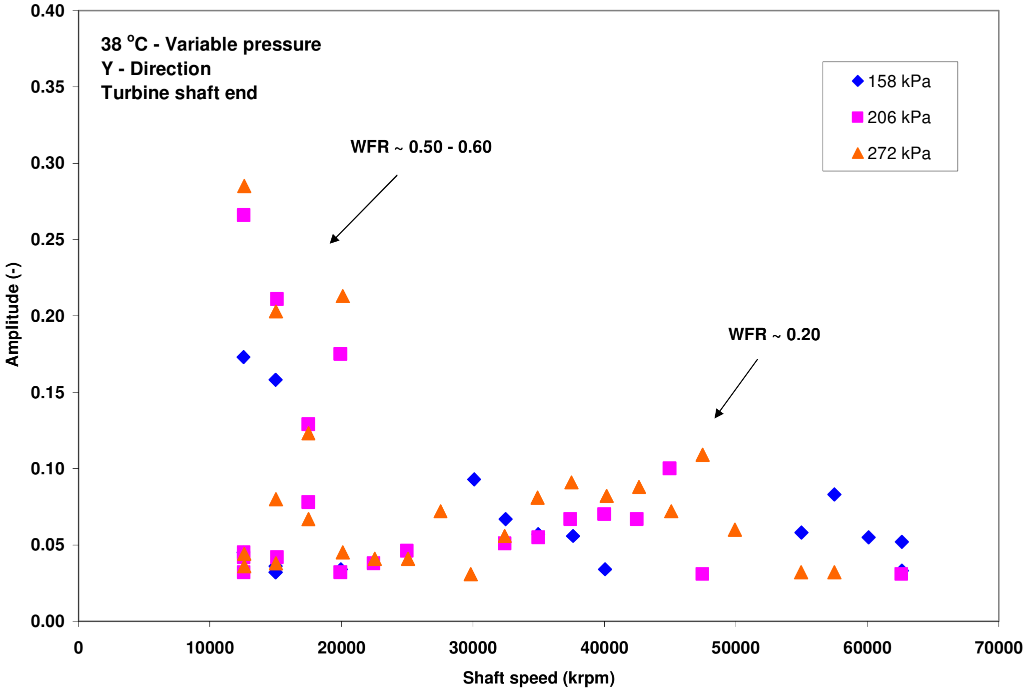

Figure 36 *Y*-direction measured amplitudes of <u>subsynchronous</u> shaft motion versus shaft speed; (top) compressor end (bottom) turbine end. Variable lubricant feed pressure, 38 ^{o}C inlet temperature [19]

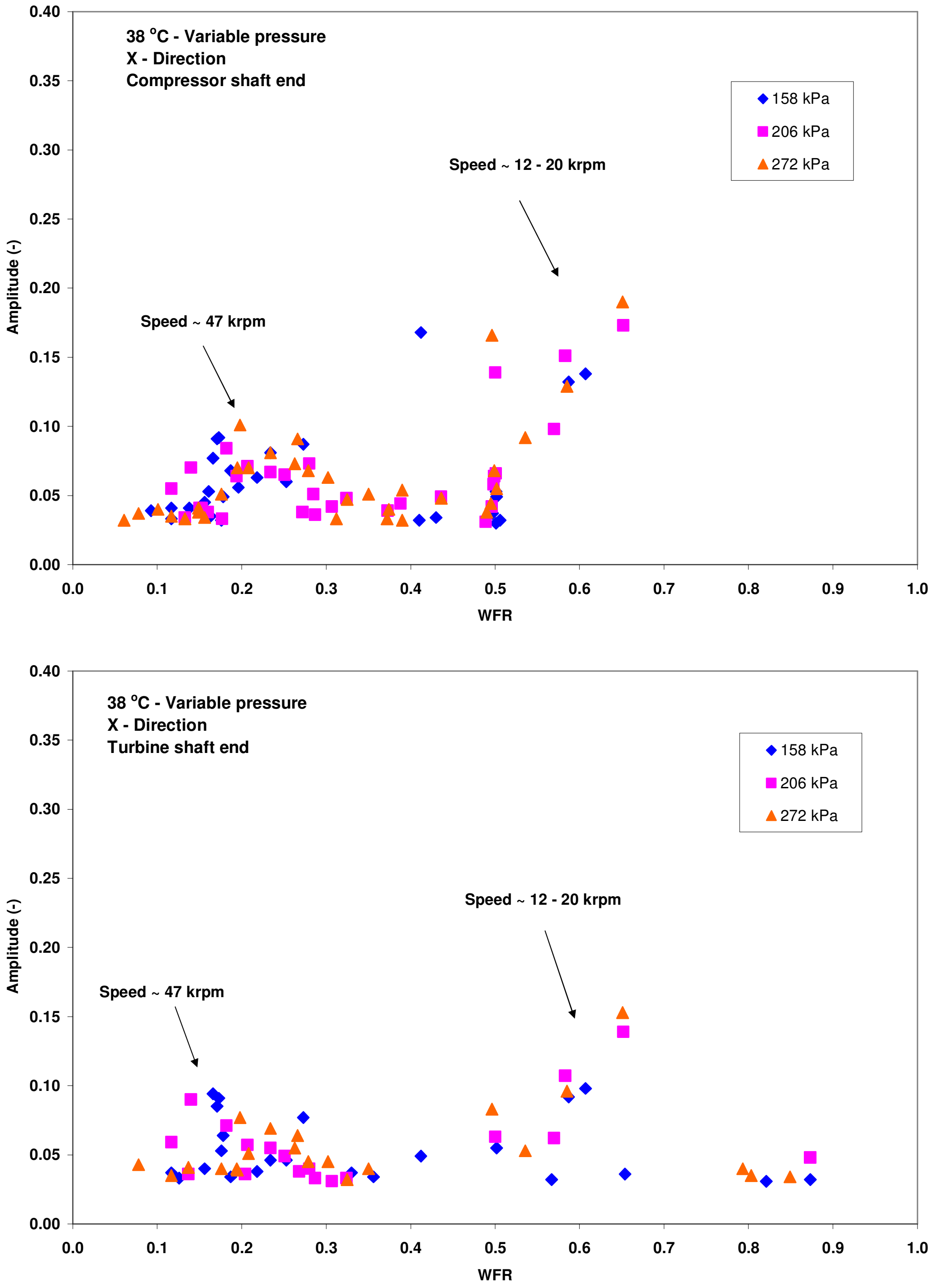

Figure 37 *X*-direction measured amplitudes of subsynchronous shaft motion versus whirl frequency ratio (*WFR*); (top) compressor end (bottom) turbine end. Variable lubricant feed pressure, 38 °C inlet temperature [19]

Figure 38 and Figure 39 depict the *X* and *Y* direction subsynchronous whirl frequency ratios (*WFRs*) versus shaft speed, respectively. The results are for lubricant feed pressures ranging from 158 kPa to 206 kPa and nominal oil inlet temperature of 38 ^{o}C. The dashed line with square markers corresponds to 50% of the ring speed ratios, the solid lines with diamond markers corresponds to 50% of the ring plus shaft speed ratio and the solid lines with circular markers show the ring speed ratio, respectively. In the graphs, only ring speed ratios for lubricant feed pressure of 206 kPa and inlet temperature of 38 ^{o}C are shown since previous results indicate that ring speed ratios are not feed pressure dependant.

Note that at the compressor end of the TC rotor, one subsynchronous frequency at approximately 50%-60% the shaft speed tracks the line that denotes the 50% of the ring plus shaft speeds, in particular for the horizontal (*X*) motions. Thus, the largest amplitudes of subsynchronous shaft motions correspond to the instability of the inner film. Other subsynchronous shaft motion peaks are evident for *WFRs* of approximately 0.2, although with smaller amplitudes and more evident in the horizontal (*X*) direction. The two figures show subsynchronous frequencies that decrease steadily in amplitude as shaft speed increases. Two well defined whirl frequency ratios are evident in the two figures (Figure 38 and Figure 39). The first *WFR* starts at 60% of the shaft speed and decreases to values of approximately 13% at the highest tested shaft speed. The second *WFR* has a value of 0.3 at low shaft speed and decreases to below 0.1 at the highest shaft speed. These *WFRs* do not appear for all shaft speeds in the graphs due to the percentage of maximum amplitude selected as a threshold for the filtering process of the motion data. More importantly, the *WFR* that appears at approximately 50% of the shaft speed at the compressor end of the rotor indicates that the compressor side ring stopped rotating at high shaft speeds.

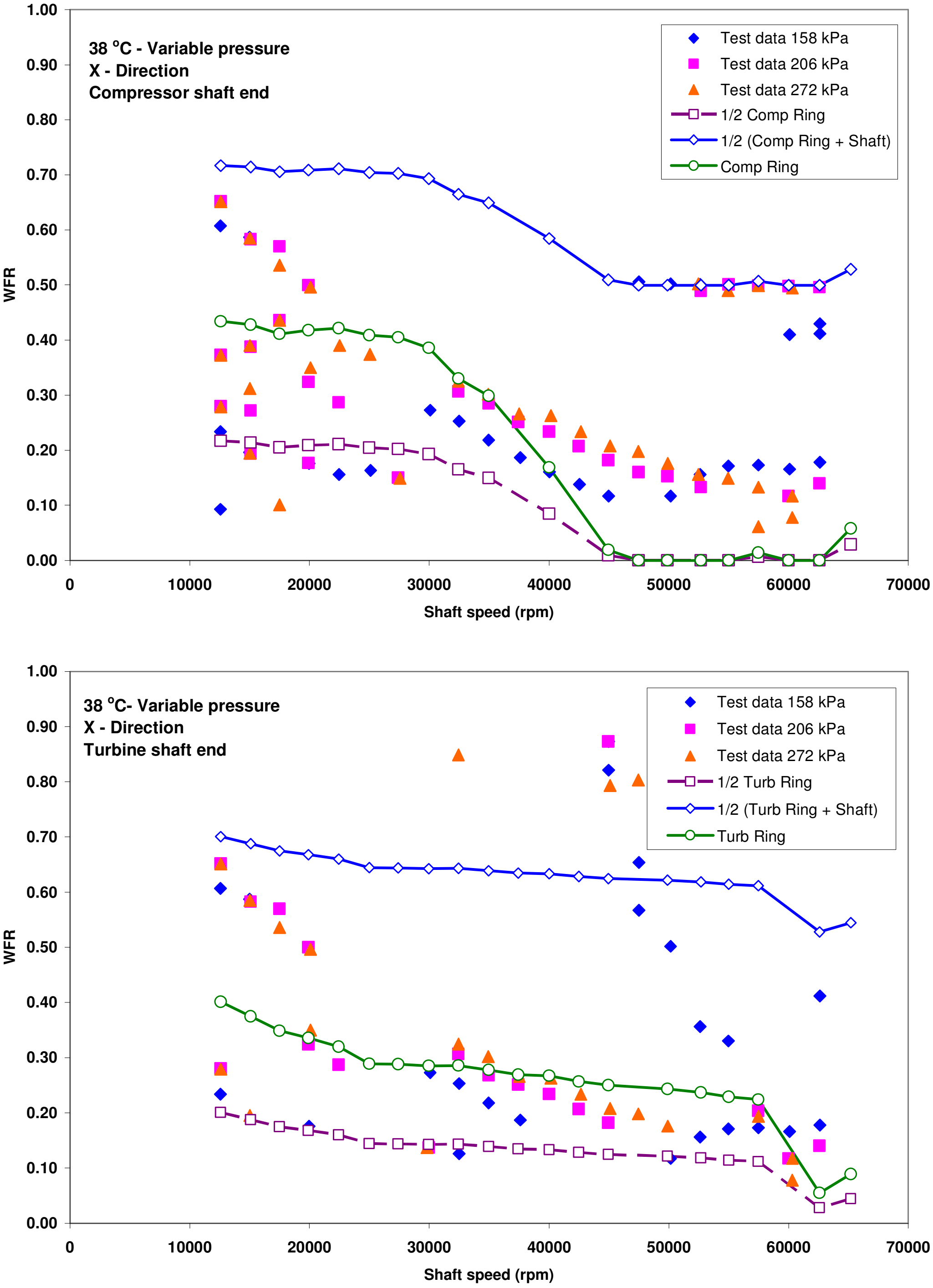

Figure 38 Turbine and compressor *X*-direction whirl frequency ratio versus shaft speed; (top) compressor end (bottom) turbine end. 206 kPa lubricant feed pressure, 38 °C inlet temperature [19]

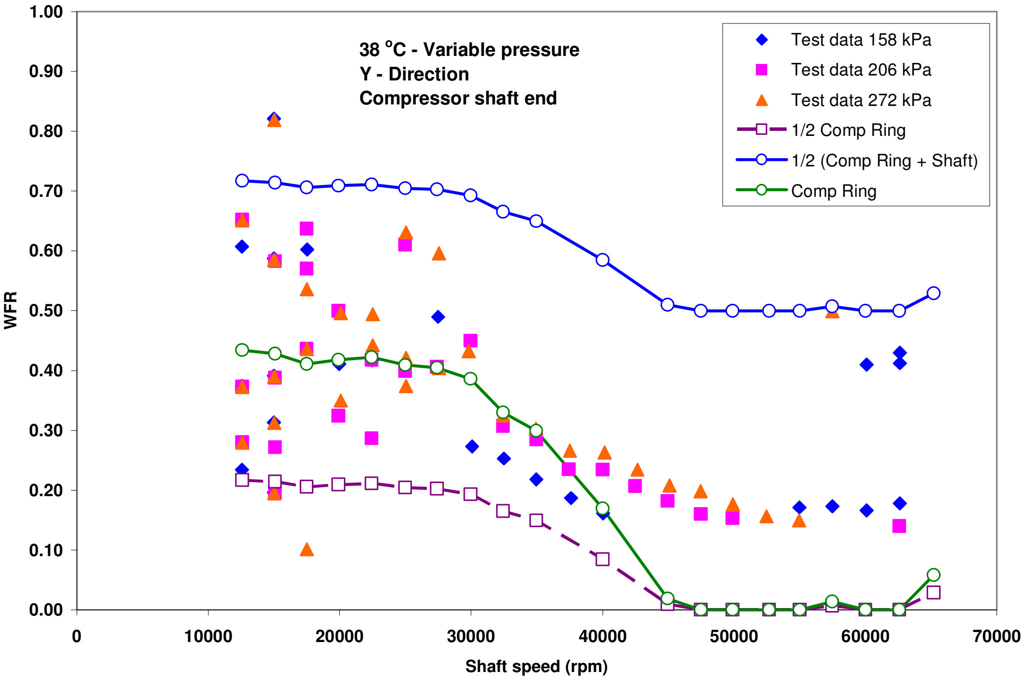

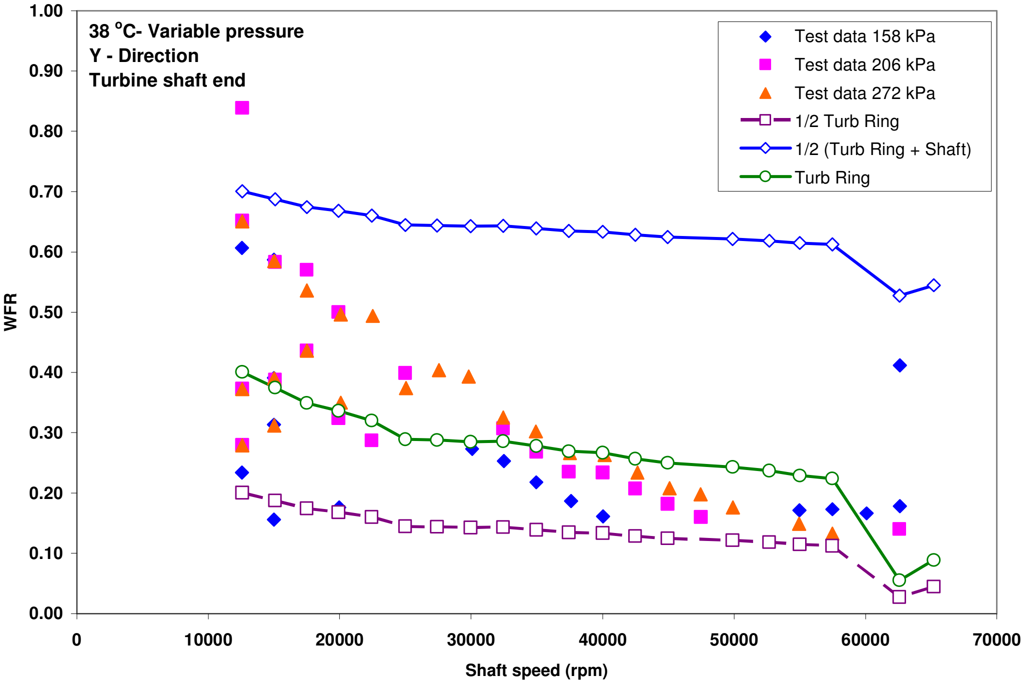

Figure 39 Turbine and compressor *Y*-direction whirl frequency ratio versus shaft speed; (top) compressor end (bottom) turbine end. 206 kPa lubricant feed pressure, 38 °C inlet temperature [19]

The test data shown is representative of the complex shaft motions encountered in turbocharger dynamics. The measurements show that the horizontal (*X*) and vertical (*Y*) motions are similar in amplitudes at both compressor and turbine ends. The synchronous (*1X*) motions are dominant in amplitude through the entire operating speed range when compared to the subsynchronous vibrations, except at the top speed (65 krpm) where a large amplitude subsynchronous vibration is evident in the test data. The measurements at the compressor and turbine ends of the TC rotor show a critical speed at approximately 20 krpm and steadily decreasing amplitudes at higher shaft speeds. Subsynchronous motions appear at frequencies below 300 Hz and are concentrated in two *WFRs*; the first one ranging from 12%-20% of the shaft speed and the second from 50%-60% of the shaft speed. The second WFR shows the largest amplitudes of subsynchronous vibrations. At high shaft speeds, above 50 krpm, the test data shows the existence of a *WFR* equal to 0.5, perhaps indicative that the floating rings stopped rotating.

Finally, comparisons of synchronous (*1X*) and subsynchronous motions for various operating conditions demonstrate that the shaft motions do not depend of the lubricant supply pressure and inlet temperature. However, the analyses indicate that using larger hydrostatic loads at high shaft speeds induce more subsynchronous activity in the nonlinear predictions, improving the correlation of predictions to test data.

CHAPTER V

PREDICTIONS OF LINEAR AND NONLINEAR RESPONSES FOR TURBOCHARGER. COMPARISONS TO TEST DATA

This chapter presents predictions of shaft motion forced response and comparisons to the test data advanced in [19]. As in the test data, shaft motion predictions are obtained at the compressor and turbine ends of the TC rotor. The rotor geometry and operating conditions are used with the TC linear and nonlinear rotordynamic models described in [11] for predictions of synchronous (*1X*) and subsynchronous shaft motions.

The linearized rotordynamic force coefficients (stiffness and damping) obtained from the FRB analysis are coupled to the linear rotordynamic model to perform a linear stability analysis (eigenvalue analysis) and obtain the damped natural frequencies and mode shapes of the system. In addition, the estimated imbalance is used along with the force coefficients to calculate the synchronous (*1X*) response to imbalance.

Finally, the FRB clearances and lubricant viscosities for the inner and outer lubricant films are the main input for the nonlinear time transient response analysis which yields the multiple subsynchronous frequencies and amplitudes for the specified operating conditions. Post processing of the results by means of mathematical software yields the synchronous (*1X*) and subsynchronous vibration components.

Linear eigenvalue analysis

The linear eigenvalue analysis relies on the specification of the stiffness and damping force coefficients for the inner and outer films at the turbine and compressor floating ring bearings. The linearized force coefficients are calculated with the fluid film bearing program previously described for a specified operating condition.

Table 5 shows the predicted TC critical speeds and damping ratios for lubricant feed pressures equal to 158, 206 and 272 kPa at a nominal inlet temperature of 38 ^{o}C. For a lubricant feed pressure equal to 158 kPa, the eigenvalue analysis predicts first, second and third critical speeds at 4, 20 and 70 krpm, respectively. Figure 40 depicts the rotor mode shape plots at the three critical speeds mentioned above. The first critical speed is associated to the excitation of the rotor conical mode, at frequencies ranging from 60 Hz to 90 Hz as shaft speed increases from 4 krpm to 70 krpm. The second critical speed is associated to the excitation of the rotor cylindrical-bending mode, showing larger motions at the compressor nose than at the turbine end of the TC rotor. The linear eigenvalue analysis predicts the cylindrical-bending mode with an almost constant frequency of approximately 330 Hz for all shaft speeds. Finally, the third predicted critical speed is related to the excitation of the first bending mode of the rotor. This last mode is predicted to occur with frequencies that increase with shaft speeds, starting at 900 Hz at the lowest shaft speed (4 krpm) and reaching approximately 1130 Hz at the highest shaft speed (70 krpm) .

Table 5 Critical speeds and damping ratios for TC rotor model. Lubricant inlet temperature of 38 ^oC and varying feed pressures

	Critical speed RPM	Frequency Hz	Damping Ratio	Mode shape
158 kPa	4000	60.3	-0.212	Conical mode
	20000	330.5	-0.021	Cylin-bending
	70000	1170.4	0.304	Bending
206 kPa	4000	64.7	-0.152	Conical mode
	20000	332.1	-0.022	Cylin-bending
	67500	1113.8	0.325	Bending
272 kPa	4000	69.5	-0.061	Conical mode
	20000	334.4	-0.02	Cylin-bending
	62500	1044.4	0.344	Bending

The predicted damping ratios and damped natural frequencies given in Table 5 show that the rotor conical and cylindrical-bending modes are unstable (damping ratio < 0) at the critical speeds. On the other hand, the first bending mode is predicted to be stable (damping ratio > 0). In addition, the rotor cylindrical-bending mode shows no dependence on the lubricant feed pressure. On the contrary, the rotor conical and first bending modes do show dependence to the lubricant feed pressure, in particular the conical mode.

Figure 41 shows the rotor damped natural frequency map for lubricant feed pressures of 158, 206 and 272 kPa for a nominal inlet temperature of 38 ^{o}C. Figure 42 depicts the stability map for the three lubricant feed pressures. As mentioned above, the rotor cylindrical-bending mode is predicted to occur at a constant frequency of approximately 330 Hz with negative damping ratios along the entire operating speed range (unstable mode). For the three lubricant feed pressures, the linear stability analysis predicts the rotor conical mode to be unstable (damping ratios < 0) from start up, becoming stable as shaft speed increases. Note that this mode shows significant dependence on the lubricant feed pressure, becoming stable at low shaft speeds as lubricant feed pressure increases. The rotor bending mode occurs for frequencies ranging from approximately 900 Hz to 1130 Hz, being always stable (damping ratios > 0). The cylindrical-bending mode is always unstable, irrespective of the lubricant feed pressure condition.

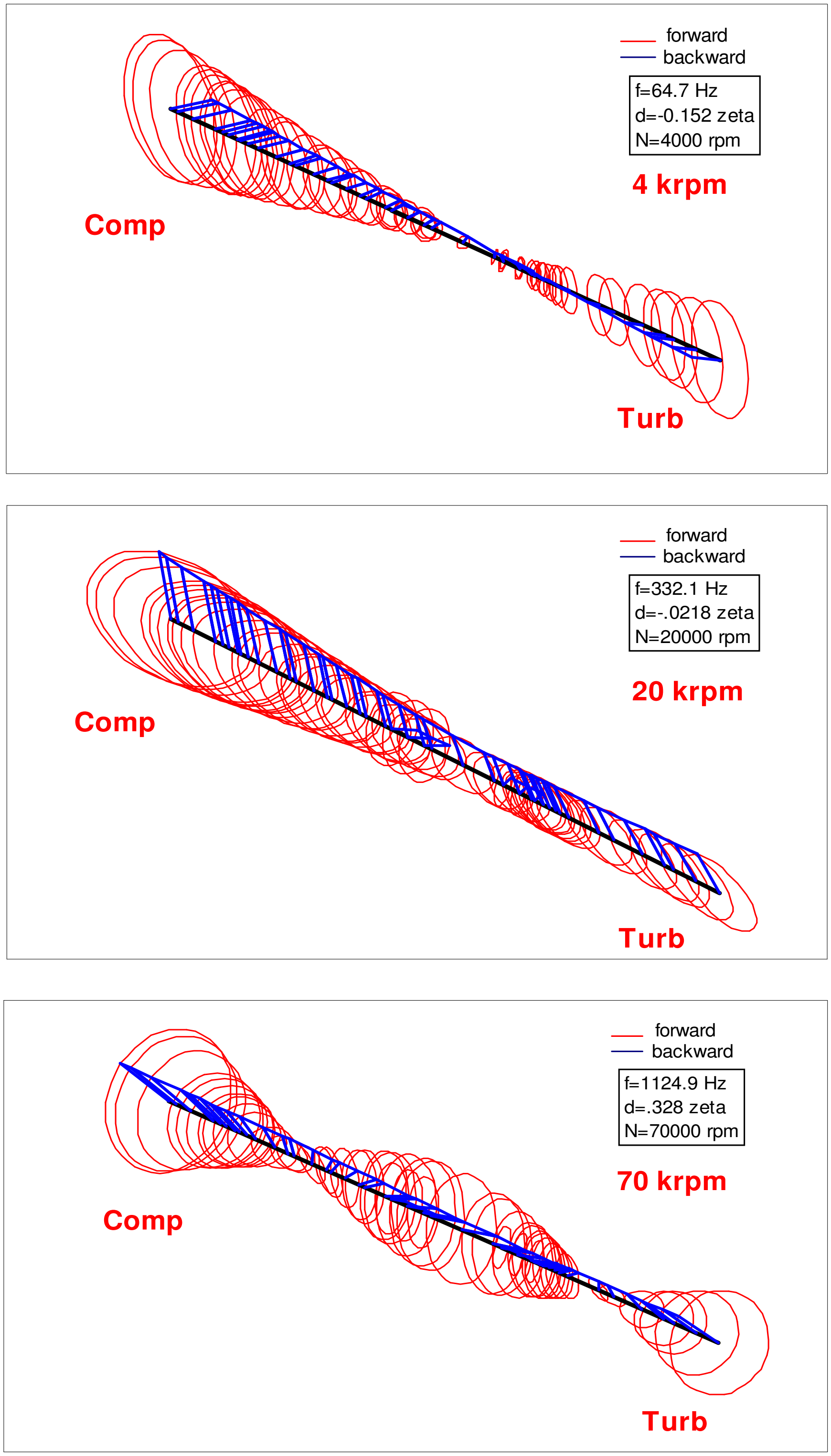

Figure 40 TC Rotor damped mode shape plots at critical speeds. Lubricant feed pressure of 206 kPa and inlet temperature of 38 ^{o}C

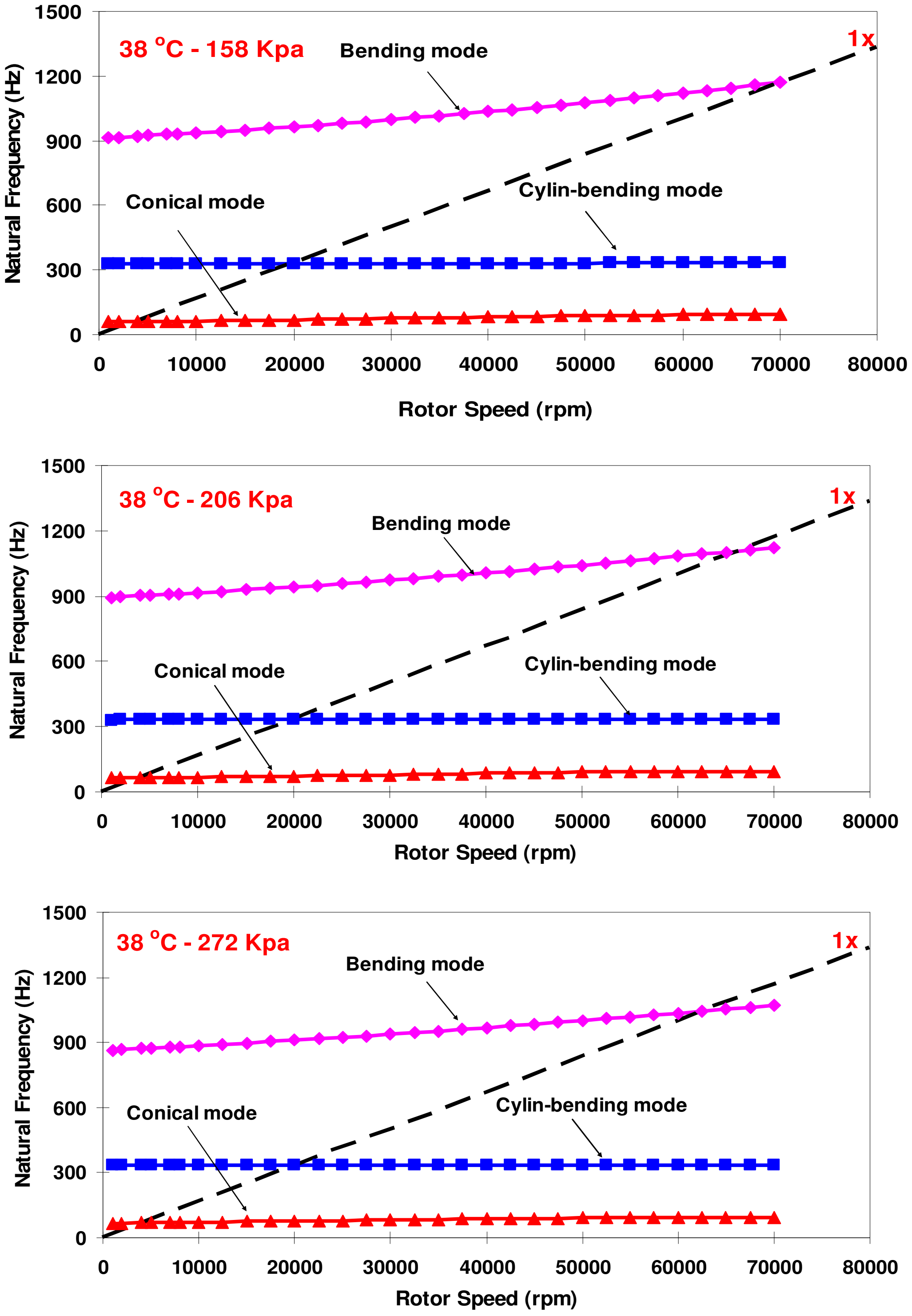

Figure 41 TC rotor natural frequencies versus shaft speed. Lubricant inlet temperature of 38 °C and varying feed pressures

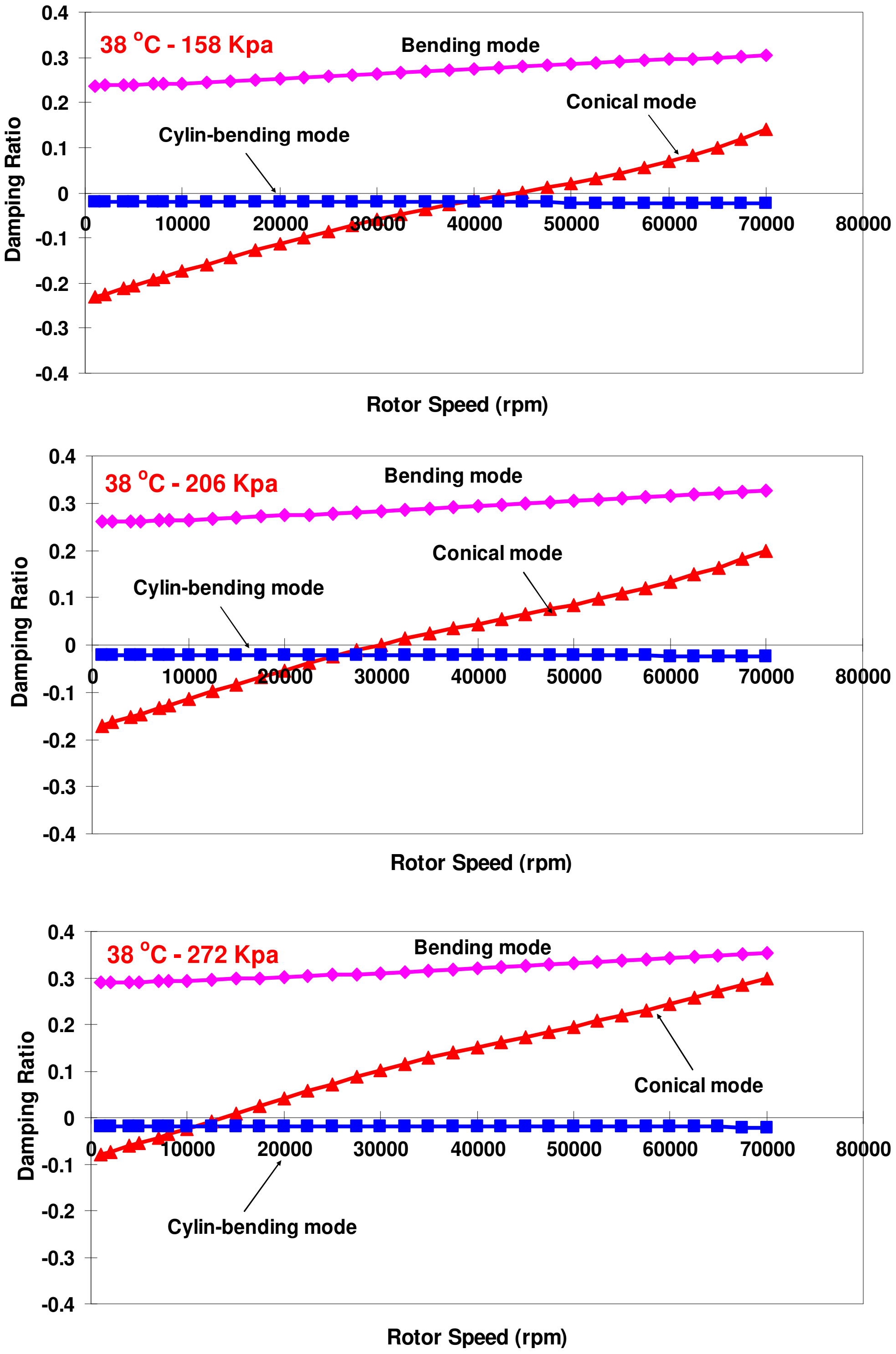

Figure 42 Damped eigenvalues (damping ratios). Lubricant inlet temperature of 38 °C and varying feed pressures

Imbalance response predictions

Table 2 (pg. 14) gives the imbalance masses used with the structural model for the synchronous (*1X*) response predictions. The estimated imbalance condition was obtained from test data at a lubricant feed conditions of 206 kPa in pressure and 38 ^{o}C, at shaft speeds equal to 60, 62.5 and 65 krpm. Chapter III describes the analytical procedure for estimating the imbalance masses and corresponding phase angles. The figures in this section show amplitudes of vibrations in dimensionless form relative to the limit of maximum conical motion at the turbine end of the TC rotor (0.254 mm 0-pk). Figure 43 shows the dimensionless amplitudes of TC synchronous response (compressor end) for 158, 206, and 272 kPa at a nominal lubricant inlet temperature of 38 ^{o}C. In the graphs, diamond markers show the test data, square-markers show the results from the nonlinear transient analysis and the solid line corresponds to the results from the linear analysis. Figure 44 displays test data and predictions corresponding to the turbine end of the rotor. A complete description of the nonlinear transient analysis follows later in this chapter.

The results from the linear analyses (compressor end) show good agreement with the test data, in particular at shaft speeds below 20 krpm and greater than 40 krpm, predicting well the first critical speed of the system. The test data for the three lubricant feed pressures show a steady reduction of the *1X* amplitudes as shaft speed increases. The linear result predictions show a sudden drop of synchronous amplitudes for shaft speeds ranging from 20 krpm to 30 krpm, underpredicting the measurements. As in the test data, the synchronous responses predicted with the linear model show a slight dependence on lubricant feed pressure; the major differences can be observed for the highest lubricant feed pressure case, namely 272 kPa.

The results obtained from the time response simulations (nonlinear analysis) underpredict the measured synchronous (*1X*) amplitudes from start up to approximately 45 krpm, showing good correlation to the test data at higher shaft speeds only. At the turbine end of the rotor, the linear and nonlinear *1X* predictions show good agreement with the test data for shaft speeds higher than 30 krpm. Nonetheless, both models predict lower imbalance response amplitudes than the test data at shaft speeds below 30 krpm, in particular the nonlinear model. The justification for the discrepancies between measured data and nonlinear predictions may be attributed to the uncertainty in the (used) imbalance masses and their exact location in the rotor model.

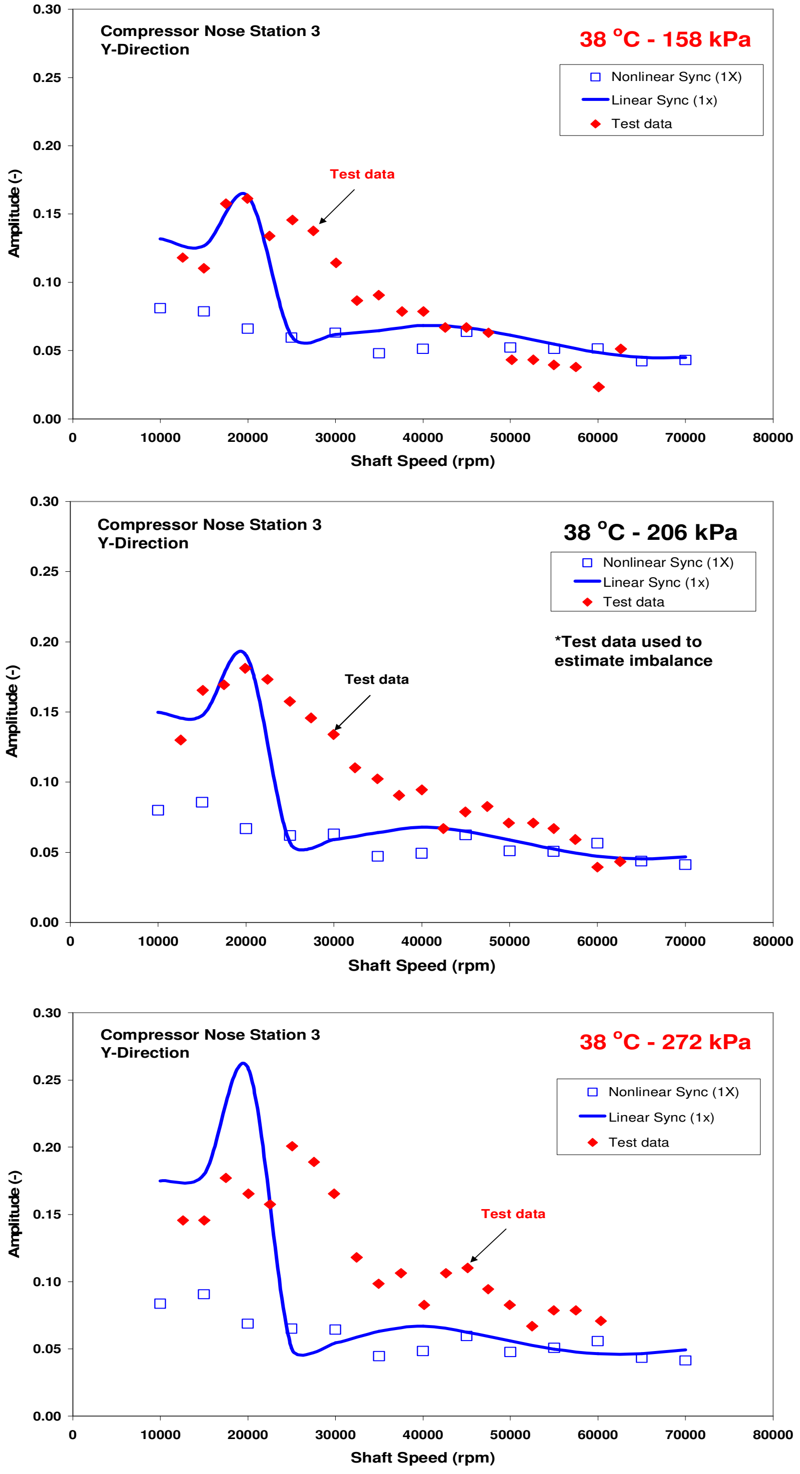

Figure 43 Compressor end synchronous response to imbalance. Lubricant supply pressure 158 kPa (Top), 206 kPa (Middle) and 272 kPa (Bottom). Nominal inlet temperature of 38 °C

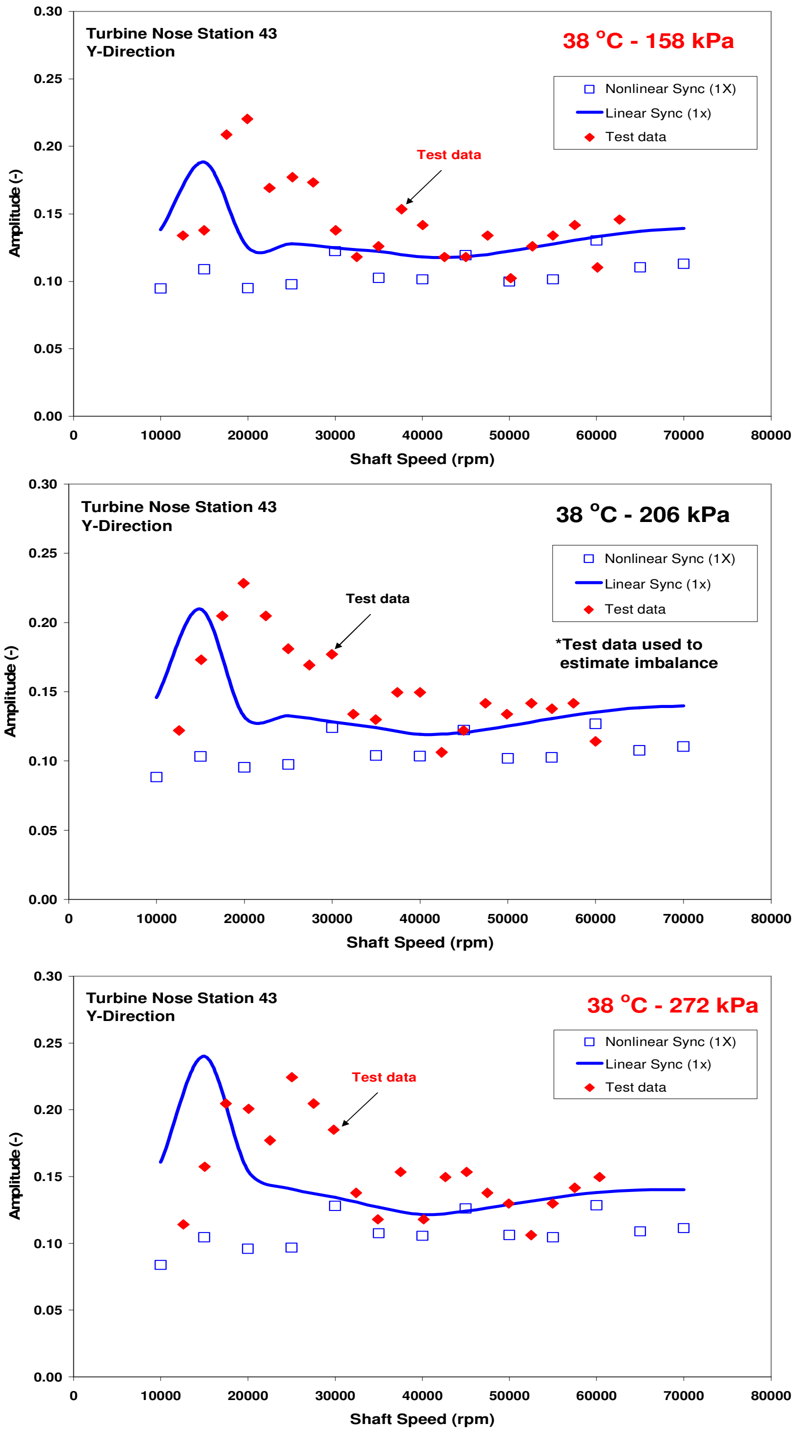

Figure 44 Turbine end synchronous response to imbalance. Lubricant supply pressure 158 kPa (Top), 206 kPa (Middle) and 272 kPa (Bottom). Nominal inlet temperature of 38 °C

Time response nonlinear predictions

Linear rotordynamic analyses are restricted to predict the synchronous (*1X*) response to imbalance, and not the amplitudes and multiple (subsynchronous) frequency components of shaft motion. Thus, it is necessary to conduct nonlinear rotordynamic analyses to reproduce the dynamics of the TC rotor/bearing system.

In the nonlinear transient analysis, the nonlinear equations of motion of the system (rotor-FRB) are integrated and the bearing reaction forces are calculated each time step of the numerical integration. The time transient nonlinear analysis was conducted for shaft speeds ranging from 10 krpm (166.7 Hz) to 70 krpm (1166.7 Hz) and lasting a sufficiently "long time" to warrant the prediction of a quasi steady-state motion condition. The results that follow in this section are obtained by using a total integration time of 1 sec and 12,800 time steps, resulting in a time step equal to 78 μs. The maximum frequency span is equal to 6,400 Hz with a minimum frequency step of 12.5 Hz (1024 data points). From the results, only the quasi steady-state portion is analyzed.

Shaft motion amplitudes are presented relative to the limit of maximum conical motion at the turbine end of the TC rotor (0.254 mm 0-pk). The predicted shaft motions include the effect of a hydrostatic load proportional to the lubricant feed pressure applied along the vertical direction of the FRB (refer to Figure 8). In the analysis, the proper fraction of rotor weight is used for each bearing, 1.41 N at the compressor side FRB and 4.25 N at the turbine side FRB; thus resulting in different operating inner and outer film clearances.

Table 6 and Table 7 show the static load predictions from the thermal floating ring bearing analysis for a lubricant feed pressure of 206 kPa and inlet temperature equal to 38 ^{o}C.

Table 6 Predicted ring speed, clearances and viscosities for compressor side FRB. Lubricant feed pressure 206 kPa, inlet temperature 38 ^{o}C

Rotor speed rpm	Ring speed rpm	Ring speed ratio	μ_i (Cpoise)	μ_o (Cpoise)	C_i (μm)	C_o (μm)
10000	3161	0.32	7.9	7.9	18.2	49.1
15000	4829	0.32	7.9	7.9	18.2	49.1
20000	6243	0.31	7.8	7.9	18.2	49.1
25000	7674	0.31	7.8	7.9	18.2	49.1
30000	9025	0.30	7.7	7.8	18.2	49.0
35000	10348	0.30	7.7	7.8	18.2	49.0
40000	11588	0.29	7.6	7.8	18.2	49.0
45000	12716	0.28	7.5	7.8	18.2	48.9
50000	13958	0.28	7.5	7.8	18.3	48.9
55000	14729	0.27	7.1	7.6	18.3	48.8
60000	15896	0.26	7.0	7.6	18.3	48.8
65000	16801	0.26	6.9	7.6	18.3	48.7
70000	17439	0.25	6.7	7.5	18.4	48.7
		Nominal:	7.9	7.9	17.5	47.5

μ_i: Inner film viscosity
μ_o: Outer film viscosity
C_i: Inner film clearance
C_o: Outer film clearance

ISO VG 10

Table 7 Predicted ring speed, clearances and viscosities for turbine side FRB. Lubricant feed pressure 206 kPa, inlet temperature 38 ^{o}C

Rotor speed rpm	Ring speed rpm	Ring speed ratio	μi (Cpoise)	μo (Cpoise)	Ci (μm)	Co (μm)
10000	2519	0.25	7.9	7.9	18.2	49.1
15000	3873	0.26	7.9	7.9	18.2	49.1
20000	5166	0.26	7.8	7.9	18.2	49.1
25000	6408	0.26	7.8	7.9	18.2	49.1
30000	7508	0.25	7.7	7.9	18.2	49.0
35000	8743	0.25	7.7	7.8	18.2	49.0
40000	9899	0.25	7.6	7.8	18.2	49.0
45000	10880	0.24	7.5	7.8	18.2	49.0
50000	11925	0.24	7.5	7.8	18.2	48.9
55000	12721	0.23	7.1	7.7	18.3	48.8
60000	13585	0.23	7.0	7.7	18.3	48.8
65000	14411	0.22	6.9	7.6	18.3	48.7
70000	15438	0.22	6.7	7.6	18.3	48.7
		Nominal:	7.9	7.9	17.8	48.5

μ_i: Inner film viscosity
μ_o: Outer film viscosity
C_i: Inner film clearance
C_o: Outer film clearance

ISO VG 10

Figure 45 portrays predicted horizontal (*X*) displacement waterfall plots that correspond to the compressor (top graph) and turbine (bottom graph) ends of the TC rotor, respectively. Similarly, Figure 46 shows the vertical (*Y*) displacement waterfalls for the compressor (top) and turbine (bottom) rotor ends. Figure 23 and Figure 24 (pg. 38-39) show the test data for similar operating conditions.

Clearly, the predicted (nonlinear) synchronous (*1X*) amplitudes at the turbine shaft end are larger than at the compressor end of the rotor, agreeing well with the test data. One main subsynchronous whirl frequency (instability) is evident at both ends of the TC. Post processing of the predicted data indicates that the subsynchronous motions tracks the synchronous motion at approximately 50%-60% of the shaft speed. The nonlinear analysis predicts subsynchronous motions for shaft speeds ranging from 10 krpm to 55 krpm. The test data on the other hand, shows subsynchronous vibrations along the entire operating speed range (10 krpm to 70 krpm).

Figure 47 depicts transmitted loads predicted for the horizontal and vertical directions of the compressor side FRB. Transmitted dynamic loads to the TC casing are larger in the horizontal direction and not in the direction of the applied hydrostatic load (*Y*-direction). The waterfalls of transmitted force show large synchronous force components that increase in magnitude with shaft speed, reaching load magnitudes up to approximately 20 N (0-pk) at the highest shaft speed (70 krpm). Figure 48 depicts the transmitted dynamic loads to the TC casing at the turbine side FRB. The graph shows large synchronous loads that increase in magnitude with shaft speed, reaching similar peak loads as for the compressor side FRB. Although, note that at the turbine side FRB the largest dynamic loads are predicted in the direction of the hydrostatic side load. In addition, the nonlinear transient analysis predicts unexpected large 2X load components that increase in magnitude with increasing shaft speed.

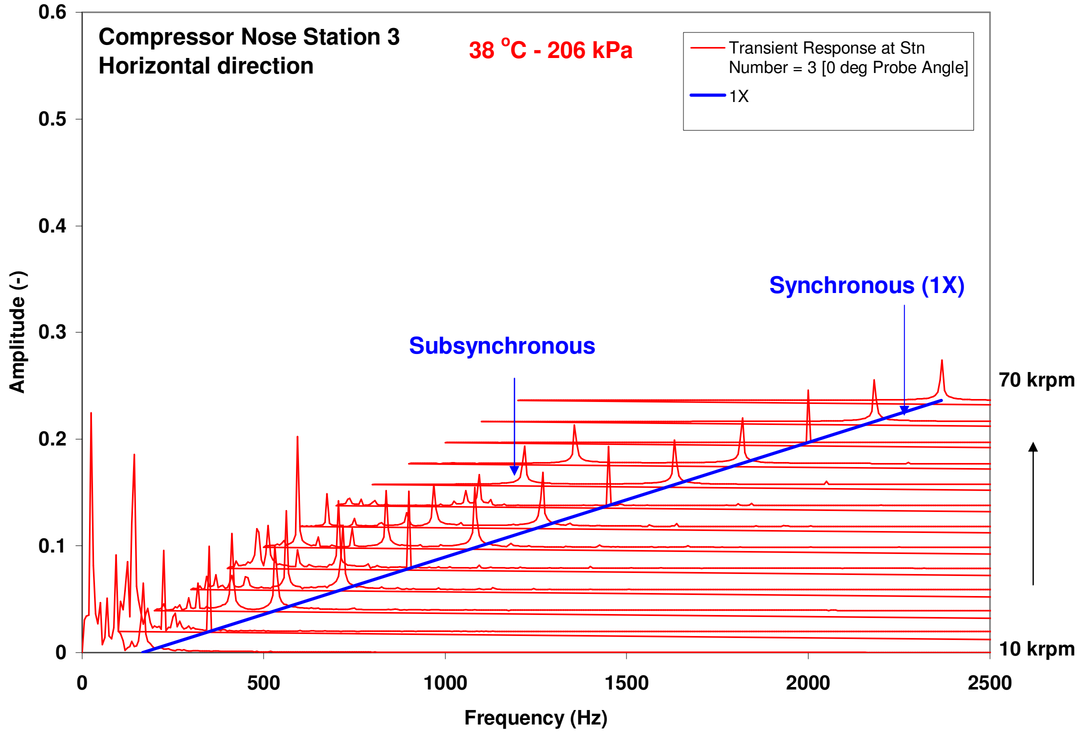

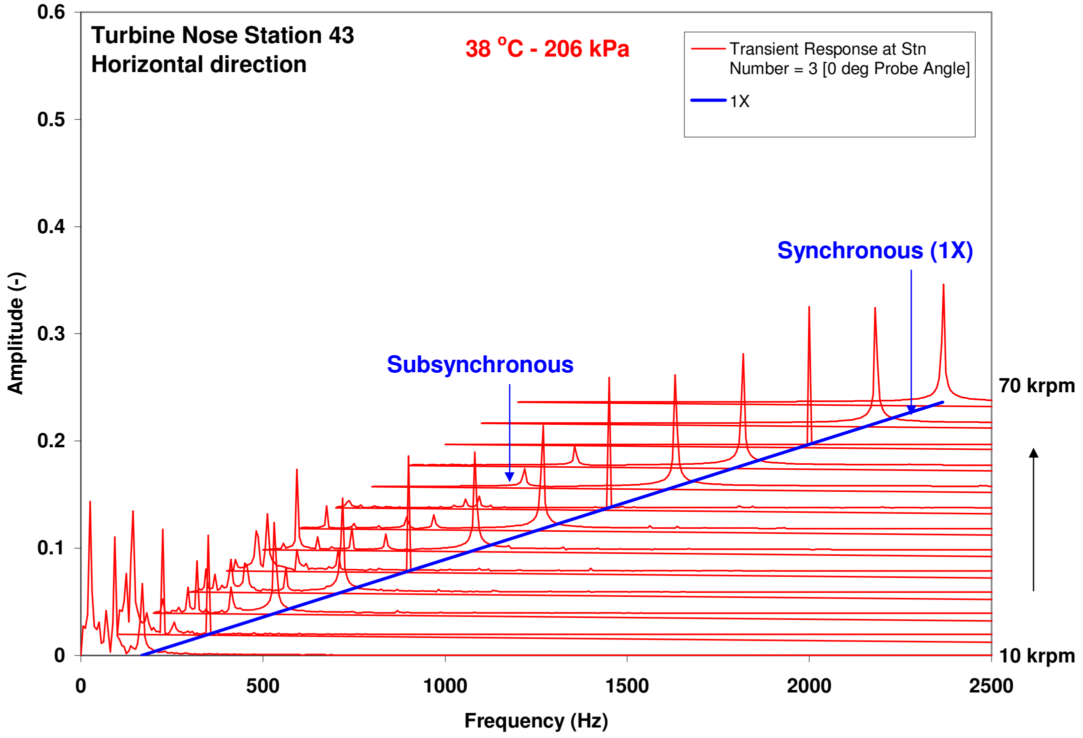

Figure 45 Waterfall of predicted horizontal shaft motions at the compressor (top) and turbine (bottom) ends of the TC rotor. Lubricant feed pressure of 206 kPa and inlet temperature equal to 38 °C

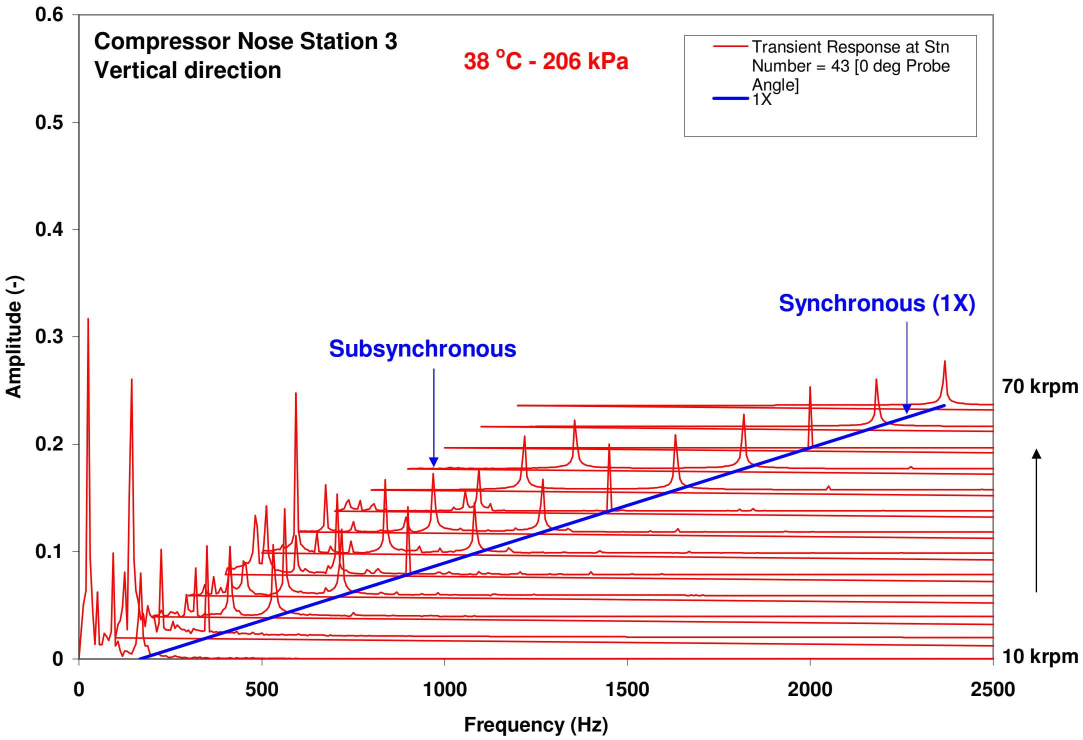

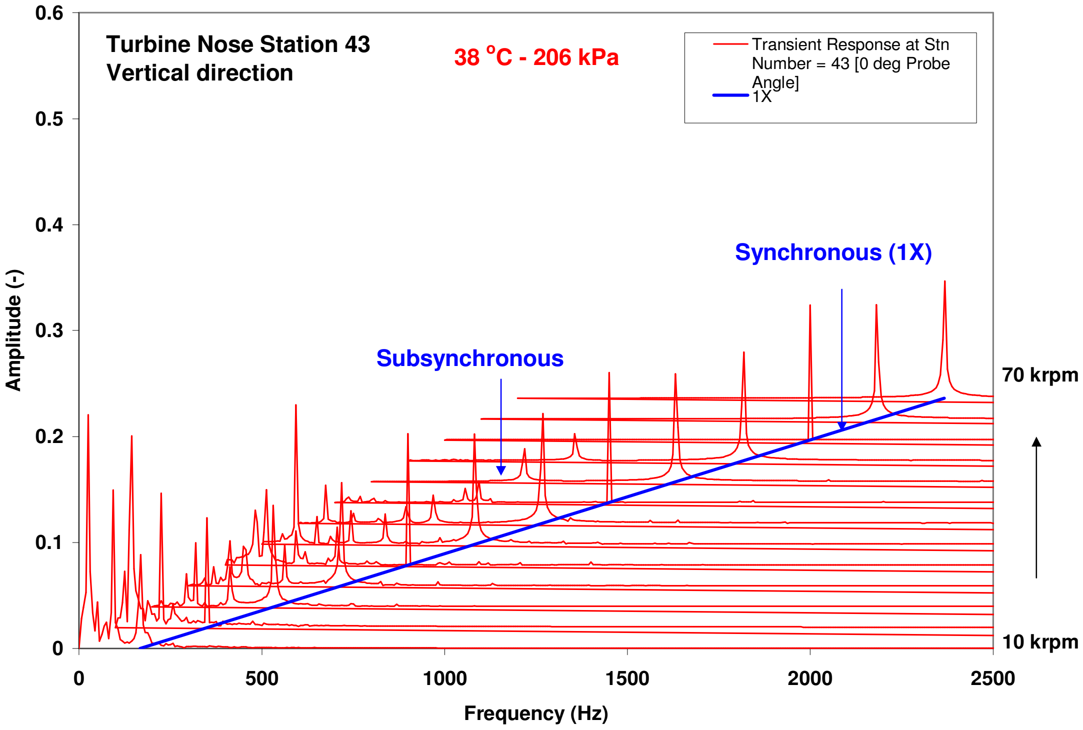

Figure 46 Waterfall of predicted vertical shaft motions at the compressor (top) and turbine (bottom) ends of the TC rotor. Lubricant feed pressure 206 kPa and inlet temperature equal to 38 °C

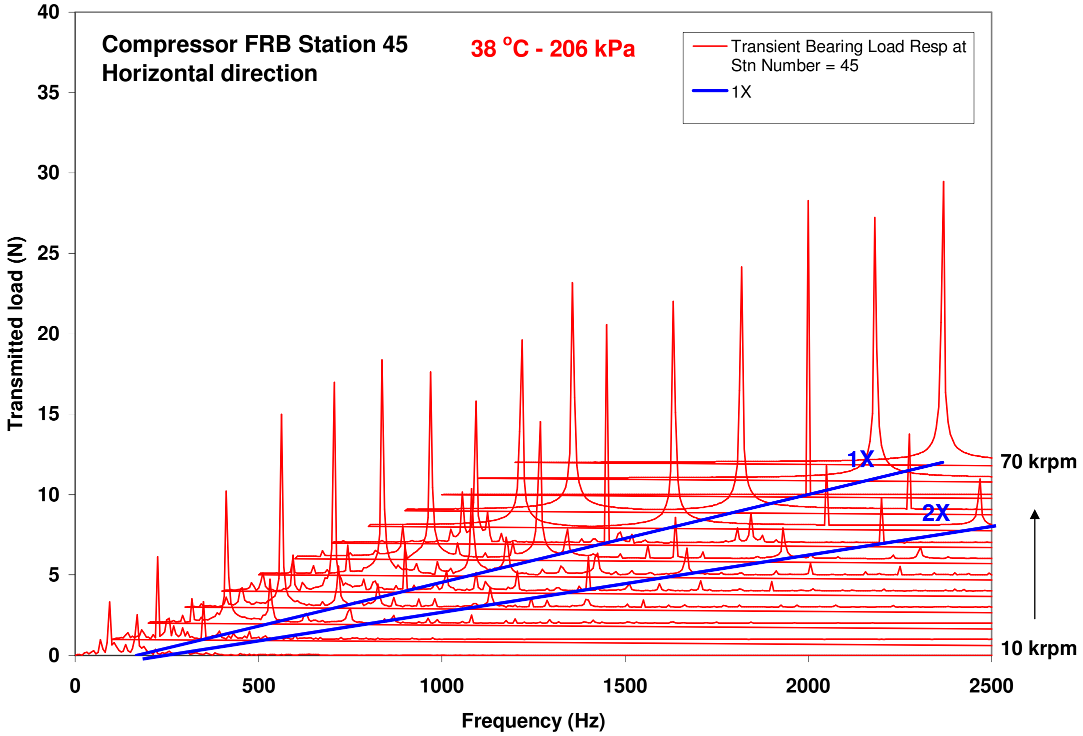

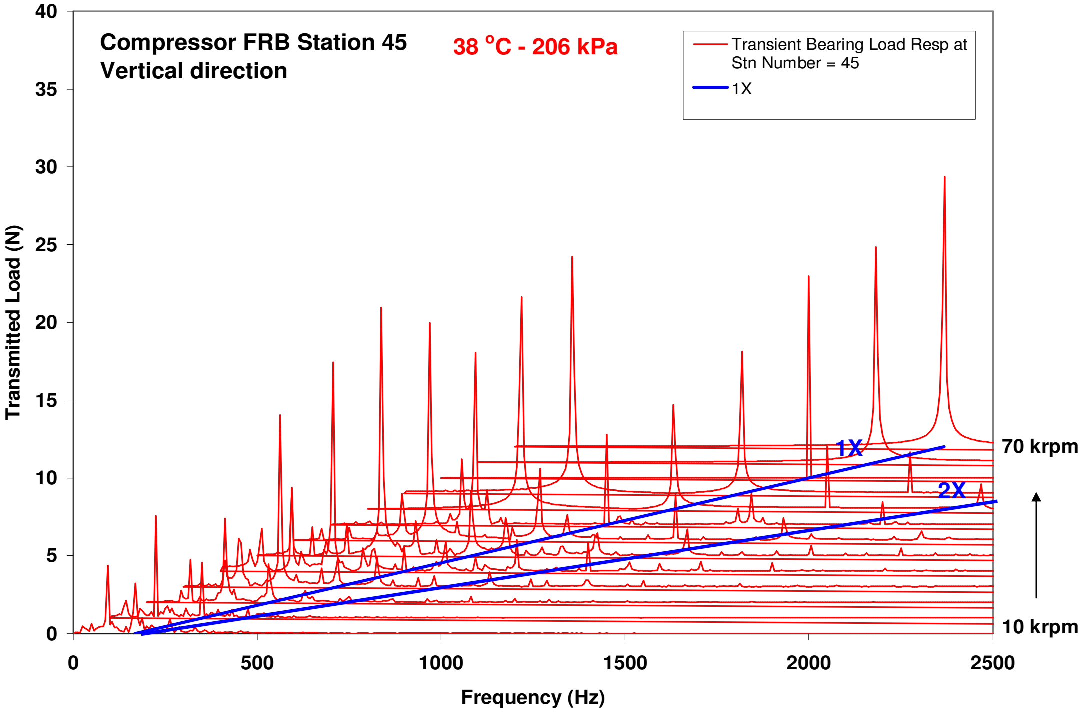

Figure 47 Horizontal (top) and vertical (bottom) transmitted forces at compressor side FRB. Lubricant feed pressure 206 kPa and inlet temperature equal to 38 °C

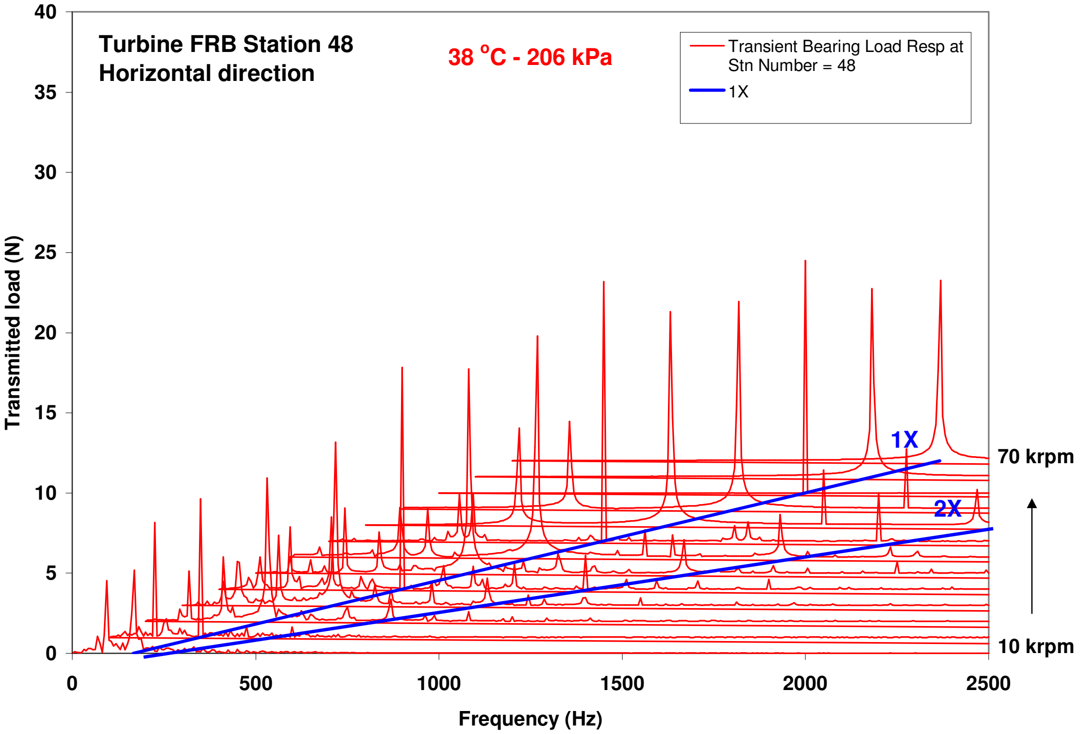

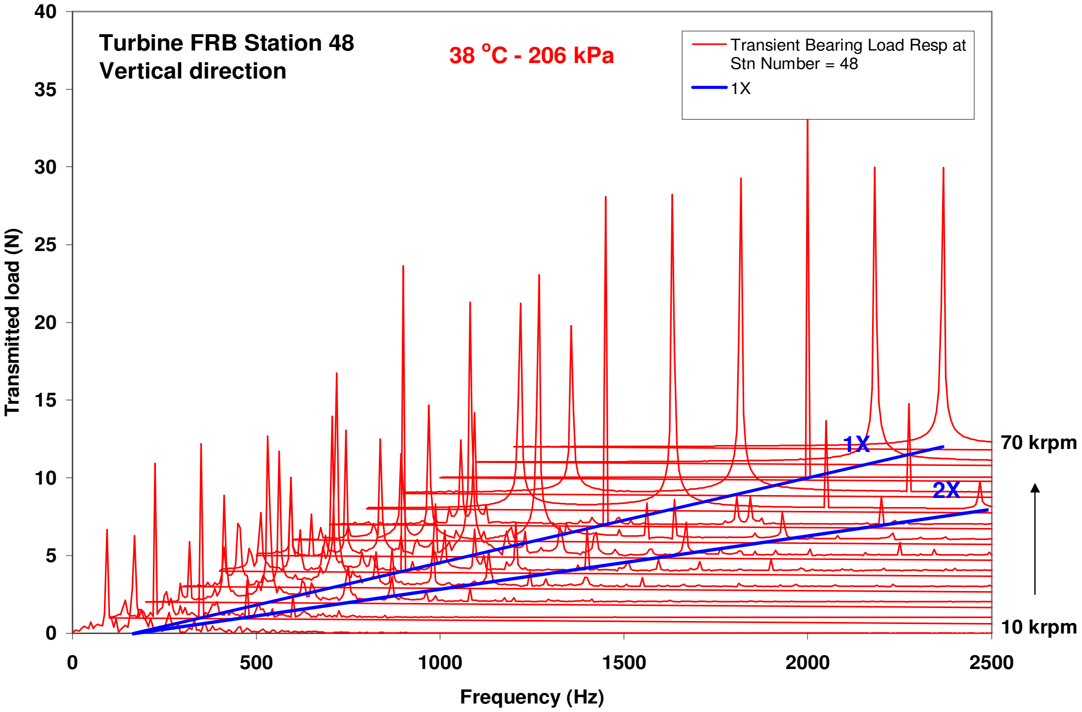

Figure 48 Horizontal (top) and vertical (bottom) transmitted forces at turbine side FRB. Lubricant feed pressure 206 kPa and inlet temperature equal to 38 °C

The waterfalls of shaft motion and transmitted loads for the tests and predictions reveal a complex rotor response, rich in subsynchronous activity. The test data and FFT predictions are filtered to capture the amplitude and frequency of the peak responses, including the synchronous components. The threshold amplitude for the analysis is 3% of the physical limit.

Figure 49 depicts the filtered subsynchronous frequencies of motion versus shaft speed. The top graph corresponds to the predicted (nonlinear) and measured subsynchronous frequencies at the compressor end of the TC while the bottom graph shows the results at the turbine end. The results are for a lubricant feed pressure of 206 kPa and inlet temperature of 38 ^{o}C. In addition, damped natural frequencies (predicted) and ring speed ratios (measured) are also included. The test data and nonlinear predictions show some agreement with the predicted rotor conical mode, in particular the nonlinear predictions. At low shaft speeds, below 30 krpm, the measured subsynchronous frequencies at the compressor end of the TC rotor are related to the line that tracks half of the ring speed. Therefore, this instability is attributed to the outer lubricant film of the FRB. On the other hand, the nonlinear analysis predicts an instability (at the compressor and turbine ends) related to half of the ring plus shaft speed. This motion is evident in the test data only at the compressor end of the rotor and for shaft speeds below 25 krpm and above 65 krpm. In general, the tests shows the excitation of two subsynchronous whirl frequencies; the first one with frequencies ranging from 60 Hz to 200 Hz and the second one with frequencies ranging from 130 Hz to 500 Hz (compressor end only).

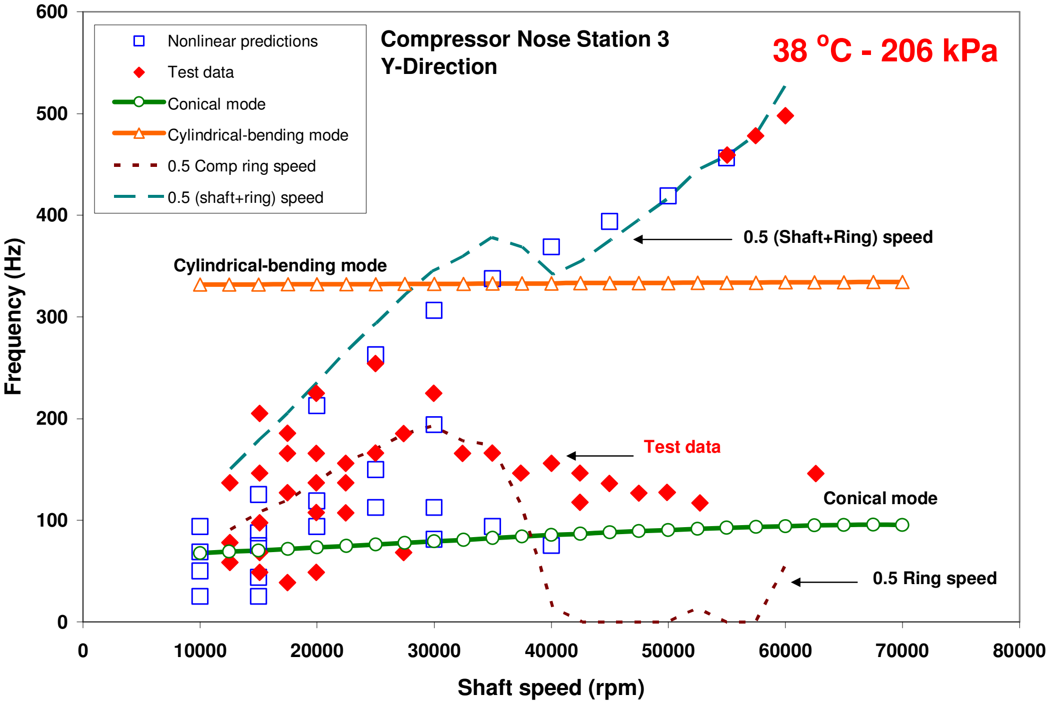

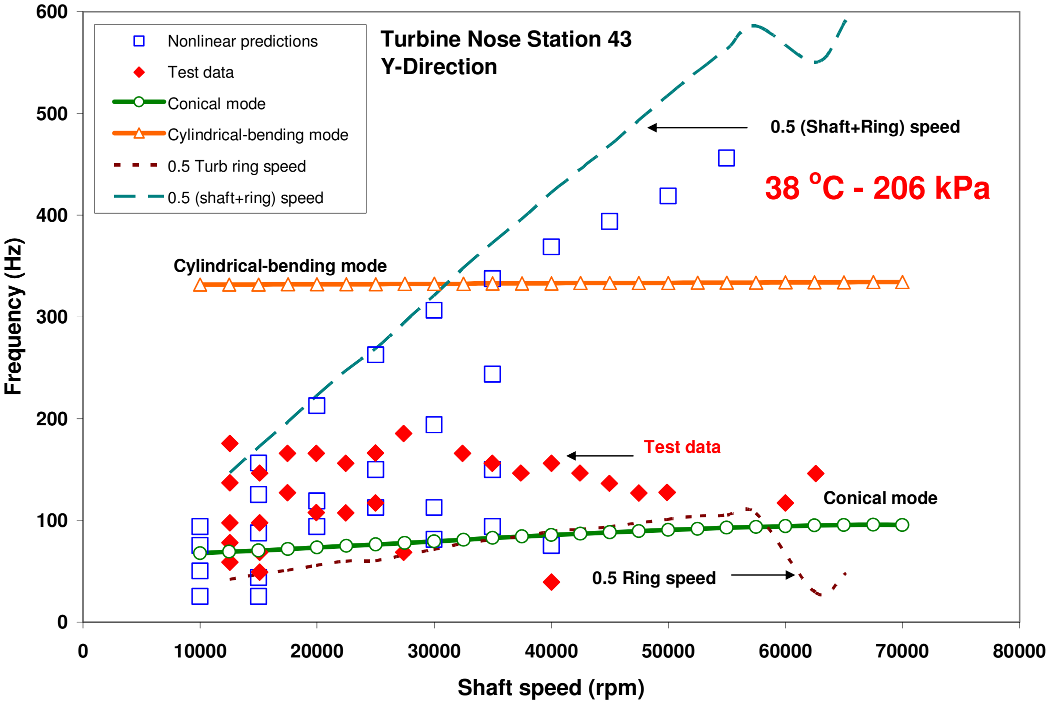

Figure 49 Compressor (top) and Turbine (bottom) rotor ends whirl frequency of subsynchronous motions versus shaft speed. Lubricant feed pressure of 206 kPa and inlet temperature of 38 ^{o}C

Figure 50 displays the measured and predicted (nonlinear) dimensionless amplitudes of subsynchronous motions versus shaft speed. The results are for a lubricant feed pressure of 206 kPa and inlet temperature equal to 38 ^{o}C. The top and bottom graphs show results for the compressor and turbine ends of the TC rotor, respectively. In addition, the test data is denoted by diamond markers and the square markers represent the nonlinear predictions. The test data shows that the largest amplitudes of subsynchronous motions occur at low shaft speeds (< 20 krpm). This specific trend is observed at both compressor and turbine end of the rotor and is well predicted by the nonlinear analysis. Although, note that the test data shows more subsynchronous activity than the predictions. At higher shaft speeds, above 20 krpm, the measured and predicted amplitudes of subsynchronous motions reach maximum amplitudes equivalent to 10% of the physical limit; predicted amplitudes are slightly smaller than the measurements at shaft speeds above 35 krpm.

Figure 51 depicts the measured and predicted (nonlinear) amplitudes of subsynchronous motions versus their corresponding whirl frequencies. The results are for the same operating conditions and shaft locations mentioned above. The measurements indicate that the subsynchronous motions with the largest amplitudes occur at a frequency of approximately 150 Hz for both compressor and turbine shaft ends, i.e., excitation of the rotor conical mode. The predictions follow a similar trend (amplitudes and frequencies) as in the test data. The nonlinear analysis predicts the largest amplitudes of subsynchronous motions at a frequency of approximately 100 Hz. The predictions agree well with the measurements showing a large concentration of subsynchronous motions at frequencies below 300 Hz for the compressor end and 150 Hz for the turbine end. However, the nonlinear analysis also predicts subsynchronous motions with decreasing amplitudes at higher frequencies ranging from 200 Hz to 450 Hz.

.

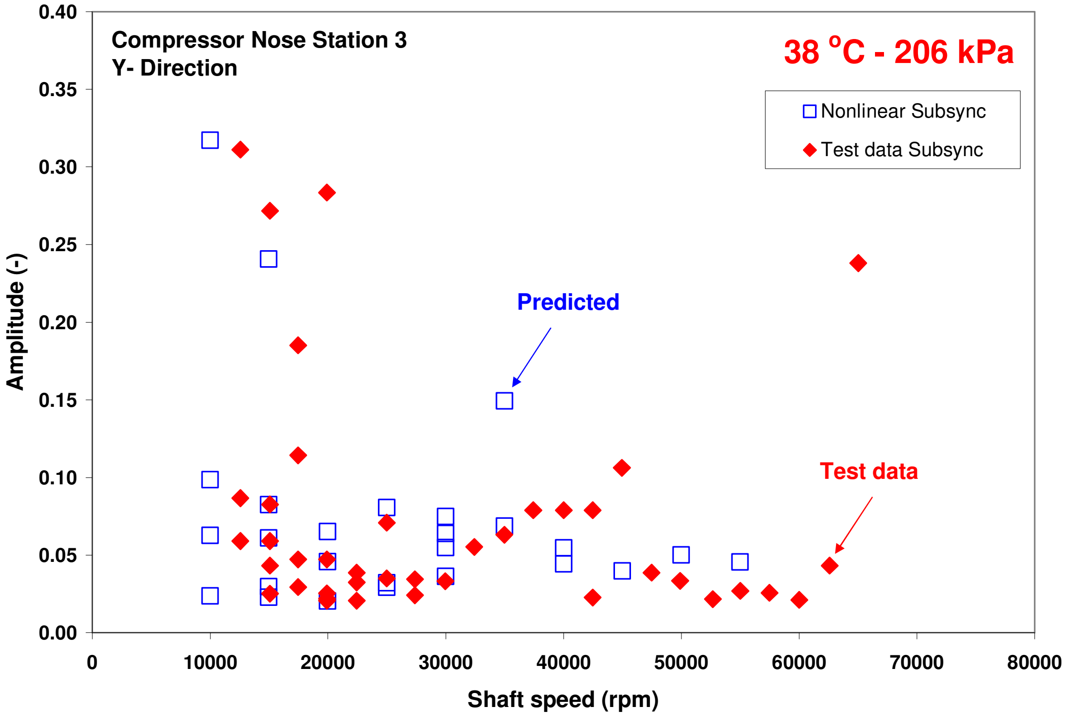

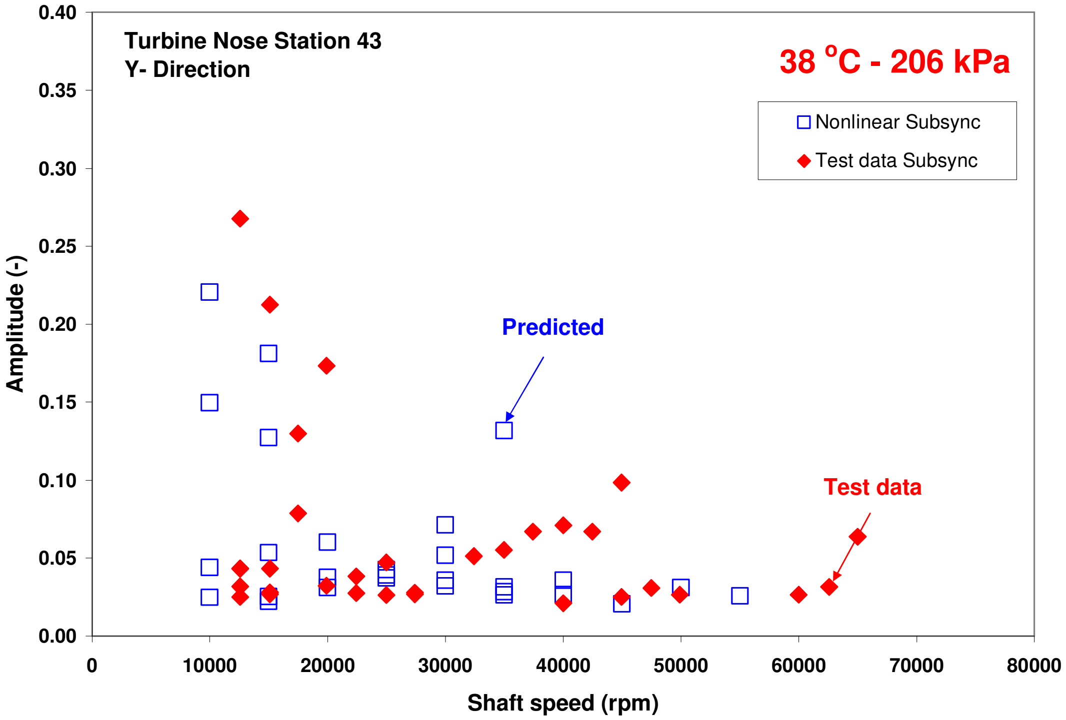

Figure 50 Amplitudes of subsynchronous motions (*Y*-direction) versus shaft speed at the compressor (top) and turbine (bottom) ends of the TC rotor. Lubricant feed pressure of 206 kPa and inlet temperature of 38 °C

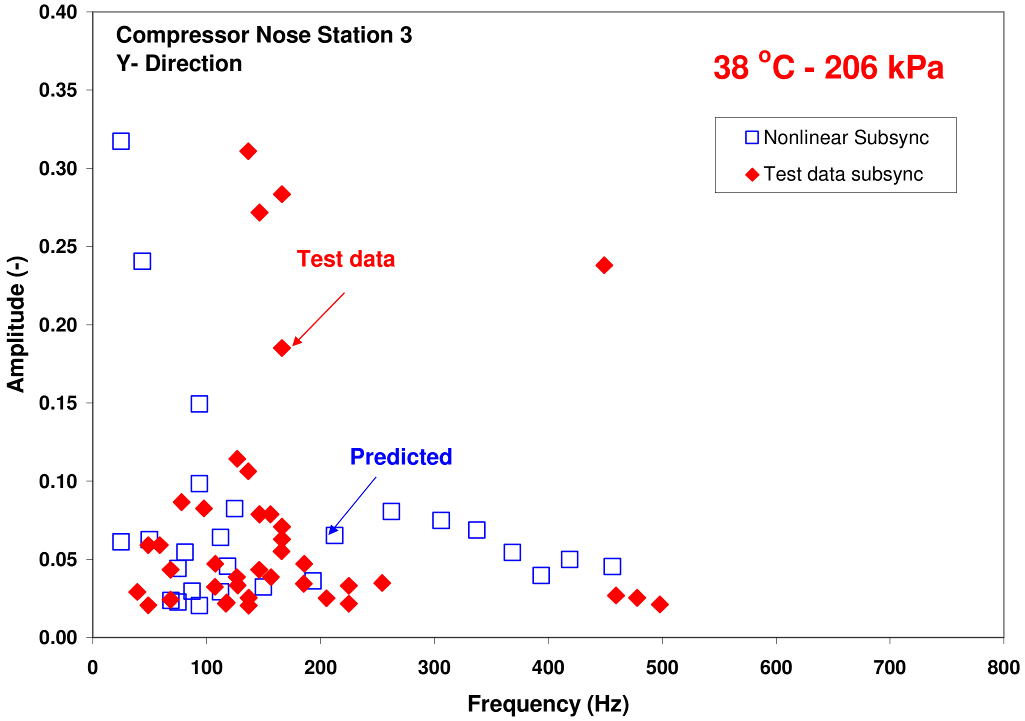

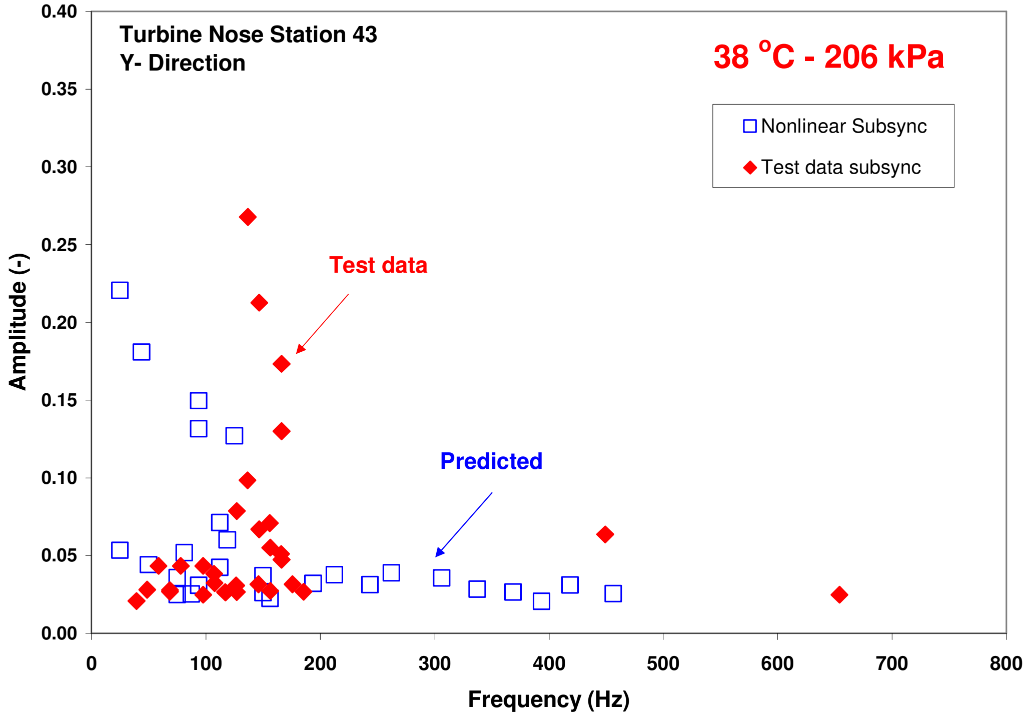

Figure 51 Amplitudes of subsynchronous motions (*Y*-direction) versus frequency speed at the compressor (top) and turbine (bottom) ends of the TC rotor. Lubricant feed pressure of 206 kPa and inlet temperature of 38 °C

Figure 52 displays the dimensionless amplitudes of subsynchronous motions versus *WFRs* at the compressor (top) and turbine (bottom) ends of the TC rotor. As it was discussed in Chapter IV, the test data evidences the existence of two characteristic whirl frequency ratios (*WFRs*). Test data subsynchronous motions are concentrated at *WFRs* ranging from 0.12-0.20 and 0.50-0.60; the largest amplitudes of vibration are associated to the higher *WFRs*. The results from the nonlinear analysis also show large concentration of *WFRs* similar to the test data. Although, it is important to note that the nonlinear analysis predicts the largest amplitudes of subsynchronous motions to be associated to the lower *WFRs* (0.12-0.2). In addition, the predictions show more subsynchronous motions with low amplitudes and *WFRs* between 0.5 and 0.65 than the measurements.

The nonlinear transient analysis also yields predictions of total shaft motion amplitudes (pk-pk) at the compressor and turbine ends of the TC rotor. The limit cycle orbits define the total shaft motion. Figure 53 depicts the predicted and measured amplitudes of total shaft motion for a lubricant feed pressure of 206 kPa and inlet temperature equal to 38 ^{o}C. The amplitudes are shown in dimensionless form relative to the physical limit of maximum conical motion at the turbine nose (0.508 mm pk-pk). As expected, from the measured and predicted synchronous (*1X*) and subsynchronous motions, the largest total motion amplitudes occur at the lowest shaft speeds (< 20 krpm). At higher shaft speeds, the amplitudes of total motion decrease rapidly with increasing shaft speed, in particular at the compressor end. The slightly smaller than test data predicted amplitudes of total motion at shaft speeds below 20 krpm may be attributed to the poorly predicted synchronous (*1X*) amplitudes. Note that for shaft speeds above 55 krpm, the predicted response is purely synchronous (refer to Figure 45 and Figure 46). On the other hand, the test data shows large total motion amplitudes (refer to Figure 23 and Figure 24). There is excellent correlation of predictions to test data for shaft speeds ranging from 25 krpm to 60 krpm. Despite the large synchronous (*1X*) and subsynchronous amplitudes in the test data and predictions, the amplitudes of total shaft motion are well below the physical limit.

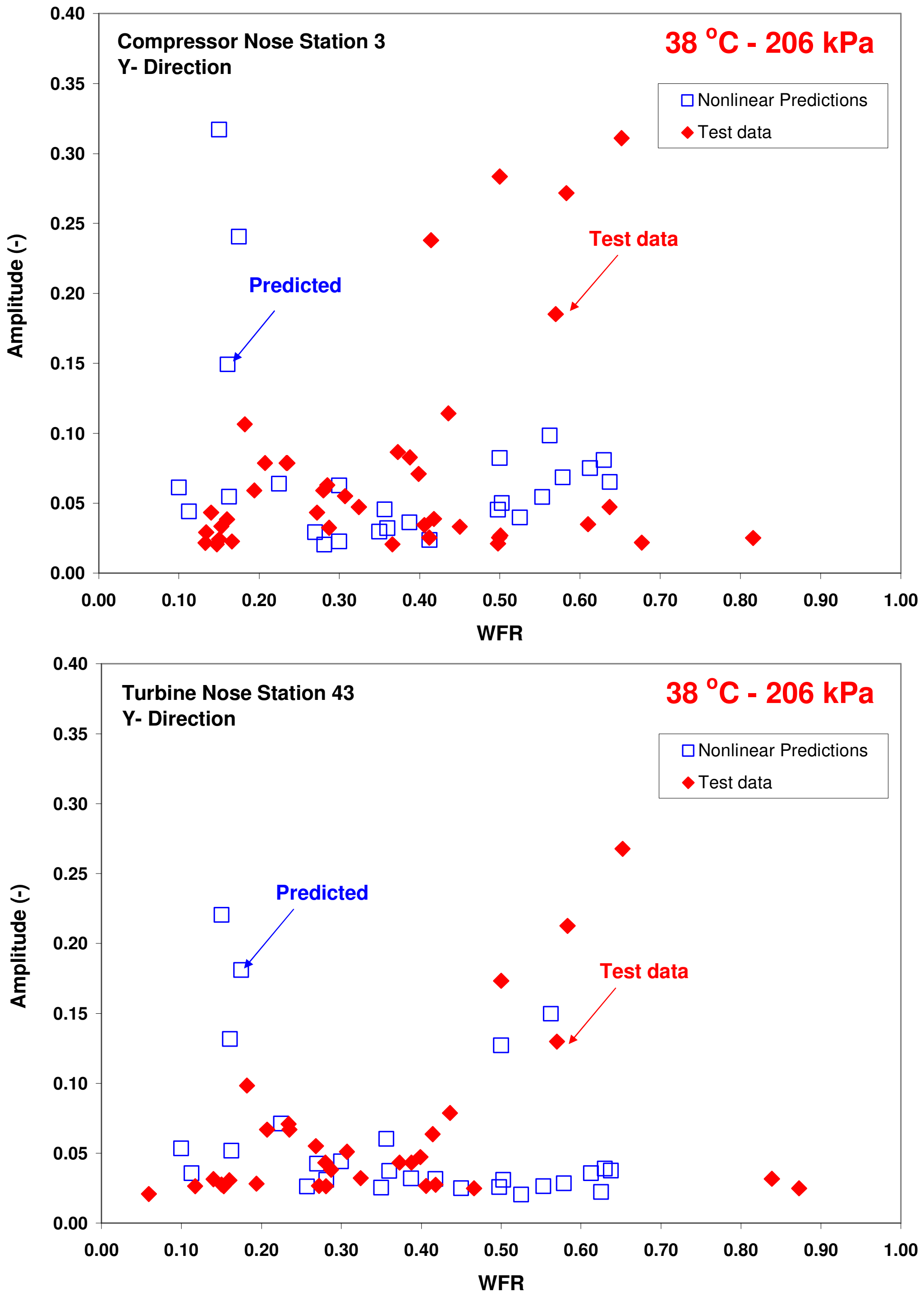

Figure 52 Predicted and measured subsynchronous amplitudes versus *WFRs* at the compressor (top) and turbine (bottom) ends of the TC rotor. Lubricant feed pressure of 206 kPa and inlet temperature of 38 °C

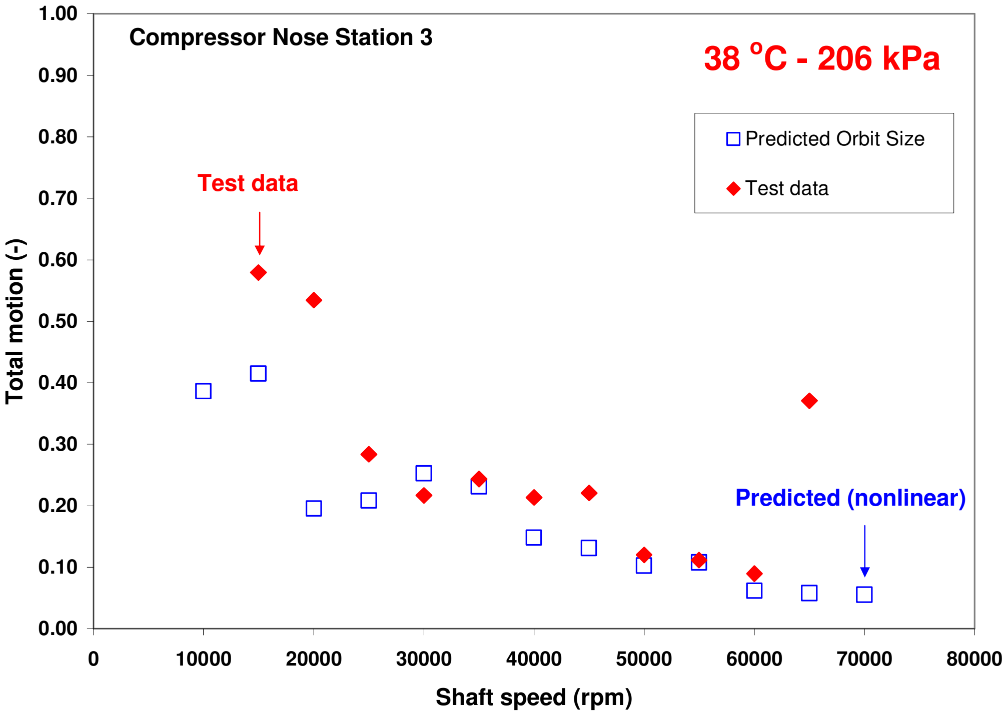

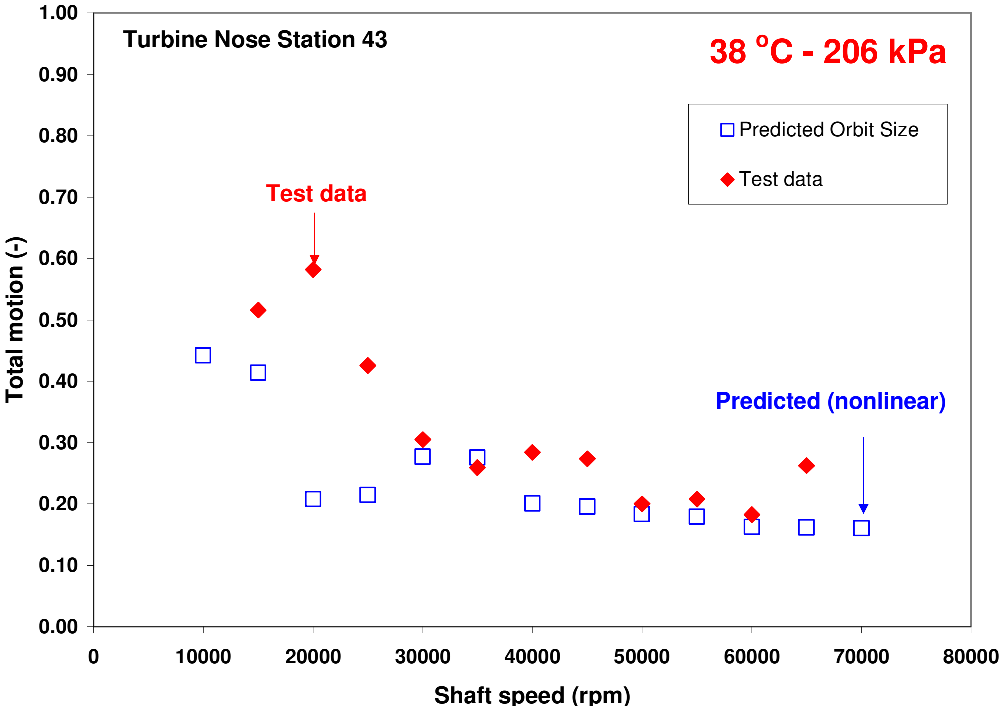

Figure 53 Predicted and measured total shaft motion (pk-pk) at the compressor (top) and turbine (bottom) ends of the TC rotor. Lubricant feed pressure of 206 kPa and inlet temperature of 38 °C

Predictions without floating ring at top shaft speeds

The measured floating ring speed ratios in Figure 10 to Figure 11 show scattered data points for shaft speeds greater than approximately 50 krpm. It is of importance to verify whether the floating rings stopped spinning or the peculiar test data is caused by malfunctioning of the motion sensors. Consecutively, a time response nonlinear prediction is obtained removing the floating rings in the structural model. Thus, the analysis is performed assuming that the floating ring bearing is locked (no rotation or whirl) and it behaves like a plain journal bearing. The ring speed and shaft motion test data in Figure 54 depicts the dimensionless amplitudes of subsynchronous motions versus *WFRs* for the compressor and turbine ends of the rotor. As expected, the nonlinear predictions show large amplitudes of subsynchronous motions at a *WFR* equal to 0.5, typical in plain cylindrical journal bearing. Note that the results obtained with predicted ring speeds for all shaft speeds do not show this large amplitudes of subsynchronous motions at a *WFR* of 0.5 (refer to Figure 52). Hence, the large amplitudes of subsynchronous motions in the test data with *WFR* of 0.5 originate due to the lack of the outer lubricant film which acts as a squeeze film damper when the ring is locked. This occurrence is more evident in Figure 55 which shows the predicted and measured subsynchronous *WFRs* versus shaft speed at the compressor and turbine ends of the TC rotor. The results obtained with ring speed rotation for all shaft speeds are presented in Figure 38. The results in Figure 55 show a concentration of data points at a *WFR* equal to 0.5 and shaft speeds above 50 krpm, agreeing well with the test data for the compressor end. At the turbine end of the TC, the test data does not show subsynchronous motions with WFR equal to 0.5 since the floating ring stopped rotating at shaft speeds above 60 krpm and the maximum tested shaft speed equals 62.5 krpm.

In general, the scattered data points in Figure 10 to Figure 13 do not represent a malfunctioning of the motion sensors but show that the compressor and turbine side floating rings stopped rotating at shaft speeds above 50 krpm and 60 krpm, respectively. Appendix B shows predicted and test data displacement waterfalls, total shaft motion, and synchronous and subsynchronous amplitudes for the time transient analysis described above.

In addition, a time transient analysis was conducted with the test ring speeds ratios. The purpose of this analysis is to demonstrate the effect of the rotational speed of the rings on the TC shaft motions. Table 8 shows the test data ring speed ratios used for the time transient analysis.

Table 8 Ring speed ratios for time transient analysis

Shaft speed	Ring speed ratio	
RPM	Comp FRB	Turb FRB
10000	0.43	0.40
15000	0.42	0.37
20000	0.41	0.33
25000	0.40	0.28
30000	0.38	0.28
35000	0.29	0.27
40000	0.25	0.23
45000	0.20	0.20
50000	0.15	0.17
55000	0.10	0.15
60000	-	-
65000	-	-
70000	-	-

The predicted results in Appendix B show that at high shaft speeds (> 50 krpm) the floating rings are locked (inner fluid film acting only), resulting in large amplitudes of subsynchronous motions. The test data shows these large amplitudes of motion at shaft speeds above 60 krpm. Hence, the results shown in Figure 63 to Figure 76 in Appendix C show the locked floating rings at shaft speeds above 60 krpm.

The predicted results show large amplitudes of subsynchronous motions at low shaft speeds (< 30 krpm). Note that the test data shows the highest ring speed ratios for these shaft speeds. Thus, it is suspected that these subsynchronous motions with large amplitudes originate due to the high rotational speed of the floating rings compared to the shaft speed, which lessen the operation of the outer lubricant film as a squeeze film damper. On the other hand, the predictions for the compressor and turbine ends show subsynchronous motions with low amplitudes for shaft speeds greater than 30 krpm and lower than 60 krpm. Thus, at these shaft speeds the floating rings do not spin but they only whirl, allowing the outer film to act as a squeeze film damper. At higher shaft speeds (> 60 krpm) the predictions and measurements show large amplitudes of subsynchronous motions due to the lack of whirl and rotation of the floating rings.

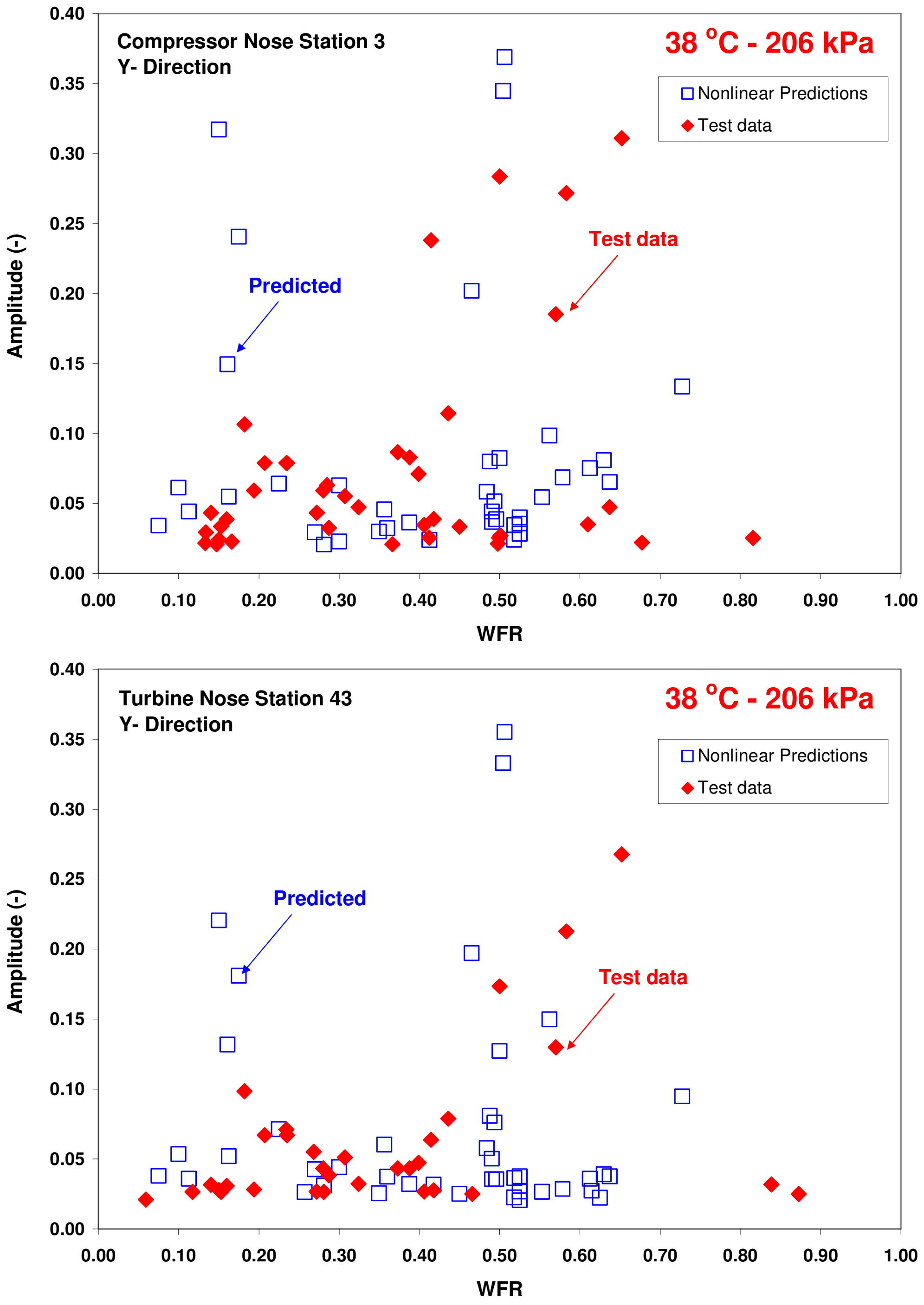

Figure 54 Predicted and measured subsynchronous amplitudes versus *WFRs* at the compressor (top) and turbine (bottom) ends of the TC rotor. Lubricant feed pressure of 206 kPa and inlet temperature of 38 °C. <u>Removed floating ring for shaft speeds above 50 krpm</u>

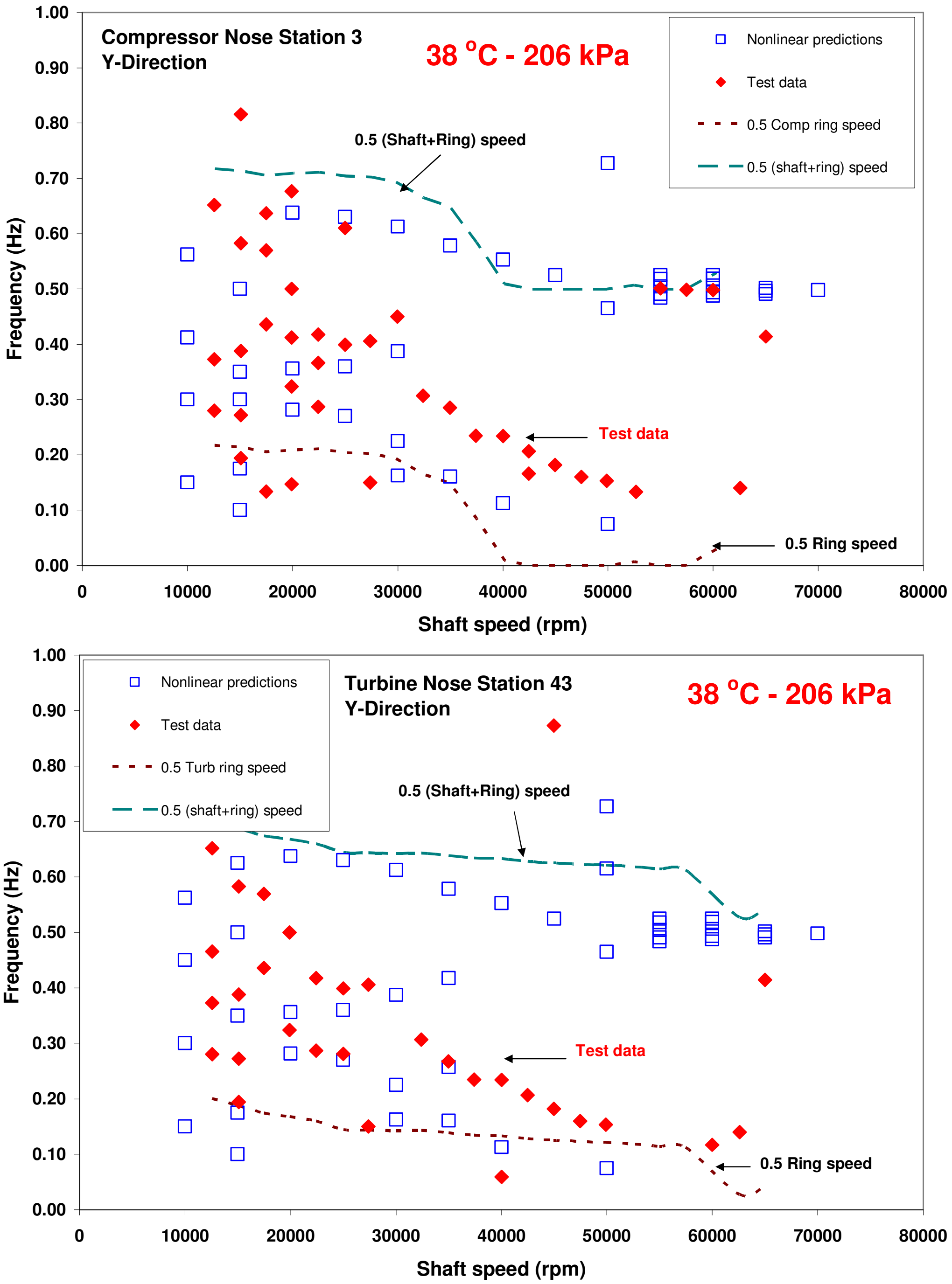

Figure 55 Predicted and measured WFRs versus shaft speed at compressor (top) and turbine (bottom) ends. Lubricant feed pressure of 206 kPa and inlet temperature of 38 °C. <u>Removed floating ring for shaft speeds above 50 krpm</u>

The good agreement between predictions (nonlinear) and measurements demonstrate the progress on the development of computational tools for accurate prediction of the complex shaft motions encountered in turbochargers. The linear eigenvalue analysis predicts three critical speeds at approximately 4, 20 and 70 krpm associated to the rotor conical, cylindrical-bending and first bending modes, respectively. The predicted damping ratios and natural frequencies show that the rotor conical and cylindrical-bending modes are unstable (damping ratios < 0). The first bending mode is predicted to be stable (damping ratios > 0) over the entire speed range considered (10 krpm to 70 krpm). Although, the rotor conical mode shows significant dependence on the lubricant feed pressure, becoming stable at lower shaft speeds as lubricant feed pressure increases. The linear model yields predicted synchronous (1X) motions that agree well with the test data for all shaft speeds. On the other hand, the nonlinear model predicts well the synchronous (1X) amplitudes at high shaft speeds only (> 45 krpm). The time transient analysis predicts subsynchronous motions with similar amplitudes and frequencies as in the test data for shaft speeds ranging from 10 krpm to 55 krpm. Measurements show subsynchronous motions along the entire operating speed range (10 krpm – 65 krpm). Hence, the linear model can be used to calculate accurately the synchronous (1X) response and the nonlinear model to predict the multiple frequencies of subsynchronous motions along with their corresponding amplitudes.

CHAPTER VI
CONCLUSIONS

This thesis presents progress on the development of linear and nonlinear rotordynamic models to accurately predict the dynamic shaft response of TC rotors supported on FRBs. The results show significant improvements in predicting the TC shaft motions, in particular with the proper estimation of imbalance, clearances and the rapidly varying side loads due to lubricant feed pressure. The numerical results presented demonstrate the complex shaft motions encountered in automotive turbocharger dynamics. More importantly, it shows the importance of using accurate rotordynamic models for accurate predictions of turbocharger shaft motions. The most significant conclusions of this research follow.

Measurements of the rotational speed of the compressor and turbine side FRBs indicate that the ring speed ratio decreases with increasing shaft speed. Measured ring speed ratios show that the floating ring speed decreases steadily from 40% to 20% of shaft speed, showing scattered data points at shaft speeds higher than 50 krpm and 60 krpm for both compressor and turbine side floating rings, respectively. A subsequent time transient analysis in which the ring speed ratios were arbitrarily set equal to 1% of the shaft speed proves that the scattered points do not show malfunctioning of the motion sensors but indicate that the floating rings stopped rotating. Predicted ring speed ratios follow the test data trend line, showing good correlation for shaft speeds ranging from 20 krpm to 45 krpm. However, the fluid film bearing analysis does not predict a null ring rotational speed at the highest shaft speeds as observed in the test data. A better estimation of the hydrostatic loads acting on the FRBs would yield better correlation of predictions to test data. Measurements and predictions for various lubricant feed pressures and temperatures demonstrate that the ring rotational speeds do not depend greatly on the lubricant feed pressure or inlet temperature.

The linear stability analysis (eigenvalue analysis) of the test rotor predicts the rotor cylindrical-bending mode to be unstable along the entire operating speed range. On the contrary, the rotor first bending mode is predicted to be stable for all shaft speeds. These two modes show no dependence on the lubricant feed pressure. However, the rotor conical mode is unstable from start up and becomes stable at lower shaft speeds as the lubricant feed pressure increases. Synchronous (*1X*) response measurements and predictions indicate the existence of a critical speed at approximately 20 krpm. This critical speed is associated to the excitation of the rotor cylindrical-bending mode.

Predicted synchronous (*1X*) response to imbalance derived from the linear rotordynamic model yields good correlation to the test data at low (< 20 krpm) and high shaft speeds (> 35 krpm). The shaft motion measurements at the compressor and turbine ends of the TC rotor show synchronous (*1X*) amplitudes that peak at approximately 20 krpm and decrease as shaft speed increases. The synchronous response at the turbine end shows larger amplitudes than for the compressor end due to the larger imbalance mass on the turbine wheel. Significant improvements in the predicted synchronous (*1X*) motions was achieved when using a mass imbalance distribution estimated from the actual shaft motion measurements. Additionally, the linear predictions and measurements indicate that the synchronous response to imbalance of the TC rotor does not depend on the lubricant feed pressure or inlet temperature. The results obtained from the time response simulations (nonlinear analysis) underpredict slightly the measured synchronous (*1X*) amplitudes from start up to approximately 45 krpm by approximately 70-90%, showing good correlation to the test data at higher shaft speeds only.

The waterfall spectra of the TC shaft motions show multiple subsynchronous frequencies along the entire operating speed range (10 krpm to 70 krpm). Post processing of the raw test data using mathematical software evidences two main subsynchronous vibrations at whirl frequency ratios equal to 0.12 - 0.2 and 0.5 - 0.6, the last one showing the largest amplitudes of vibration. The large amplitudes of subsynchronous motions originate at shaft speeds above 50 krpm due to the lack of rotation of the floating rings. The nonlinear analysis predicts well the amplitudes and frequencies of subsynchronous motions; although it predicts a purely synchronous response at shaft speeds above 55 krpm. The measured and predicted subsynchronous motions show a slight dependence on the lubricant feed pressure. The analyses indicate that using larger side loads at high shaft speeds induces more subsynchronous activity in the nonlinear predictions.

REFERENCES

[1] Shaw, C., and Nussdorfer, T., 1947, "An Analysis of the Full-Floating Journal Bearing," NACA Report No. 866, pp. 95-107.

[2] Born, H., 1987, "Analytical & Experimental Investigation of the Stability of the Rotor-Bearing System of a New Small Turbocharger," *Gas Turbine Conference and Exhibition*, ASME Paper No. 87-GT-110.

[3] San Andrés, L., 2000, "Notes 4. Static Load Performance of Plain Journal Bearings," Texas A&M University MEEN 626 –Lubrication Theory Class Notes, pp. 1-13.

[4] Orcutt, F., and Ng, C., 1968, "Steady-State and Dynamic Properties of the Floating-Ring Journal Bearing," Journal of Lubrication Technology, **90,** pp. 243 – 253.

[5] Tanaka, M., 1996, "A Theoretical Analysis of Stability Characteristics of High Speed Floating Bush Bearings," *IMechE Conference Transactions of 6th International Conference on Vibrations in Rotating Machinery*, pp. 133-142.

[6] Tatara, A., 1970, "An Experimental Study on the Stabilizing Effect of Floating Bush Journal Bearings," Bulletin of the JSME, **13**, pp. 859-863.

[7] Tanaka, M., and Hori, Y., 1972, "Stability Characteristics of Floating Bush Bearings," Trans. ASME Journal of Lubrication Technology, **94**, pp. 248-259.

[8] Trippett, R., and Li, D., 1983, "High-Speed Floating-Ring Bearing Test and Analysis," ASLE Transactions, **27**(1), pp. 73-81.

[9] Li, C., 1982, "Dynamics of Rotor Bearing Systems Supported by Floating Ring Bearings," Journal of Lubrication Technology, **104**, pp. 469-477.

[10] Holt, C., and L. San Andrés, 2003, "Test Response of a Turbocharger Supported on Floating Ring Bearings – Part I: Assessment of Subsynchronous Motions," *Proceedings of the 19th Biennial Conference on Mechanical Vibration and Noise*, Paper No. DETC 2003/VIB-48418 Chicago, IL.

[11] Holt, C., and L. San Andrés, 2003, "Test Response of a Turbocharger Supported on Floating Ring Bearings – Part II: Comparisons to Nonlinear Rotordynamic Predictions," *Proceedings of the 19th Biennial Conference on Mechanical Vibration and Noise*, Paper No. DETC 2003/VIB-48419, Chicago, IL.

[12] L. San Andrés, and Kerth, J., 2004, "Thermal Effects on the Performance of Floating Ring Bearings for Turbochargers," Proceedings of the Institution of Mechanical Engineers, Part J: J. Engineering Tribology, **218**, pp. 1-14.

[13] Kerth, J., 2003, "Prediction and Measurement of the Rotordynamic Response of an Automotive Turbocharger with Floating Ring Bearings," MS Thesis, Texas A&M University, College Station, TX.

[14] San Andrés, L., Rivadeneira, J., Chinta, M., LaRue, G., and Gjika, K., 2005, "Nonlinear Rotordynamics of Automotive Turbochargers – Predictions and Comparisons to Test Data," ASME Paper No. GT2005-68177.

[15] *XLTRC^2 Rotordynamics Software Suite v.2.20*, 2004, Turbomachinery Laboratory, Texas A&M University.

[16] San Andrés, L., 2005, *XLSFRBThermal® Software Suite*, Tribology Group, Turbomachinery Laboratory, Texas A&M University, College Station, TX.

[17] San Andrés, L., "Revisions to Thermal Analysis for Floating Ring Bearings", Proprietary Technical Report, November 2004.

[18] *XLHYPAD© Software Suite*, Turbomachinery Laboratory, Texas A&M University, College Station, TX.

[19] San Andrés, L., 2003, "Effects of Compressor Housing Orientation on the Dynamic Response of GT 37 Turbocharger", Proprietary Technical Report.

[20] Vance, J., 1987, *Rotordynamics of Turbomachinery*, John Wiley & Sons, New York, pp. 171 – 201.

APPENDIX A
FLOATING RING BEARING DIMENSIONS

Table 9 shows the FRB dimensions after testing. The measurements were performed by the sponsor company (October 2003) and at Texas A&M University (August 2005). The latest FRB dimensions were used in the analysis. The after testing dimensions show that severe rubbing occurred between the bearing and shaft and ring components. In addition, the inspection of the supply lubricant tank after numerous tests revealed debris from metal to metal contact. Figure 56 depicts a schematic view of a floating ring bearing cross section. The figure shows the post test dimensions of the ring and bearing component as used in the present analysis.

Table 9 FRB dimensions after testing

	October 2003		**August 2005**	
	Comp FRB mm	**Turb FRB** mm	**Comp FRB** mm	**Turb FRB** mm
Journal diameter	11.493	11.499	11.508	11.505
Floating ring inner diameter	11.532	11.537	11.543	11.541
Floating ring outer diameter	17.763	17.770	17.722	17.720
Bearing diameter	17.860	17.861	17.817	17.817
Inner film diametral clearance	0.0382	0.0384	0.0350	0.0356
Outer film diametral clearance	0.0966	0.0904	0.0950	0.0970

Note: August 2005 dimensions are the average of 5 measurements;
Measurements performed with a digital micrometer (uncertainty ± 0.00254 mm)
Reference [13] shows predictions for (Corner 1) diametral clearances $2\times C_i = 15\ \mu m$ and $2\times C_o = 42\ \mu m$

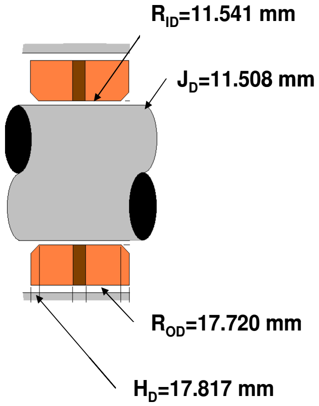

Figure 56 Compressor side FRB dimensions after testing (August 2005)

APPENDIX B

PREDICTIONS WITHOUT FLOATING RING AT SHAFT SPEEDS ABOVE 50 KRPM

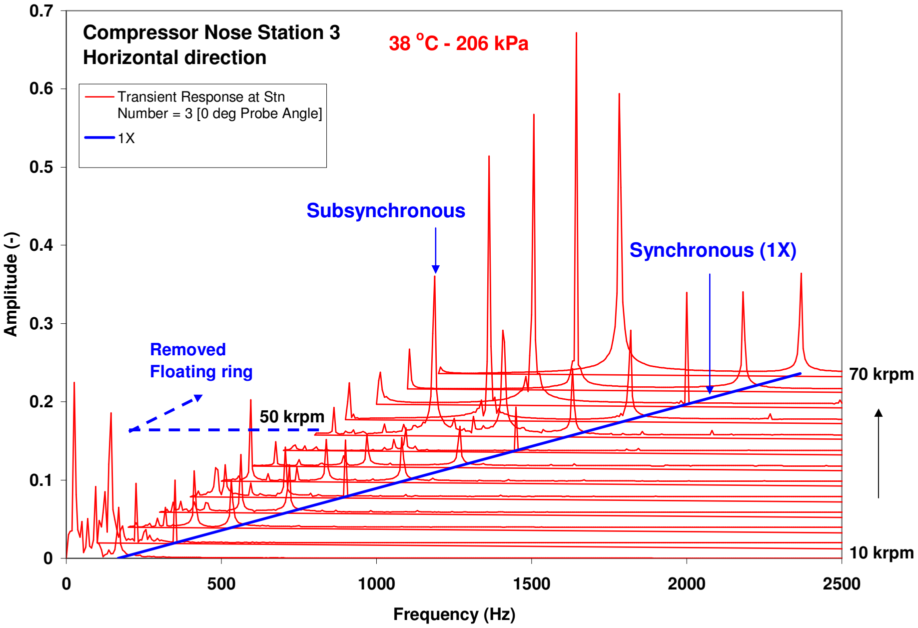

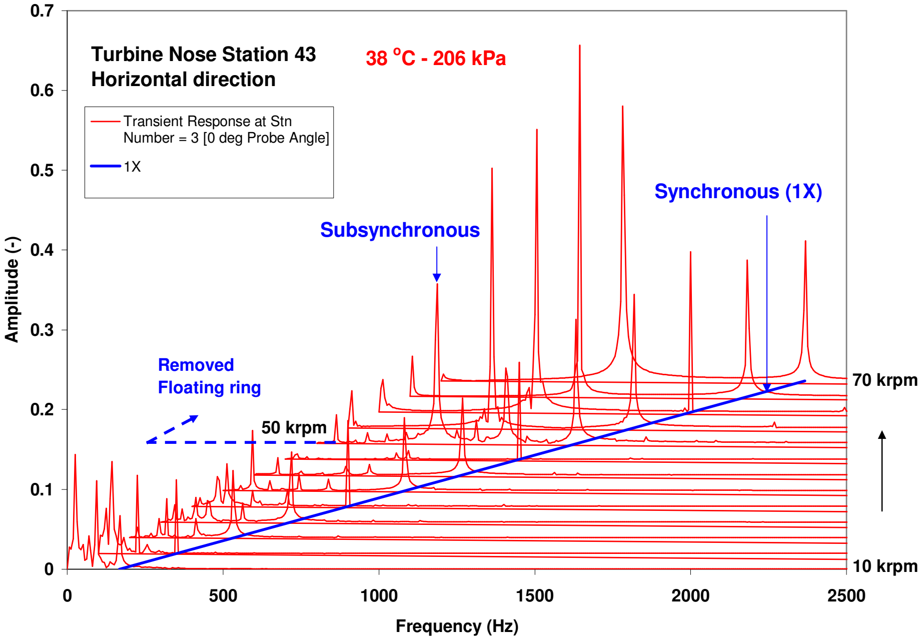

Figure 57 Waterfall of predicted horizontal shaft motions at the compressor (top) and turbine (bottom) ends of the TC rotor. Lubricant feed pressure of 206 kPa and inlet temperature equal to 38 °C. Removed floating ring for shaft speeds above 50 krpm

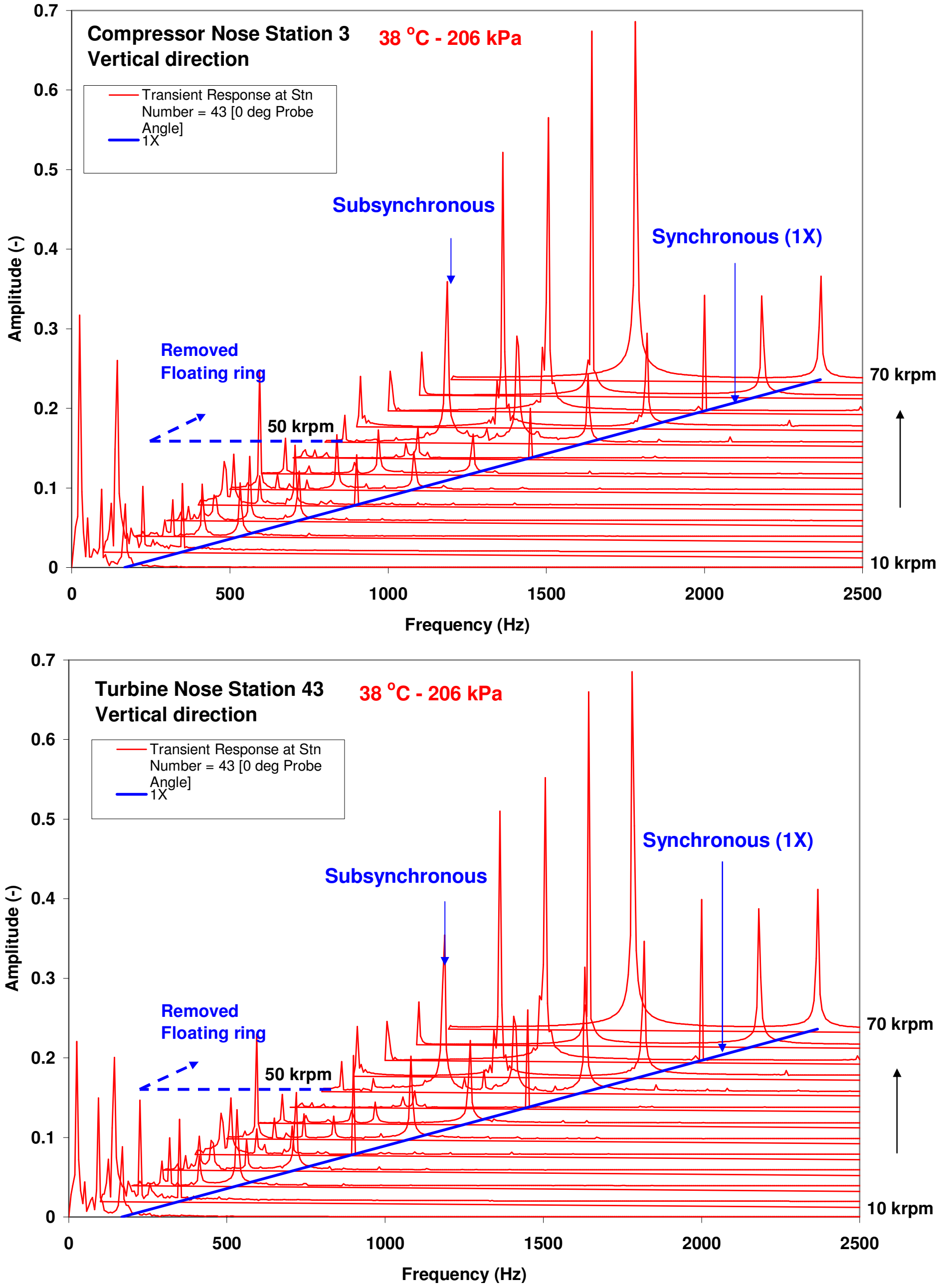

Figure 58 Waterfall of predicted vertical shaft motions at the compressor (top) and turbine (bottom) ends of the TC rotor. Lubricant feed pressure of 206 kPa and inlet temperature equal to 38 °C. Removed floating ring for shaft speeds above 50 krpm

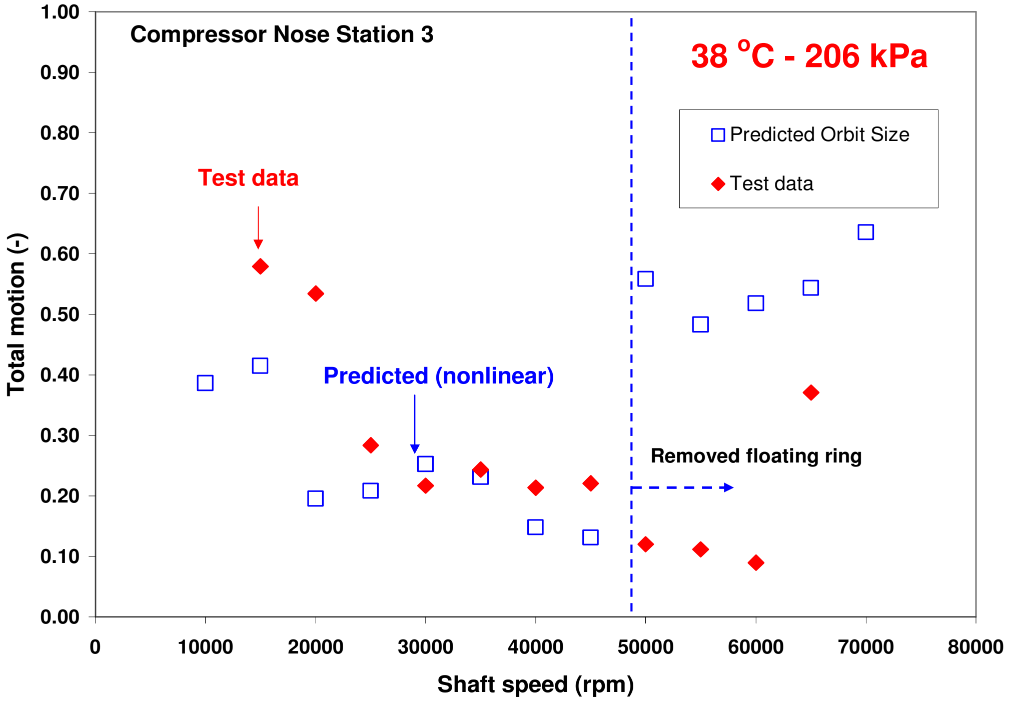

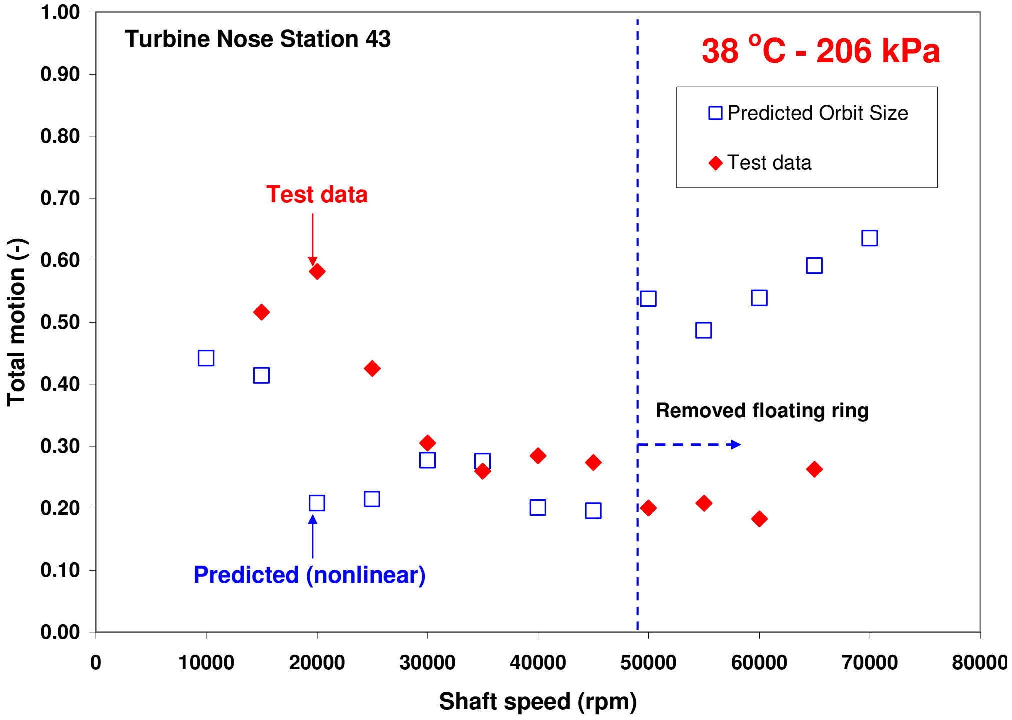

Figure 59 Predicted and measured total shaft motion (pk-pk) at the compressor (top) and turbine (bottom) ends of the TC rotor. Lubricant feed pressure of 206 kPa and inlet temperature of 38 °C. Removed floating ring for shaft speeds above 50 krpm

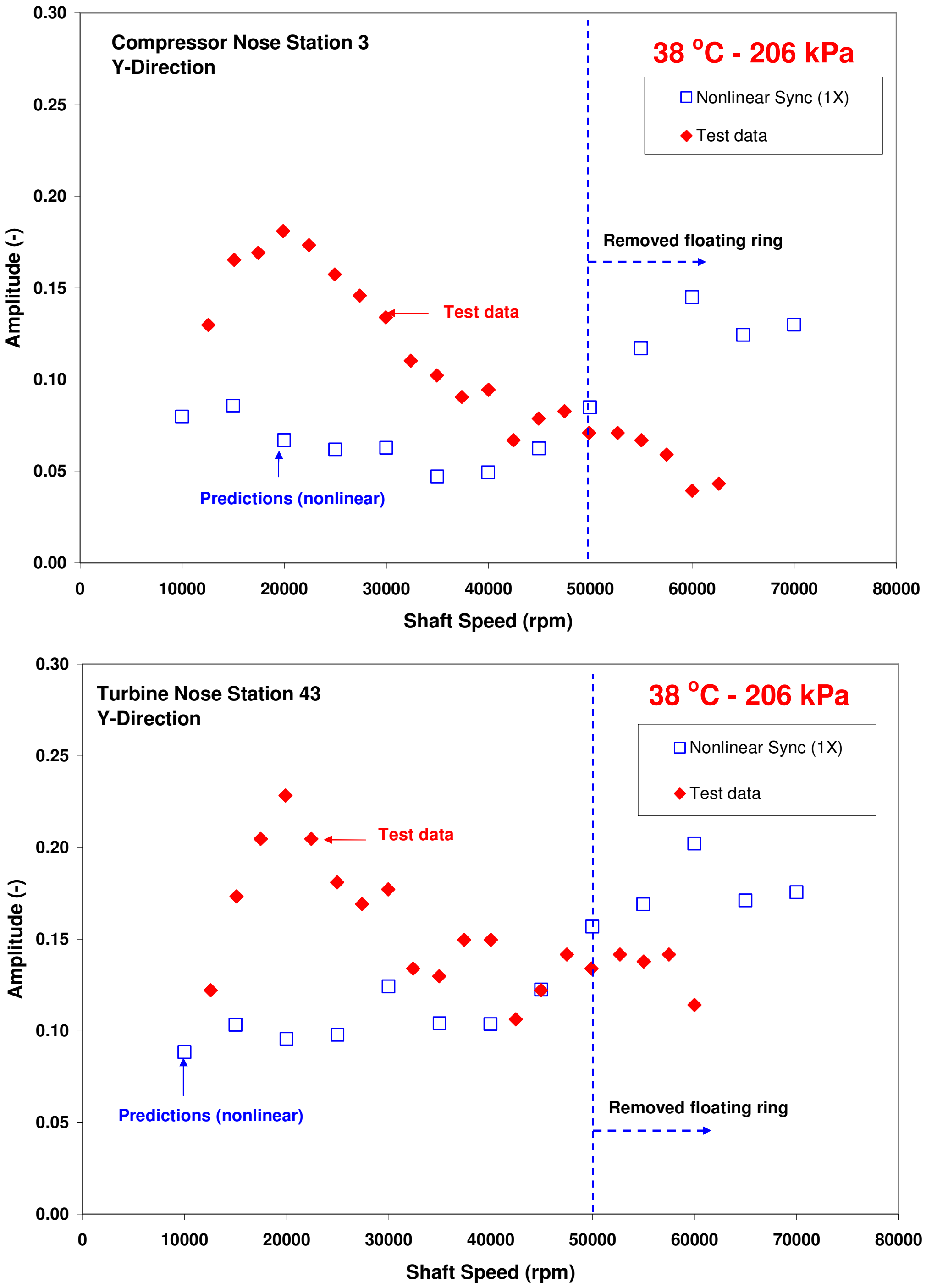

Figure 60 Measured and predicted synchronous response to imbalance at the compressor (top) and turbine (bottom) ends of the rotor. Lubricant feed pressure of 206 kPa and inlet temperature of 38 ^{o}C. <u>Removed floating ring for shaft speeds above 50 krpm</u>

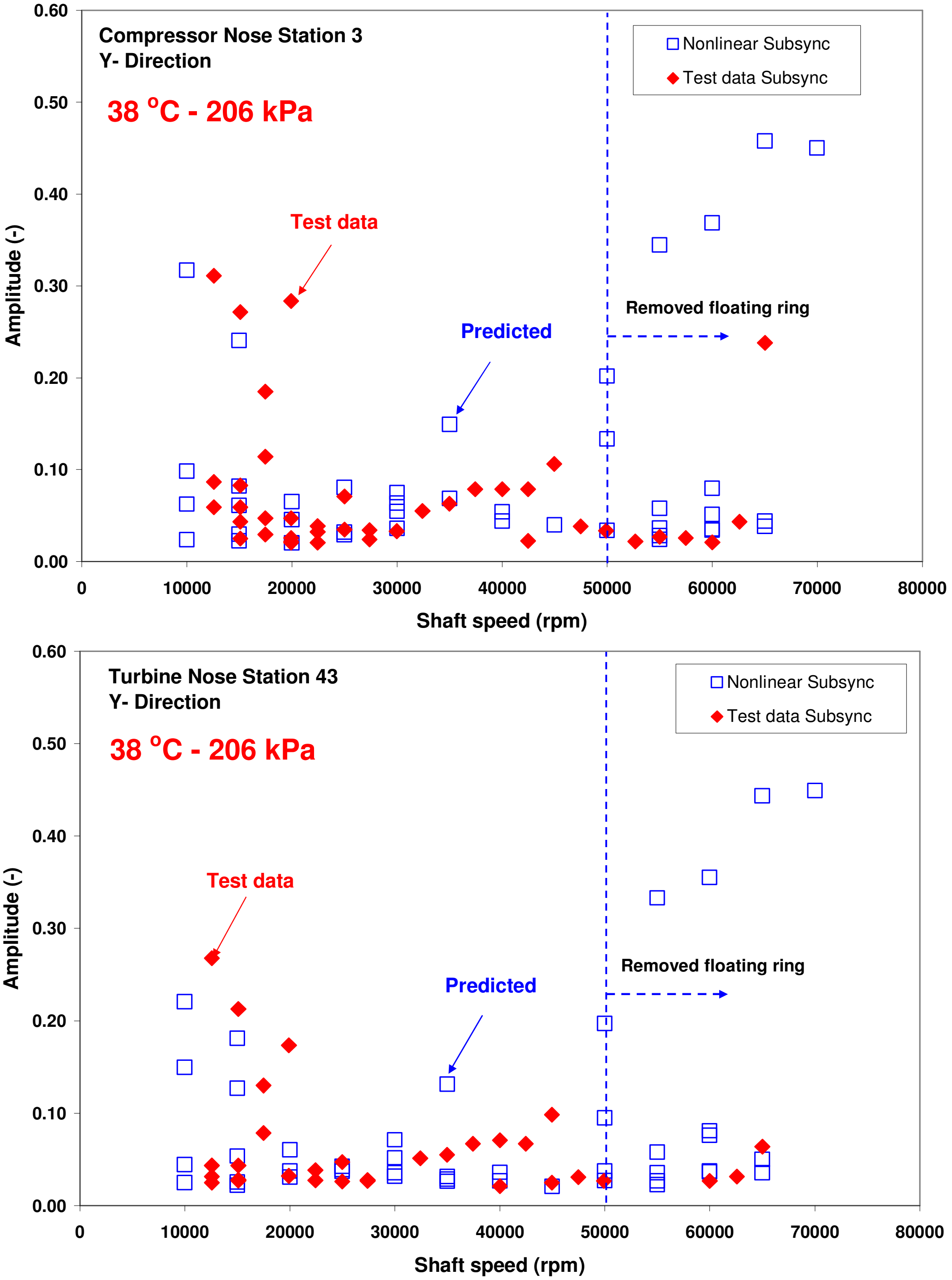

Figure 61 Amplitudes of subsynchronous motions (*Y*-direction) versus shaft speed at the compressor (top) and turbine (bottom) ends of the TC rotor. Lubricant feed pressure of 206 kPa and inlet temperature of 38 °C. Removed floating ring for shaft speeds above 50 krpm

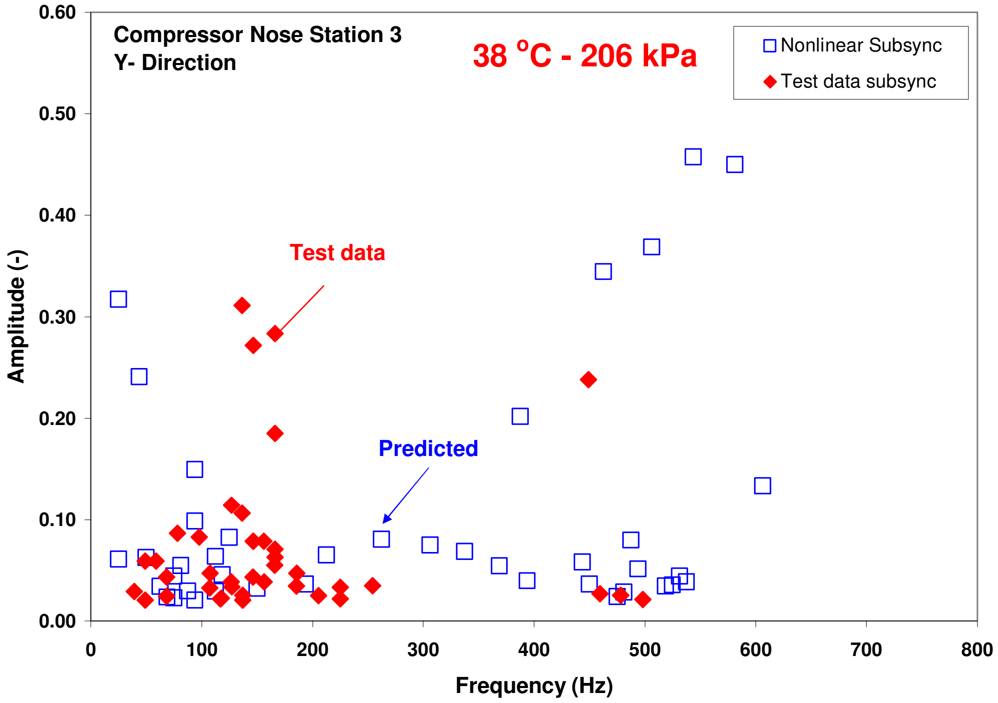

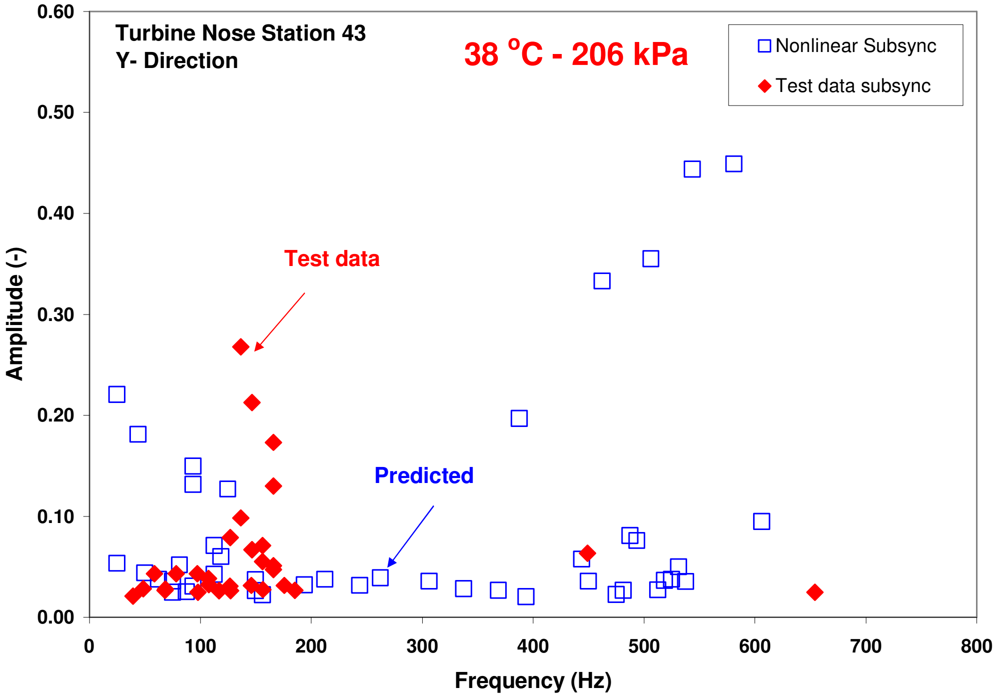

Figure 62 Amplitudes of subsynchronous motions (*Y*-direction) versus frequency at the compressor (top) and turbine (bottom) ends of the TC rotor. Lubricant feed pressure of 206 kPa and inlet temperature of 38 ^{o}C. <u>Removed floating ring for shaft speeds above 50 krpm</u>

APPENDIX C

PREDICTIONS BASED ON TEST DATA FLOATING RING SPEED RATIOS

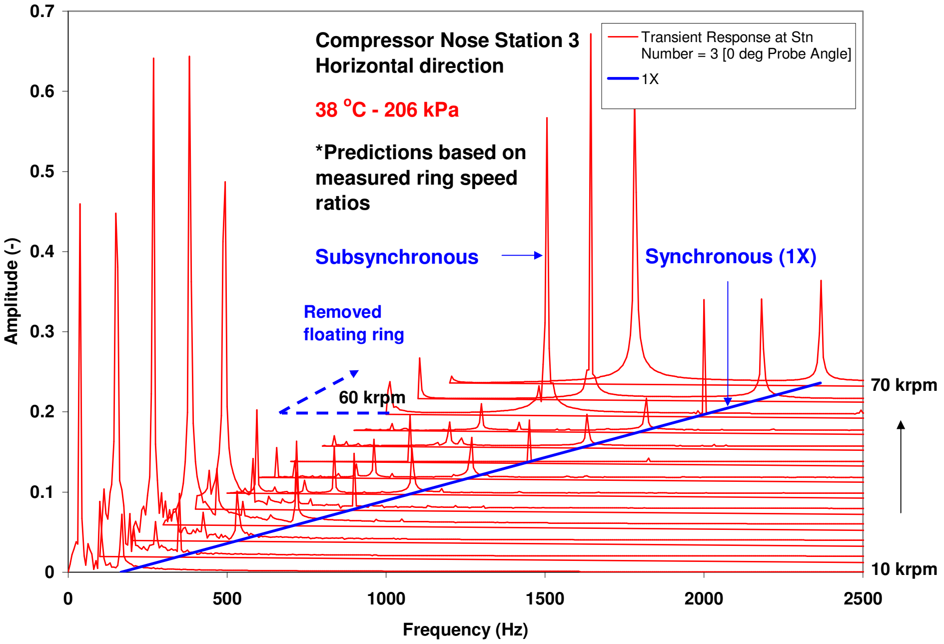

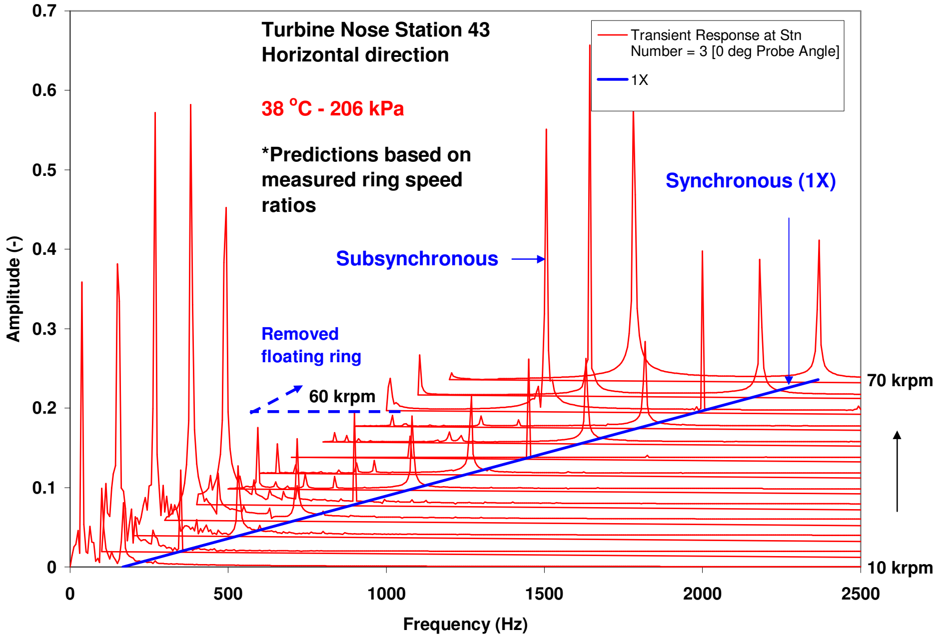

Figure 63 Waterfall of predicted horizontal shaft motions at the compressor (top) and turbine (bottom) ends of the TC rotor. Lubricant feed pressure of 206 kPa and inlet temperature equal to 38 °C. <u>Test floating ring speeds</u>

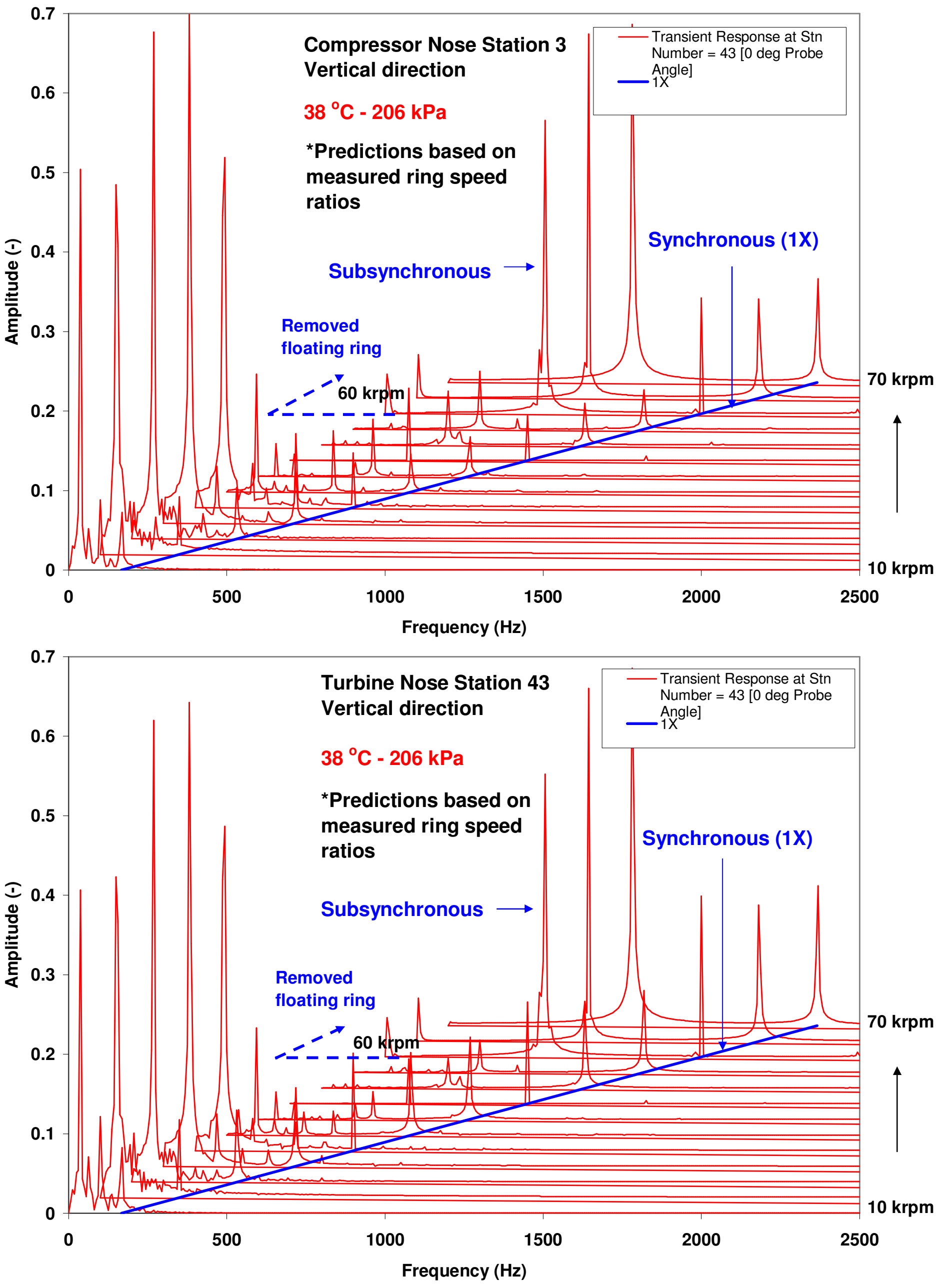

Figure 64 Waterfall of predicted vertical shaft motions at the compressor (top) and turbine (bottom) ends of the TC rotor. Lubricant feed pressure of 206 kPa and inlet temperature equal to 38 °C. <u>Test floating ring speeds</u>

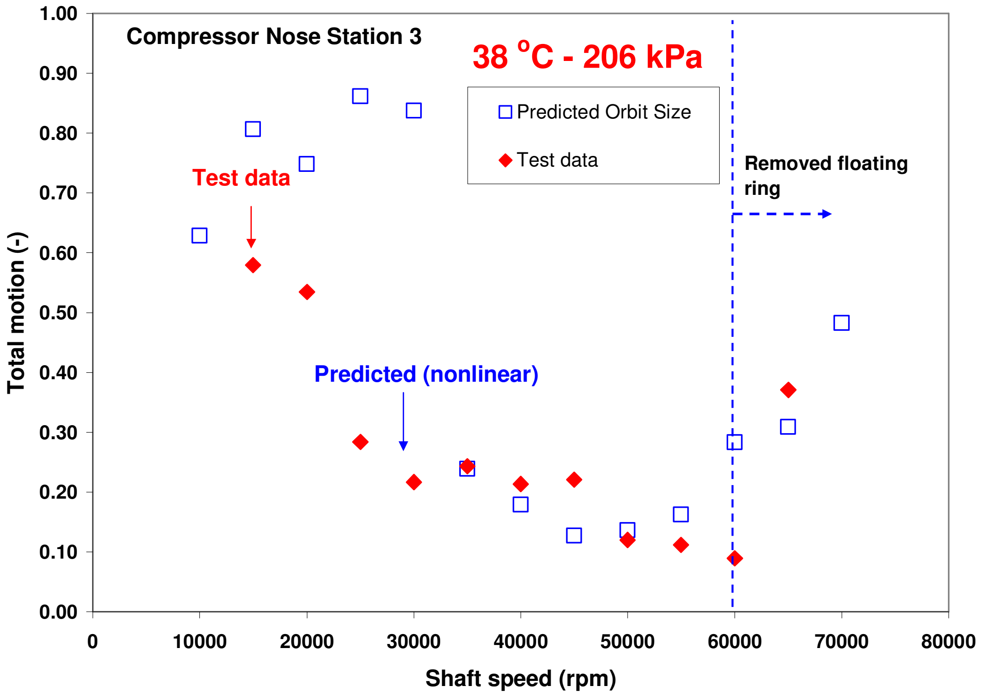

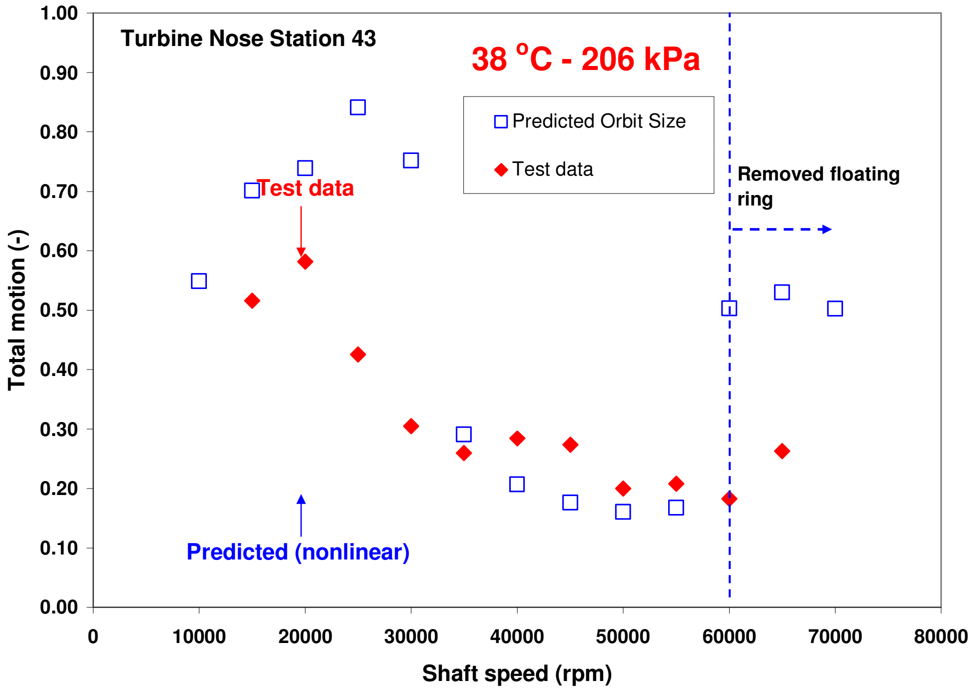

Figure 65 Predicted and measured total shaft motion (pk-pk) at the compressor (top) and turbine (bottom) ends of the TC rotor. Lubricant feed pressure of 206 kPa and inlet temperature of 38 ^{o}C. Test floating ring speeds

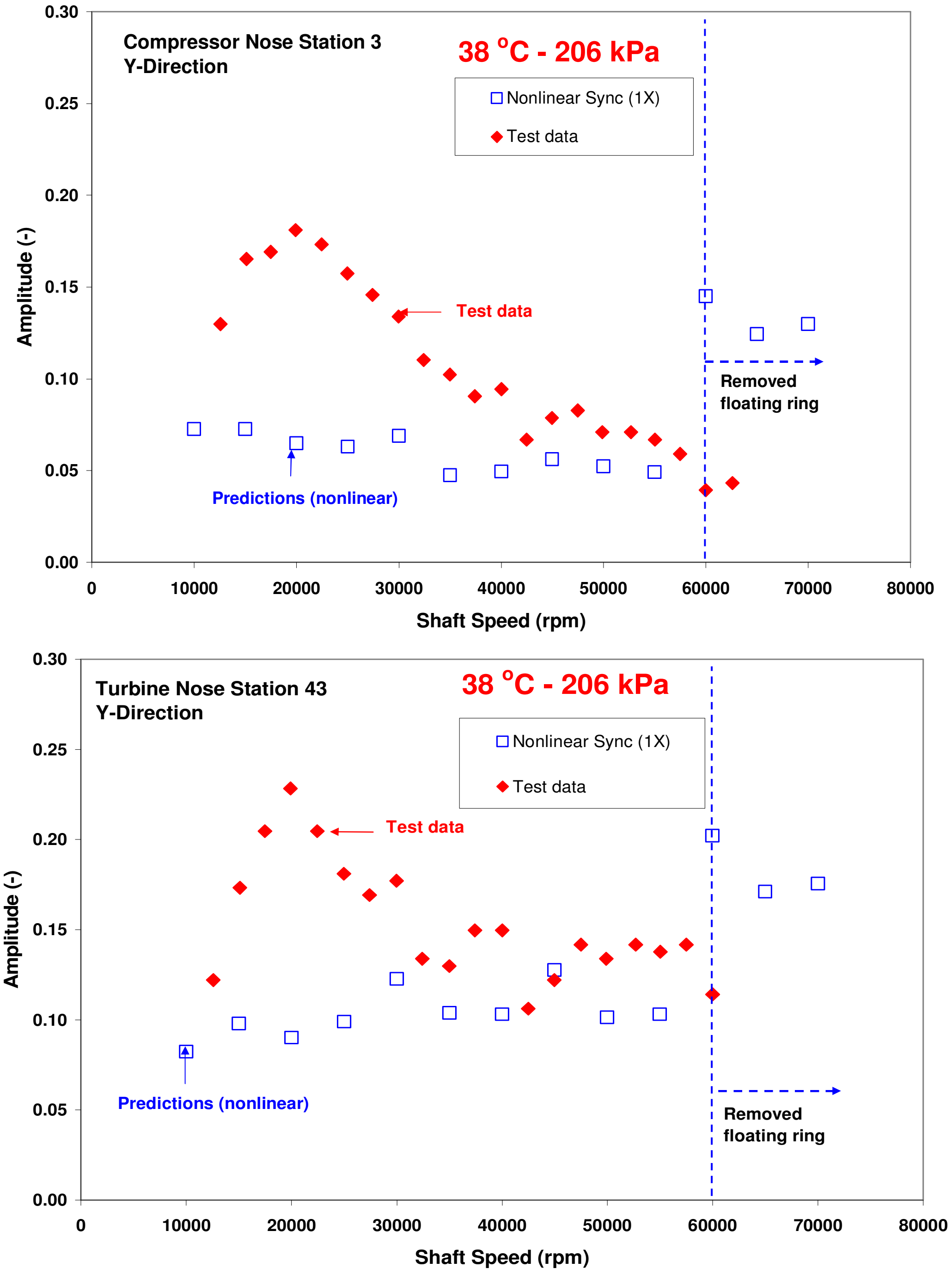

Figure 66 Measured and predicted synchronous response to imbalance at the compressor (top) and turbine (bottom) ends of the rotor. Lubricant feed pressure of 206 kPa and inlet temperature of 38 °C. <u>Test floating ring speeds</u>

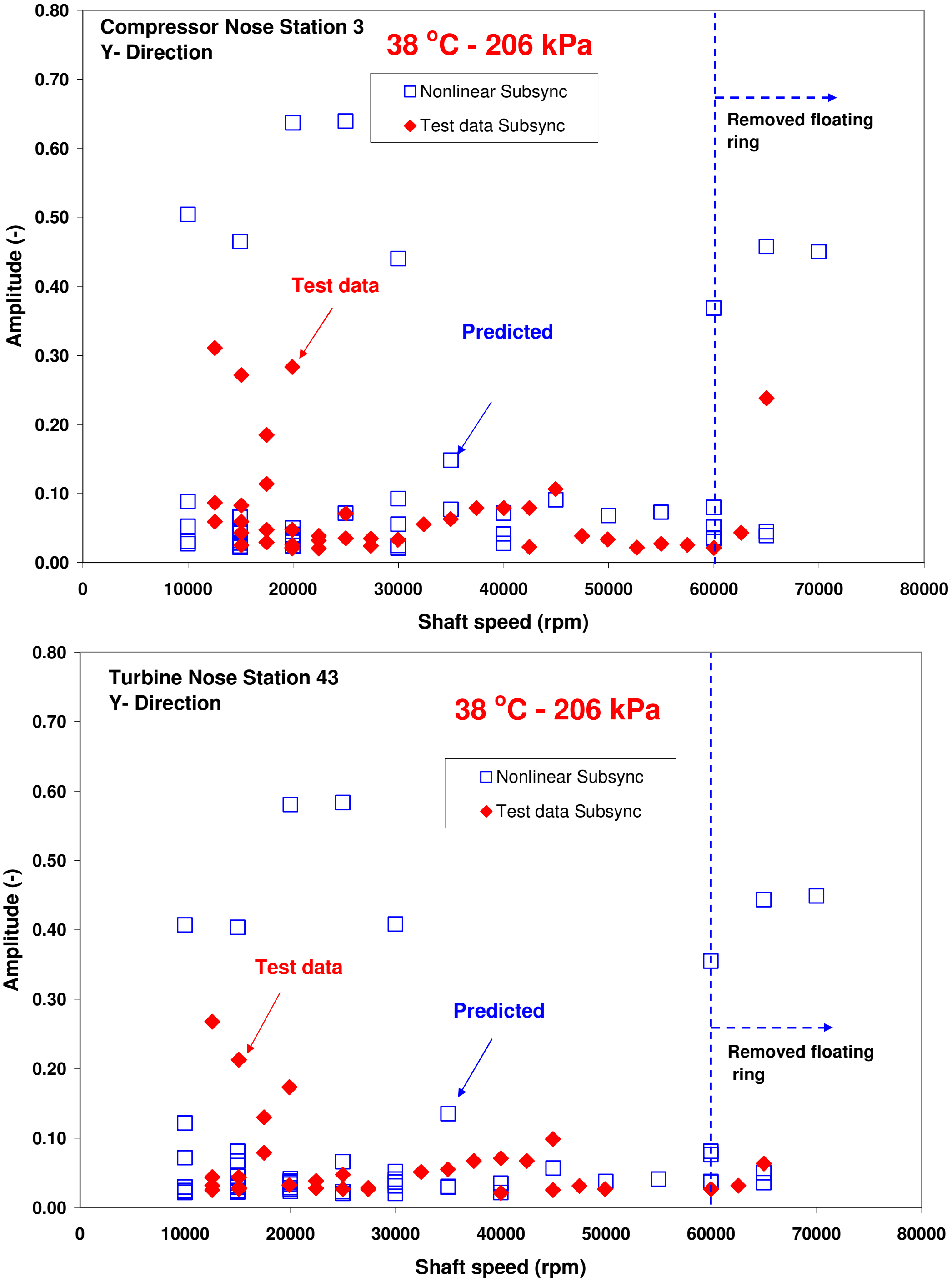

Figure 67 Amplitudes of subsynchronous motions (*Y*-direction) versus shaft speed at the compressor (top) and turbine (bottom) ends of the TC rotor. Lubricant feed pressure of 206 kPa and inlet temperature of 38 °C. Test floating ring speeds

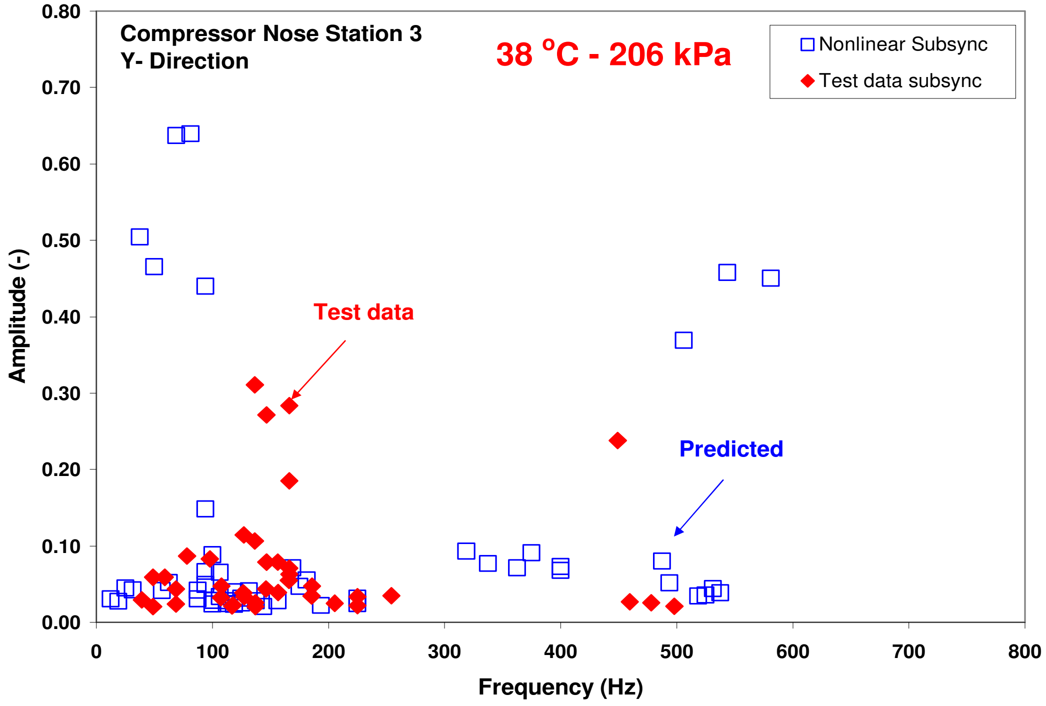

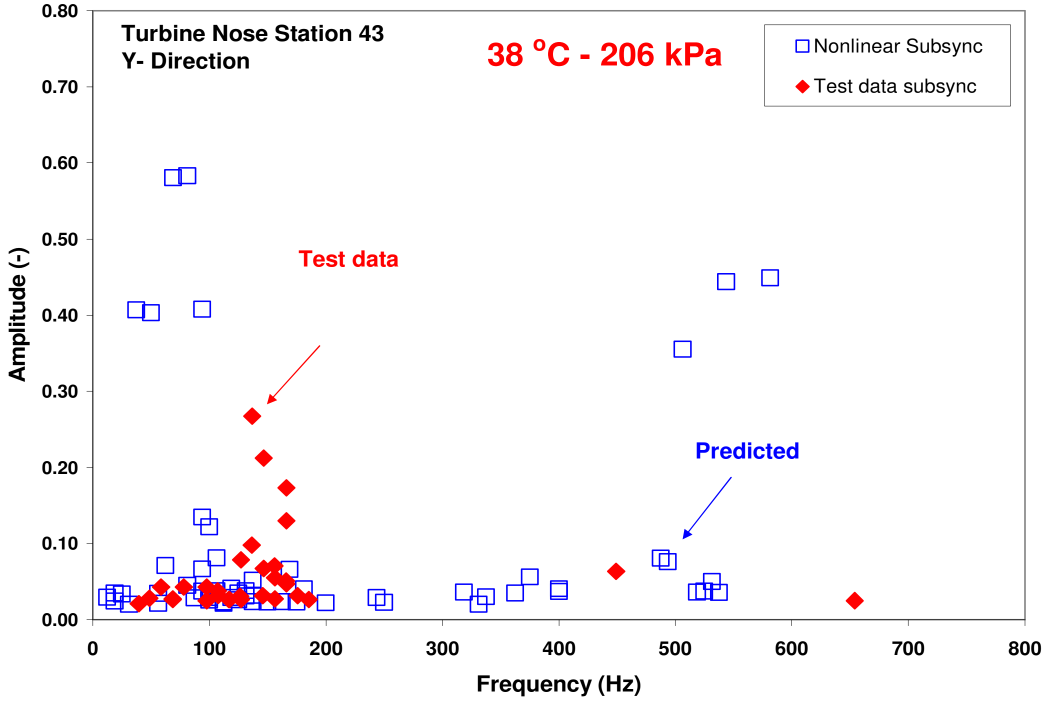

Figure 68 Amplitudes of subsynchronous motions (*Y*-direction) versus frequency at the compressor (top) and turbine (bottom) ends of the TC rotor. Lubricant feed pressure of 206 kPa and inlet temperature of 38 °C. Test floating ring speeds

VITA

Name: Juan Carlos Rivadeneira Pinos

Place of birth: Quito, Ecuador

Education: BS. Mechanical Engineering, Michigan State University, May 2003
MS. Mechanical Engineering, Texas A&M University, May 2006

Email: jkrivadeneira@sbcglobal.net

Address: 10226 Peridot Cove
Houston, Texas 77095